

ACTIVE VIBRATION CONTROL OF A SMART BEAM: A SPATIAL  
APPROACH

A THESIS SUBMITTED TO  
THE GRADUATE SCHOOL OF NATURAL AND APPLIED SCIENCES  
OF  
MIDDLE EAST TECHNICAL UNIVERSITY

BY

ÖMER FARUK KIRCALI

IN PARTIAL FULFILLMENT OF THE REQUIREMENTS  
FOR  
THE DEGREE OF MASTER OF SCIENCE  
IN  
AEROSPACE ENGINEERING

SEPTEMBER 2006

Approval of the Graduate School of Natural and Applied Sciences.

---

Prof. Dr. Canan Özgen  
Director

I certify that this thesis satisfies all the requirements as a thesis for the degree of Master of Science.

---

Prof. Dr. Nafiz Alemdaroğlu  
Head of Department

This is to certify that we have read this thesis and that in our opinion it is fully adequate, in scope and quality, as a thesis for the degree of Master of Science.

---

Dr. Volkan Nalbantoğlu  
Co-Supervisor

---

Prof. Dr. Yavuz Yaman  
Supervisor

Examining Committee Members

Assoc. Prof. Dr. Serkan Özgen	(METU,AEE)	_____
Prof. Dr. Yavuz Yaman	(METU,AEE)	_____
Assist. Prof. Dr. Melin Şahin	(METU,AEE)	_____
Assist. Prof. Dr. Metin U. Salamcı	(Gazi Univ., ME)	_____
Dr. Volkan Nalbantoğlu	(ASELSAN)	_____

**I hereby declare that all information in this document has been obtained and presented in accordance with academic rules and ethical conduct. I also declare that, as required by these rules and conduct, I have fully cited and referenced all material and results that are not original to this work.**

Name, Last name : Ömer Faruk KIRCALI

Signature :

## ABSTRACT

### ACTIVE VIBRATION CONTROL OF A SMART BEAM: A SPATIAL APPROACH

Kırcalı, Ömer Faruk

M. S., Department of Aerospace Engineering

Supervisor: Prof. Dr. Yavuz Yaman

Co-Supervisor: Dr. Volkan Nalbantoğlu

September 2006, 139 Pages

This study presented the design and implementation of a spatial  $H_\infty$  controller to suppress the free and forced vibrations of a cantilevered smart beam. The smart beam consists of a passive aluminum beam with surface bonded PZT (Lead-Zirconate-Titanate) patches. In this study, the PZT patches were used as the actuators and a laser displacement sensor was used as the sensor.

In the first part of the study, the modeling of the smart beam by the assumed-modes method was conducted. The model correction technique

was applied to include the effect of out-of-range modes on the dynamics of the system. Later, spatial system identification work was performed in order to clarify the spatial characteristics of the smart beam.

In the second part of the study, a spatial  $H_\infty$  controller was designed for suppressing the first two flexural vibrations of the smart beam. The efficiency of the controller was verified both by simulations and experimental implementation.

As a final step, the comparison of the spatial and pointwise  $H_\infty$  controllers was employed. A pointwise  $H_\infty$  controller was designed and experimentally implemented. The efficiency of the both controllers was compared by simulations.

**Keywords:** Assumed-Modes Method, Model Correction, Spatial System Identification, Spatial  $H_\infty$  Controller Design.

## ÖZ

### AKILLI BİR KİRİŞİN AKTİF TİTREŞİM KONTROLÜ: UZAMSAL BİR YAKLAŞIM

Kırcalı, Ömer Faruk

Yüksek Lisans, Havacılık ve Uzay Mühendisliği Bölümü

Tez Yöneticisi: Prof. Dr. Yavuz Yaman

Ortak Tez Yöneticisi: Dr. Volkan Nalbantoğlu

Eylül 2006, 139 Sayfa

Bu çalışmada, ankastre akıllı bir kirişin serbest ve zorlanmış titreşimlerinin sönümlendirilmesi için uzamsal  $H_{\infty}$  denetçi tasarımı ve gerçekleştirimi sunulmuştur. Akıllı kiriş pasif alüminyum bir kiriş ve yüzeyine yapıştırılmış PZT (Lead-Zirconate-Titanate) yamalardan oluşmuştur. Çalışmada, PZT yamaları uyarıcı ve bir lazer yardımıyla yerdeğiştirme ölçüm cihazı ile algılayıcı olarak kullanılmıştır.

Çalışmanın ilk bölümünde, akıllı kirişin varsayılan-biçimler metodu ile modellenmesi incelenmiştir. Elde edilen modele yüksek frekanstaki titreşim

biçimlerinin etkisi model iyileştirme tekniği kullanılarak dahil edilmiştir. Daha sonra uzamsal sistem tanımlama yöntemi kullanılarak akıllı kirişin uzamsal karakteristiklerinin daha net bir şekilde elde edilmesi çalışılmıştır.

Çalışmanın ikinci kısmında, akıllı kirişin ilk iki eğilme titreşimlerini söndürmek için uzamsal bir  $H_\infty$  denetçisi tasarlanmıştır. Denetçinin etkinliği benzetim ve deneysel uygulamalar ile doğrulanmıştır.

Son olarak, uzamsal ve noktasal denetçilerin karşılaştırılması çalışılmıştır. Noktasal bir  $H_\infty$  denetçisi tasarlanmış ve deneysel olarak uygulanmıştır. Her iki denetçinin de etkinlikleri benzetimler vasıtasıyla karşılaştırılmıştır.

**Anahtar Kelimeler:** Varsayılan-Biçimler Metodu, Model İyileştirme, Uzamsal Sistem Tanımlama, Uzamsal  $H_\infty$  Denetçi Tasarımı.

*dedicated to*  
*my wife Senem*

*&*

*my all family*

## ACKNOWLEDGMENTS

I would like to express my deepest gratitude to Prof. Dr. Yavuz Yaman, for his great supervision, friendly guidance and encouragement throughout this study.

I also would like to thank to Dr. Volkan Nalbantođlu and Dr. Melin řahin, for their continuous support and great enthusiasm. Their enlightening advices and suggestions have motivated me to introduce this study.

My grateful thanks are for all my friends, the academic and the administrative staff in the department, for their help, understandings and motivations throughout this study. I am also thankful to my colleagues and my managers in Defence Technologies Inc. for their support and understandings.

I am indebted to my all families, the Kırcalıs, Atalayers and Aykaçs, for their endless love, care and encouragement. Their being with me is really priceless.

And finally...I know the words will not be enough, but I wish to express my deepest thanks to my wife Senem. Without your love it was impossible to finish this work. Thank you for always being with me...

## TABLE OF CONTENTS

PLAGIARISM .....	iii
ABSTRACT.....	iv
ÖZ.....	vi
ACKNOWLEDGEMENTS.....	ix
TABLE OF CONTENTS .....	x
LIST OF TABLES .....	xiii
LIST OF FIGURES .....	xiv
NOMENCLATURE.....	xix
CHAPTER	
1. INTRODUCTION .....	1
1.1 Motivation to the Study.....	1
1.2 Historical Background.....	3
1.2.1 Smart Structures .....	3
1.2.2 Structural Modeling and Model Correction.....	4
1.2.3 Active Vibration Control Strategies.....	5
1.3 Aims and Limitations of the Study.....	7
1.4 Outline of the Thesis .....	8
2. THEORY .....	10
2.1 Introduction .....	10
2.2 Modeling Approaches .....	10

2.2.1	Transverse Vibration of a Passive Euler-Bernoulli Beam.....	10
2.2.2	Assumed-Modes Method.....	15
2.3	Assumed-Modes Modeling of the Smart Beam.....	18
2.4	Model Correction Technique.....	25
2.5	Spatial $H_\infty$ Control Technique .....	30
2.6	Conclusion.....	37
3.	IDENTIFICATION OF THE SMART BEAM .....	38
3.1	Introduction .....	38
3.2	Model Correction of the Smart Beam System Model.....	38
3.3	Spatial System Identification of the Smart Beam.....	47
3.4	Conclusion.....	62
4.	ACTIVE CONTROL OF THE SMART BEAM .....	63
4.1	Introduction .....	63
4.2	Spatial $H_\infty$ Control of the Smart Beam .....	64
4.2.1	Controller Design.....	64
4.2.2	Implementation .....	71
4.2.2.1	Free Vibration Control of the Smart Beam .....	72
4.2.2.2	Forced Vibration Control of the Smart Beam.....	73
4.3	Pointwise $H_\infty$ Control of the Smart Beam.....	80
4.3.1	Controller Design.....	80
4.3.2	Implementation .....	86
4.3.2.1	Free Vibration Control of the Smart Beam .....	86
4.3.2.2	Forced Vibration Control of the Smart Beam.....	87
4.4	Comparison of Pointwise and Spatial $H_\infty$ Controllers.....	92
4.5	Conclusion.....	98

5. GENERAL CONCLUSIONS AND RECOMMENDATIONS.....	99
5.1 General Conclusions.....	99
5.2 Recommendations for Future Work.....	101
REFERENCES.....	103
APPENDICES	
A. MODELLING OF THE CANTILEVERED PASSIVE BEAM BY ASSUMED MODES METHOD.....	112
B. MODELING OF THE SMART BEAM BY ASSUMED MODES METHOD.....	120
C. SPATIAL NORMS.....	124
D. SPATIAL $H_\infty$ CONTROL MODEL OF THE SMART BEAM.....	130

## LIST OF TABLES

### TABLES

3.1: Properties of the smart beam.....	39
3.2: First three resonance frequencies of the smart beam.....	41
3.3: The measurement points and their ratios to the length of the smart beam.....	52
3.4: First two flexural resonance frequencies and modal damping ratios of the smart beam.....	57
3.5: Mean and standard deviation of the first two resonance frequencies and modal damping ratios.....	59
4.1: The comparison of attenuation levels under the effect of spatial and pointwise $H_\infty$ controllers in forced vibrations.....	92

## LIST OF FIGURES

### FIGURES

2.1: a) Beam in transverse vibrations. b) Free body diagram of a small element of the beam.....	11
2.2: The smart beam model used in the study .....	18
2.3: Inducing bending moment by applying voltage to PZT patches .....	21
2.4: Spatial $H_\infty$ control problem.....	34
3.1: Zeros of the full order, truncated and corrected models.....	41
3.2: Frequency response of the smart beam at $r = 0.1397L_b$ .....	42
3.3: Frequency response of the smart beam at $r = 0.3219L_b$ .....	42
3.4: Frequency response of the smart beam at $r = 0.7470L_b$ .....	43
3.5: Frequency response of the smart beam at $r = 0.9899L_b$ .....	43
3.6: Frequency responses of the error system models at $r = 0.1397L_b$ .....	45
3.7: Frequency responses of the error system models at $r = 0.3219L_b$ .....	45
3.8: Frequency responses of the error system models at $r = 0.7470L_b$ .....	46
3.9: Frequency responses of the error system models at $r = 0.9899L_b$ .....	46
3.10: The smart beam used in the study.....	48
3.11: Experimental setup for the spatial system identification of the smart beam.....	49
3.12: Applied force .....	50
3.13: Time response of the smart beam measured at $r=0.9899L_b$ .....	50

3.14: The locations of the measurement points.....	51
3.15: Experimental frequency response of the smart beam at $r=0.9899L_b$ .....	53
3.16: Analytical and experimental frequency responses of the smart beam at $r=0.9899L_b$ .....	54
3.17: Experimental and tuned analytical frequency responses at $r=0.9899L_b$ .....	55
3.18: Analytical and experimental frequency responses of the smart beam at $r=0.2611L_b$ .....	58
3.19: Analytical and experimental frequency responses of the smart beam at $r=0.9291L_b$ .....	58
3.20: First mode shape of the smart beam.....	61
3.21: Second mode shape of the smart beam.....	61
4.1: The closed loop system of the smart beam.....	64
4.2: The spatial $H_\infty$ control problem of the smart beam.....	65
4.3: Bode plot of the spatial $H_\infty$ controller .....	69
4.4: Open and closed loop frequency responses of the smart beam under the effect of spatial $H_\infty$ controller.....	69
4.5: Nyquist plot of the nominal system loop gain under the effect of spatial $H_\infty$ controller .....	70
4.6: Bode plots of the open and closed loop systems under the effect of spatial $H_\infty$ controller.....	71
4.7: The closed loop experimental setup.....	72
4.8: Open and closed loop time responses of the smart beam under the effect of spatial $H_\infty$ controller .....	73
4.9: Open and closed loop time responses of the smart beam within excitation of 5-8 Hz under the effect of spatial $H_\infty$ controller.....	75

4.10: Open and closed loop time responses of the smart beam within excitation of 40-44 Hz under the effect of spatial $H_\infty$ controller .	75
4.11: Open and closed loop frequency responses of the smart beam within excitation of 5-8 Hz under the effect of spatial $H_\infty$ controller .....	76
4.12: Open and closed loop frequency responses of the smart beam within excitation of 40-44 Hz under the effect of spatial $H_\infty$ controller .	76
4.13: Bode magnitude plot of the frequency responses of the open and closed loop systems within excitation of 5-8 Hz under the effect of spatial $H_\infty$ controller .....	77
4.14: Bode magnitude plot of the frequency responses of the open and closed loop systems within excitation of 40-44 Hz under the effect of spatial $H_\infty$ controller .....	77
4.15: Open and closed loop time responses of the smart beam under constant excitation at first resonance frequency under the effect of spatial $H_\infty$ controller .....	79
4.16: Open and closed loop time responses of the smart beam under constant excitation at second resonance frequency under the effect of spatial $H_\infty$ controller .....	79
4.17: General framework for control design.....	80
4.18: General feedback diagram for pointwise $H_\infty$ controller design .....	81
4.19: Weights for pointwise $H_\infty$ controller design .....	83
4.20: Bode plot of the pointwise $H_\infty$ controller.....	83
4.21: Open and closed loop frequency responses of the smart beam under the effect of pointwise $H_\infty$ controller .....	84

4.22: Nyquist plot of the nominal system loop gain under the effect of pointwise $H_\infty$ controller .....	84
4.23: Bode plots of the open and closed loop systems under the effect of pointwise $H_\infty$ controller .....	85
4.24: Open and closed loop time responses of the smart beam under the effect of pointwise $H_\infty$ controller.....	86
4.25: Open and closed loop time responses of the smart beam within excitation of 5-8 Hz under the effect of pointwise $H_\infty$ controller .....	88
4.26: Open and closed loop time responses of the smart beam within excitation of 5-8 Hz under the effect of pointwise $H_\infty$ controller .....	88
4.27: Open and closed loop frequency responses of the smart beam within excitation of 5-8 Hz under the effect of pointwise $H_\infty$ controller .....	89
4.28: Open and closed loop frequency responses of the smart beam within excitation of 40-44 Hz under the effect of pointwise $H_\infty$ controller .....	89
4.29: Bode magnitude plot of the frequency responses of the open and closed loop systems within excitation of 5-8 Hz under the effect of pointwise $H_\infty$ controller .....	90
4.30: Bode magnitude plot of the frequency responses of the open and closed loop systems within excitation of 40-44 Hz under the effect of pointwise $H_\infty$ controller .....	90

4.31: Open and closed loop time responses of the smart beam under constant excitation at first resonance frequency under the effect of pointwise $H_\infty$ controller .....	91
4.32: Open and closed loop time responses of the smart beam under constant excitation at second resonance frequency under the effect of pointwise $H_\infty$ controller .....	91
4.33: Simulated $H_\infty$ norm plots of open loop and closed loop systems under the effect of pointwise $H_\infty$ controller .....	94
4.34: Simulated $H_\infty$ norm plots of open loop and closed loop systems under the effect of spatial $H_\infty$ controller .....	94
4.35: Simulated $H_\infty$ norm plots of closed loop systems under the effect of pointwise and spatial $H_\infty$ controllers .....	95
4.36: $\mu$ -analysis for spatial $H_\infty$ controller .....	97
4.37: $\mu$ -analysis for pointwise $H_\infty$ controller .....	97
C.1: A spatially distributed LTI system .....	124

## NOMENCLATURE

$A$	cross sectional area; state matrix; arbitrary constant
$B$	state input matrix
$c$	proportional viscous damping coefficient
$C$	state output matrix
$C_p$	geometric constant due to bending moment
$D$	correction state space matrix
$d_{31}$	piezoelectric charge constant
$E$	Young's modulus of elasticity; error system model
$\bar{E}_{F-T}$	error system between full order and truncated models
$\bar{E}_{F-C}$	error system between full order and corrected models
$f$	distributed force
$F$	viscous or dissipative damping force
$G$	transfer function
$G_C$	corrected transfer function
$G_E$	experimental transfer function
$\bar{G}$	transfer function
$\bar{G}_C$	corrected transfer function
$\bar{G}_2$	transfer function including first 2 modes
$\bar{G}_{50}$	transfer function including first 50 modes
$\mathcal{G}$	generalized plant

$H$	Heaviside step function
$I$	second moment of area
$J$	cost function
$K$	correction term; controller
$k$	constant correction term
$L$	length of the beam ; Lagrangian
$M$	bending moment ; number of modes
$M_{pa}$	bending moment exerted from single PZT patch
$M_p$	total bending moment
$N$	number of admissible functions; number of modes
$p$	external distributed force per unit length
$P, \bar{P}$	constant forcing term
$q$	generalized coordinate
$Q$	external force; spatial weighting function
$r$	spatial coordinate
$R$	entire domain
$S$	shear force
$t$	time (s); thickness
$T$	kinetic energy
$u$	control input; input to the system
$U$	set of all stabilizing controllers
$V$	potential energy
$V_a$	applied voltage
$w$	disturbance
$W$	ideal low-pass weighting function
$W_a$	actuator weight

$W_d$	disturbance weight
$W_{mult}$	multiplicative weight
$W_n$	signal to noise ratio
$W_p$	performance weight
$x, \underline{x}$	state vectors
$y$	measured output; performance output; point coordinate
$\tilde{y}, z, \tilde{z}$	performance outputs

## GREEK SYMBOLS

$\beta$	root of characteristic equation
$\varepsilon$	strain
$\phi$	eigenfunction
$\Delta$	uncertainty block
$\Gamma$	state space matrix
$\delta$	Dirac or Kronecker delta function
$\gamma$	constant term
$\xi$	damping ratio
$\kappa$	control weight
$\lambda$	very small constant term
$\rho$	density
$\sigma$	longitudinal stress
$\Theta$	state space matrix
$\omega$	natural frequency
$\omega_c$	cut-off frequency

$\psi$           admissible function

## **SUPERSCRIPTS**

' ' '          =  $d / dt$

' ' ' '        =  $d^2 / dt^2$

' ' '         =  $d / dr$

' ' ' '        =  $d^2 / dr^2$

$T$           matrix transpose

$opt$         optimum

$*$           complex conjugate transpose

## **SUBSCRIPTS**

$b$           beam

$i$           mode number

$p$           piezoelectric patch

$sb$         smart beam

## **ABBREVIATIONS**

CL         closed loop

dB         decibel

LDS        laser displacement sensor

LHS        left-hand side

LTI	linear time-invariant
OL	open loop
PZT	Lead-Zirconate-Titanate piezoelectric material
$tr\{A\}$	trace of " $A$ "

## MISCELLANEOUS

$\langle\langle \dots \rangle\rangle_2^2$	spatial $H_2$ norm notation
$\ \cdot\ _2^2$	standard $H_2$ norm notation
$\Sigma$	summation
inf	infimum (the greatest lower bound of a set)
sup	supremum (the least upper bound of a set)

# CHAPTER 1

## INTRODUCTION

### 1.1 Motivation to the Study

The vibration phenomenon is an important and a costly issue for lightweight flexible aerospace structures. Those structures may be damaged or become ineffective under the undesired vibrational loads because of possible fatigue and instability. Hence, they require a proper control mechanism to attenuate the vibration levels in order to preserve the structural consistency. The usage of smart materials, as actuators and/or sensors, has become promising research and application area that gives the opportunity to accomplish the reduction of vibration of flexible structures and proves to be an effective active control mechanism.

A smart structure consists of a passive structure and distributed active parts working as sensors and/or actuators. That can sense the external disturbance and respond to it. That kind of structures gives the opportunity to control the vibrations in an active control manner instead of using passive vibration control units such as external vibration absorbers. Recent researches indicate that smart materials such as piezoelectric materials, electrostrictive materials,

magnetostrictive materials, shape memory alloys, electrorheological fluids and magnetorheological fluids can be used as the active parts of a smart structure.

Active vibration control concepts have offered an extensive research area for the last few decades. Designing controllers for decided performance criteria requires a good mathematical modeling of the system. Smart structures can be modeled by using analytical methods or system identification techniques using the experimental data.

The system model of a smart structure generally involves a large number of vibrational modes. However, the performance goals are mostly related to the first few vibrational modes since their effect on structural failure is more prominent. Hence, a reduction of the order of the model is required. On the other hand, ignoring the higher modes can directly affect the system behavior, which in turn requires the researchers to work on model correction techniques in order to compensate the model reduction error and to have more accurate system models.

Today, various controller design techniques are available for attenuating the structural vibration levels. The common behavior of all active vibration control techniques is to suppress the vibration levels for the first few vibrational modes on well-defined specific locations of the structure. Although that kind of pointwise vibration suppression seems to successfully work at those specific locations; the effect of vibration at the rest of the structure may not be effectively controlled. The effects on the entire structure

should be taken into consideration. The spatial active vibration control technique has emerged in order to minimize the vibration over the entire body in a spatially averaged sense.

## **1.2 Historical Background**

### **1.2.1 Smart Structures**

For the last few decades there has been an extensive research about the piezoelectric materials because of the capability of being used both as actuators and sensors. The smart structure is a structure that can sense external disturbance and respond to that in real time to fulfill operational requirements. Smart structures consist of a passive structure, highly distributed active devices called smart materials/elements and processor networks. The smart materials are primarily used as sensors and/or actuators and are either embedded or attached to an existing passive structure [1]. An extensive literature survey about various smart materials and their characteristics can be found in Çalışkan [1]. In this study, PZT (Lead-Zirconate-Titanate) type smart materials are utilized as actuators.

Pierre and Jacques Curie first discovered the direct piezoelectric effect in naturally occurring single crystals such as quartz [2]. They observed that the crystals exposed to mechanical deformation generate voltage on their surfaces. Later, they also discovered that applied electric field caused the material go under mechanical deformation which is known as converse

piezoelectric effect. Having the capability of converting the energies between electrical and mechanical, the piezoelectric materials had the possibility to be used in various application areas. Today, the main and may be the most widespread application area of piezoelectric materials is using them as collocated actuator and sensor pair for active vibration control purposes [3].

### **1.2.2 Structural Modeling and Model Correction**

Active vibration control of a smart structure starts with an accurate mathematical model of the structure. Modeling smart structures may require the modeling of both passive structure and the active parts. Crawley and de Luis [4], by neglecting the mass of active elements, presented an analytical modeling technique to show that the piezoelectric actuators can be used to suppress some modes of vibration of a cantilevered beam. Similar approach was carried out on thin plates by Dimitridis et al [5]. Although neglecting the mass and stiffness properties of the smart materials compared to the passive structure is generally acceptable, the modeling of a smart structure mainly involves the force and moment descriptions generated by the smart materials. Sample modeling studies are proposed by several researchers such as Pota et al. [6], Halim [7]. The governing differential equations of motion of the smart structures can then be solved by analytical methods, such as modal analysis, assumed-modes method, Galerkin's method or finite element method [8].

Since it is not so easy to consider all non-uniformities in structural properties of a smart structure, the analytical modeling techniques such as finite

element model, modal analysis or assumed modes method allow one to obtain system model including only the natural frequencies and mode shapes of the structure except damping [1, 7]. In order to improve the model, Nalbantoğlu [9] and Nalbantoğlu et al. [10] showed that experimental system identification techniques can be applied on flexible structures and they may help one to identify the system more accurately.

Due to having a large number of resonant modes, the high frequency characteristics of a flexible structure generally cause problems in identifying the system model. Since, usually the first few vibrational modes are taken into account in the controller design, the reduction of the model is often required to obtain the finite-dimensional system model [11, 12, 13]. General approach for reducing the order of the model is the direct model reduction. However, removing the higher modes directly from the system model perturbs zeros of the system [14]. Minimizing the effect of model reduction and correcting the system model is possible by adding a feedthrough, or correction, term including some of the removed modes, to the truncated model [14, 15, 16]. Halim [7] proposed an optimal expression for feedthrough term incase of undamped and damped system models.

### **1.2.3 Active Vibration Control Strategies**

Various control techniques have been used as active control strategy like optimal control [17], LQG control [18] and robust control using  $H_\infty$  [9, 19, 20] or  $H_2$  control framework [21].

The robust stabilizing controllers designed based on  $H_\infty$  control technique originated by Zames [22], are widely used in controlling the vibration of smart structures to take into account of the unmodeled dynamics in terms of the uncertainties over the system. The  $H_\infty$  control design technique for robust control phenomena has been developed by many researchers for various application areas including the vibration control [23, 24, 25].

Yaman et al. [19, 26] showed the effect of  $H_\infty$  based controller on suppressing the vibrations of a smart beam due its first two flexural modes. Later they extended their studies to a smart plate [27, 28]. Ülker [20] showed that, besides the  $H_\infty$  control technique,  $\mu$ -synthesis based controllers can also be used to suppress vibrations of smart structures. Lenz et al. [25, 29] studied the active vibration control of a flexible beam using distributed parameter  $H_\infty$  control method in order to obtain finite-dimensional controllers from infinite-dimensional system models. In all those works on flexible structures, the general control strategy focused on analyzing the vibrations at specific locations over the structure and minimizing them. However, that kind of pointwise controller design ignores the effect of vibration at the rest of the body and a successful vibration reduction over entire structure can not always be accounted for.

Moheimani and Fu [30] introduced spatial  $H_2$  norm, which is a measured performance over spatial domain, for spatially distributed systems in order to meet the need of spatial vibration control. Afterwards, Moheimani et al. [13, 31] proposed spatial  $H_\infty$  norm concept and simulation based results of spatial vibration control of a cantilevered beam were presented. Moheimani

et al. [32, 33] carried out the spatial approach on feedforward and feedback controller design, and presented illustrative results. They also showed that spatial  $H_\infty$  controllers could be obtained from standard  $H_\infty$  controller design techniques. Although the simulations demonstrated successful results on minimizing the vibrations over entire beam, implementation of that kind of controllers was not guaranteed on real world systems. Halim [7, 21] studied the implementation of spatial  $H_2$  controllers on active vibration control of a simply-supported beam experimentally and presented successful results. He continued to work on simply-supported beams about implementation of spatial  $H_\infty$  controller and obtained successful experimental results [34]. Further experimental studies were performed on active vibration control of a simply-supported piezoelectric laminate plate by Lee [35]. Lee also attenuated acoustic noise due to structural vibration.

The current study aims to contribute to the spatial control by considering a smart beam under clamped-free boundary conditions. It investigates the effect of spatial control on the suppression vibrations of the cantilevered smart beam.

### **1.3 Aims and Limitations of the Study**

The aim of this thesis is to obtain the corrected system model of a clamped-free smart beam by assumed-modes method and to design and implement a spatial  $H_\infty$  controller to suppress the free and forced vibrations of the smart beam. The smart beam consists of a passive aluminum beam with surface

bonded PZT (Lead-Zirconate-Titanate) patches. In this study, the PZT patches are used as the actuators and a laser displacement sensor is used as the sensor.

The frequency range of interest covers only the first two flexural modes of the smart beam.

The locations of the PZT patches are considered as optimal locations and no formal optimization has been conducted.

The PZT patches are assumed perfectly bonded to the beam.

Nonlinear characteristics of piezoelectric actuators and their hysteresis effects are neglected.

#### **1.4 Outline of the Thesis**

Chapter 1 presents the motivation to the study and gives a literature survey about the smart structures, modeling and control techniques for active vibration control.

Chapter 2 gives the theory which is used and developed in the study.

Chapter 3 gives the verifications of the theoretical model developed and experimental work for spatial system identification of the smart beam.

Chapter 4 describes the design, simulation and implementation of spatial  $H_\infty$  controller and presents experimental results. This chapter also includes a comparison of the spatial and pointwise  $H_\infty$  controllers.

Chapter 5 includes the general conclusions of the study and recommendations for further research.

## CHAPTER 2

### THEORY

#### 2.1 Introduction

This chapter describes the underlying theory of the thesis. The approaches in the modeling are first given and of the assumed-modes method and application of it on the smart beam are then presented. Later, the model correction technique is explained. For the sake of simplicity, the detailed derivations of the formulations and the spatial norm definitions are referred to appendices. The spatial  $H_\infty$  control method and its mathematical background are also described.

#### 2.2 Modeling Approaches

##### 2.2.1 Transverse Vibration of a Passive Euler-Bernoulli Beam

Many flexible structures such as aircraft wings, bridges, and entire buildings experience transverse vibrations. In transverse vibration, the beam deflects perpendicular to its own axis, which in turn results in bending motion.

This chapter studies a uniform Euler-Bernoulli beam with no axial loading.

Consider the transverse deflection of a passive beam of length  $L_b$  shown in Figure 2.1.a. The beam's density, Young's modulus of elasticity and second moment of area are defined as  $\rho_b$ ,  $E_b$ , and  $I_b$  respectively.

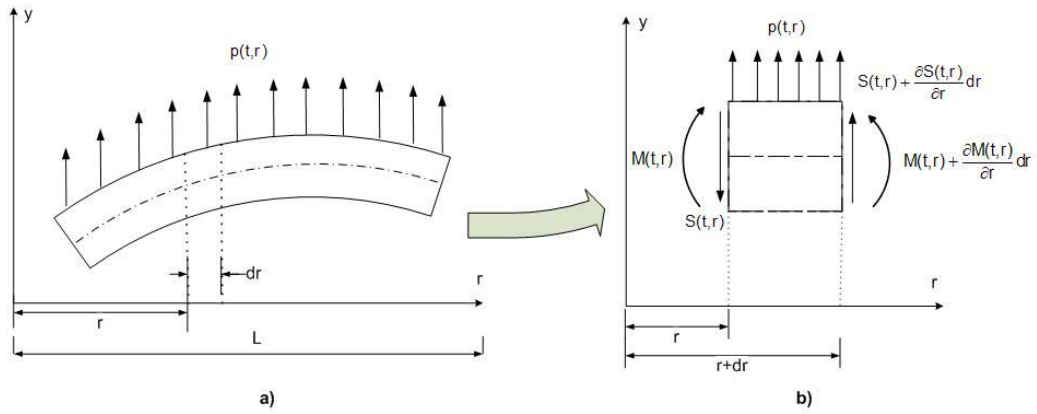


Figure 2.1: a) Beam in transverse vibrations. b) Free body diagram of a small element of the beam.

Consider Figure 2.1.b where  $M(t,r)$ ,  $S(t,r)$ , and  $p(t,r)$  denote the bending moment, shear force, and external distributed force per unit length at  $r$  at time  $t$ , respectively. Applying Newton's second law to the  $y$  direction for small deflections gives:

$$\left\{ S(t,r) + \frac{\partial S(t,r)}{\partial r} dr \right\} - S(t,r) + p(t,r)dr = \rho_b A_b(r)dr \frac{\partial^2 y(t,r)}{\partial t^2} \quad (2.1)$$

which can be found to yield:

$$\frac{\partial S(t,r)}{\partial r} dr + p(t,r)dr = \rho_b A_b(r)dr \frac{\partial^2 y(t,r)}{\partial t^2} \quad (2.2)$$

where  $A_b(r)$  is the cross-sectional area of the beam at point  $r$ .

Since the rotatory inertia effects are neglected, the sum of moments on the element is zero and it consequently leads to:

$$\left\{ M(t,r) + \frac{\partial M(t,r)}{\partial r} dr \right\} - M(t,r) + \left\{ S(t,r) + \frac{\partial S(t,r)}{\partial r} dr \right\} dr + p(t,r)dr \frac{dr}{2} = 0 \quad (2.3)$$

where the point about which the moments are considered is the lower left corner of the beam element of Figure 2.1.b and the counter-clockwise moment is assumed positive.

Equation (2.3) can be simplified to yield:

$$S(t,r) = -\frac{\partial M(t,r)}{\partial r} \quad (2.4)$$

The relation between the bending moment and bending deformation is [8]:

$$M(t,r) = E_b I_b \frac{\partial^2 y(t,r)}{\partial r^2} \quad (2.5)$$

Substituting the bending moment expression given in equation (2.5) into equation (2.4) will give the shear force as:

$$S(t, r) = -\frac{\partial}{\partial r} \left[ E_b I_b \frac{\partial^2 y(t, r)}{\partial r^2} \right] \quad (2.6)$$

Inserting this shear expression into equation (2.2) results in the differential equation of motion for the transverse vibration of the beam:

$$-\frac{\partial^2}{\partial r^2} \left[ E_b I_b \frac{\partial^2 y(t, r)}{\partial r^2} \right] + \rho_b A_b(r) \frac{\partial^2 y(t, r)}{\partial t^2} = p(t, r) \quad (2.7)$$

which is also known as the Euler-Bernoulli beam equation.

This study analyzes the beam in cantilevered configuration. Hence, the boundary conditions of the cantilevered beam are:

At clamped end (i.e.  $r = 0$ ):

$$y(t, r) \Big|_{r=0} = 0 \quad (2.8)$$

$$\frac{\partial y(t, r)}{\partial r} \Big|_{r=0} = 0 \quad (2.9)$$

At free end (i.e.  $r = L_b$ ):

$$E_b I_b \frac{\partial^2 y(t, r)}{\partial r^2} \Big|_{r=L_b} = 0 \quad (2.10)$$

$$\left. \frac{\partial}{\partial r} \left[ E_b I_b \frac{\partial^2 y(t, r)}{\partial r^2} \right] \right|_{r=L_b} = 0 \quad (2.11)$$

Equations (2.7) to (2.11) form a boundary value problem. The solution of the problem for harmonic motion gives the natural modes, or the eigenfunctions, of the cantilevered passive beam as [8]:

$$\phi_i(r) = A_i \left\{ \cosh \beta_i r - \cos \beta_i r - \frac{\cos \beta_i L_b + \cosh \beta_i L_b}{\sin \beta_i L_b + \sinh \beta_i L_b} (\sinh \beta_i r - \sin \beta_i r) \right\} \quad (2.12)$$

where  $A_i$  is an arbitrary constant and  $\beta_i$  are the roots of characteristic equation [8] given in equation (2.13) with subscript  $i$  yielding an infinite number of eigenvalues, i.e.  $i=1, 2, \dots$

$$1 + \cos \beta L_b \cosh \beta L_b = 0 \quad (2.13)$$

Note that, the natural modes of the cantilevered passive beam satisfy the below orthogonality expressions [8]:

$$\int_0^{L_b} \rho_b A_b \phi_i(r) \phi_j(r) dr = 0, \quad i \neq j \quad (2.14)$$

$$\int_0^{L_b} E_b I_b \frac{d^2 \phi_i(r)}{dr^2} \frac{d^2 \phi_j(r)}{dr^2} dr = 0, \quad i \neq j \quad (2.15)$$

### 2.2.2 Assumed-Modes Method

Approximate methods tend to represent the continuous system with an equivalent discrete one. Assumed-modes method is an approximate method that possesses this discretization by means of a series solution. It assumes a solution of the boundary value problem as:

$$y(t, r) = \sum_{i=1}^N \psi_i(r) q_i(t) \quad (2.16)$$

where  $\psi_i(r)$  are admissible functions satisfying the passive beam's geometric boundary conditions, and  $q_i(t)$  are time-dependent generalized coordinates.

Assumed-modes method uses this solution in junction with Lagrange's equation to obtain approximate system model of the structure. Lagrange's equation of motion including nonconservative forces is:

$$\frac{d}{dt} \left( \frac{\partial L}{\partial \dot{q}_i} \right) - \frac{\partial L}{\partial q_i} + \frac{\partial F}{\partial \dot{q}_i} = Q_i \quad (2.17)$$

where  $\dot{\quad}$  represents the derivative with respect to time, i.e.  $d/dt$ , and  $L = T - V$  is the Lagrangian term.  $T(t)$  and  $V(t)$  in Lagrangian term refer to the kinetic and potential energy, respectively. Besides, the nonconservative forces involve the viscous damping force  $F(t)$  and external forces applied on the system  $Q_i(t)$ .

The kinetic and potential energy expressions of a cantilevered passive beam, with uniform structural properties and cross-sectional area, at time  $t$  are [8]:

$$T(t) = \frac{1}{2} \int_0^{L_b} \rho_b A_b \left( \frac{\partial y(t, r)}{\partial t} \right)^2 dr \quad (2.18)$$

$$V(t) = \frac{1}{2} \int_0^{L_b} E_b I_b \left( \frac{\partial^2 y(t, r)}{\partial r^2} \right)^2 dr \quad (2.19)$$

The viscous damping expression of the passive beam is [8]:

$$F(t) = \frac{1}{2} \int_0^{L_b} c \rho_b A_b \left( \frac{\partial y(t, r)}{\partial t} \right)^2 dr \quad (2.20)$$

where  $c$  is the proportional viscous damping coefficient, which is related to viscous damping factor  $\xi$  and natural frequency of the beam  $\omega$  as [8]:

$$c = 2\xi\omega \quad (2.21)$$

The external forces including only a distributed force  $f(t, r)$  have the general expression as [8]:

$$Q_i(t) = \int_0^{L_b} f(t, r) \psi_i(r) dr \quad (2.22)$$

Further, the external force can be decomposed as [8]:

$$Q_i(t) = P_i u(t) \quad (2.23)$$

where  $u(t)$  is the time-dependent excitation force, considered as the input to the system, and  $P_i$  is the constant forcing term.

Following the necessary mathematical manipulations, one will obtain the solution of Lagrange's equation (2.17) in the form of the following ordinary differential equations of motion:

$$\ddot{q}_i(t) + 2\xi_i \omega_i \dot{q}_i(t) + \omega_i^2 q_i(t) = P_i u(t) \quad (2.24)$$

where  $\ddot{\phantom{x}}$  represents the second derivative with respect to time, i.e.  $d^2 / dt^2$ . One should recall that, the subscript  $i$  shows the number of the eigenvalue. That is,  $\xi_i$  and  $\omega_i$  are the modal damping ratios and natural frequencies of the passive beam, respectively.

Taking the Laplace transform of the equation (2.24) will yield the input and output relation of the system dynamics as a transfer function in the frequency domain:

$$G_N(s, r) = \sum_{i=1}^N \frac{P_i \psi_i(r)}{s^2 + 2\xi_i \omega_i s + \omega_i^2} \quad (2.25)$$

where  $G_N(s, r)$  defines the transfer function of the system from system input to the beam deflection including  $N$  number of admissible functions  $\psi_i(r)$ . The detailed derivation of equation (2.25) can be found in Appendix A.

### 2.3 Assumed-Modes Modeling of the Smart Beam

Consider the cantilevered smart beam model used in the study depicted in Figure 2.2.

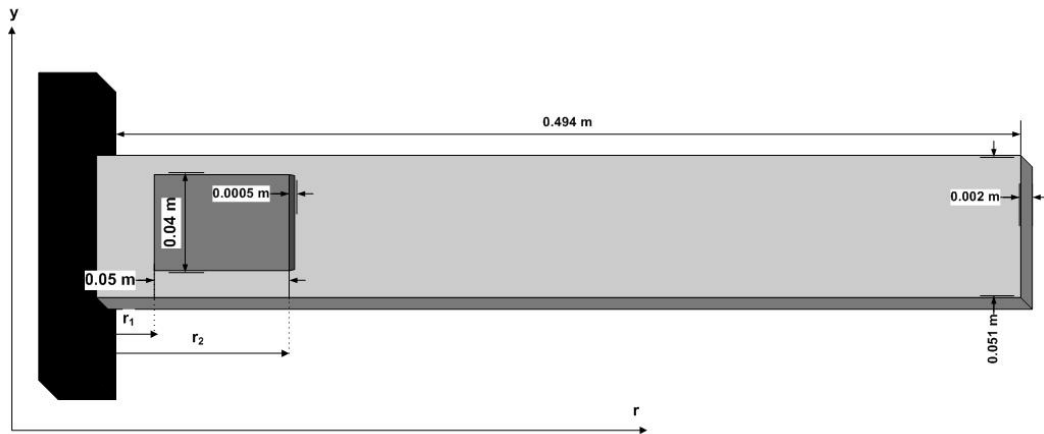


Figure 2.2: The smart beam model used in the study

The smart beam consists of a passive aluminum beam (507mmx51mmx2mm) with eight symmetrically surface bonded SensorTech BM500 type PZT (Lead-Zirconate-Titanate) patches (25mmx20mmx0.5mm), which are used as the actuators. Note that, in this thesis, the group of PZT patches on one side of the beam is considered as if it is a single patch. The beginning and end locations of the PZT patches along the length of the beam away from the fixed end are denoted as  $r_1$  and  $r_2$ , and the patches are assumed to be

optimally placed [1]. The subscripts  $b$  and  $p$  indicate the passive beam and PZT patches, respectively.

The total kinetic energy expression of the smart beam,  $T_{sb}$ , is:

$$T_{sb}(t) = T_b \Big|_0^{r_1} + (T_b + 2T_p) \Big|_{r_1}^{r_2} + T_b \Big|_{r_2}^{L_b} \quad (2.26)$$

where  $T_b$  and  $T_p$  are the kinetic energy expressions of the beam and the PZT patch, respectively. Recall that the kinetic energy expression of the passive beam is given in equation (2.18). Similarly, the kinetic energy expression of the piezoelectric patch bonded to one side of the passive beam can be shown to be:

$$T_p(t) = \frac{1}{2} \int_{r_1}^{r_2} \rho_p A_p \left( \frac{\partial y(t, r)}{\partial t} \right)^2 dr \quad (2.27)$$

Substituting equations (2.18) and (2.27) into equation (2.26), and considering equation (2.16), one can obtain the total kinetic energy expression of the smart beam as:

$$T_{sb}(t) = \frac{1}{2} \sum_{i=1}^N \sum_{j=1}^N \left\{ \int_0^{L_b} \rho_b A_b \psi_i \psi_j dr + 2 \int_{r_1}^{r_2} \rho_p A_p \psi_i \psi_j dr \right\} \dot{q}_i \dot{q}_j \quad (2.28)$$

Similarly, the total potential energy of the smart beam,  $V_{sb}$ , can be shown to yield:

$$V_{sb}(t) = V_b \Big|_0^{r_1} + (V_b + 2V_p) \Big|_{r_1}^{r_2} + V_b \Big|_{r_2}^{L_b} \quad (2.29)$$

where  $V_b$  and  $V_p$  are the potential energy expressions of the beam and the PZT patch, respectively.

The potential energy of the piezoelectric patch bonded to one side of the passive beam is:

$$V_p(t) = \frac{1}{2} \int_{r_1}^{r_2} E_p I_p \left( \frac{\partial^2 y(t, r)}{\partial r^2} \right)^2 dr \quad (2.30)$$

Hence, the total potential energy of the smart beam can be found to yield:

$$V_{sb}(t) = \frac{1}{2} \sum_{i=1}^N \sum_{j=1}^N \left\{ \int_0^{L_b} E_b I_b \psi_i \psi_j'' dr + 2 \int_{r_1}^{r_2} E_p I_p \psi_i \psi_j'' dr \right\} q_i q_j \quad (2.31)$$

where ' ' represents the second derivative with respect to spatial coordinate, i.e.  $d^2 / dr^2$ .

The total viscous damping force of the smart beam,  $F_{sb}$ , is:

$$F_{sb}(t) = F_b \Big|_0^{r_1} + (F_b + 2F_p) \Big|_{r_1}^{r_2} + F_b \Big|_{r_2}^{L_b} \quad (2.32)$$

where  $F_b$  and  $F_p$  are the dissipative damping force expressions of the beam and the PZT patch, respectively.

The viscous damping of the piezoelectric patch bonded to one side of the passive beam is:

$$F_p(t) = \frac{1}{2} \int_{r_1}^{r_2} c \rho_p A_p \left( \frac{\partial y(t,r)}{\partial t} \right)^2 dr \quad (2.33)$$

So, total viscous damping force of the smart beam consequently leads to:

$$F_{sb} = \frac{1}{2} \sum_{i=1}^N \sum_{j=1}^N \left\{ \int_0^{L_b} (2\xi_i \omega_i) \rho_b A_b \psi_i \psi_j dr + 2 \int_{r_1}^{r_2} (2\xi_i \omega_i) \rho_p A_p \psi_i \psi_j dr \right\} \dot{q}_i \dot{q}_j \quad (2.34)$$

If the PZT patches are placed in a collocated manner and the voltage is applied in order to create a bimorph configuration (PZT patches bonded to opposite faces of the beam have opposite polarity), the resulting effect on the beam becomes equivalent to that of a bending moment. This case is shown in Figure 2.3:

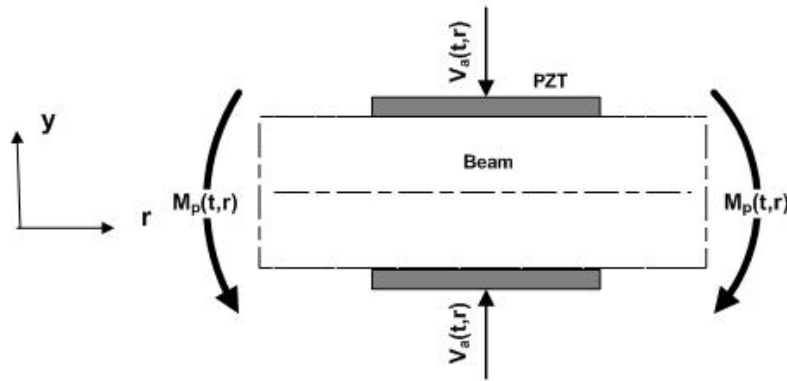


Figure 2.3: Inducing bending moment by applying voltage to PZT patches

Here  $M_p(t, r)$  denotes the bending moment and  $V_a(t, r)$  is the applied voltage. The general expression of the applied voltage is:

$$V_a(t, r) = V_a(t)[H(r - r_1) - H(r - r_2)] \quad (2.35)$$

where  $H(r - r_c)$  denotes the Heaviside step function given as:

$$H(r - r_c) = \begin{cases} 1 & \text{for } r \geq r_c \\ 0 & \text{elsewhere} \end{cases} \quad (2.36)$$

When the voltage in equation (2.35) is applied on a PZT patch, a piezoelectric strain  $\varepsilon_p$  is introduced in the patch [36]:

$$\varepsilon_p(t, r) = \frac{d_{31}}{t_p} V_a(t, r) \quad (2.37)$$

This strain results in a longitudinal stress  $\sigma_p$  as:

$$\sigma_p(t, r) = E_p \varepsilon_p(t, r) \quad (2.38)$$

This stress in turn generates a bending moment about the neutral axis of the system, given by [36]:

$$M_{pa}(t, r) = \int_{t_b/2}^{t_b/2+t_p} \sigma_p(t, r) w_p y dy \quad (2.39)$$

where  $M_{pa}(t, r)$  denotes the bending moment exerted from the PZT patch bonded on one side of the beam. Since both PZT patches having opposite polarity are used as the actuators in this study, the bending moment exerted on the beam becomes:

$$M_p(t, r) = \int_{\frac{t_b}{2}}^{\frac{t_b}{2}+t_p} \sigma_p w_p y dy + \int_{-\frac{t_b}{2}}^{-\left(\frac{t_b}{2}+t_p\right)} \sigma_p w_p y dy \quad (2.40)$$

which consequently leads to:

$$M_p(t, r) = C_p V_a(t, r) \quad (2.41)$$

where  $C_p$  is a geometric constant due to bending moment, and expressed as:

$$C_p = E_p d_{31} w_p (t_p + t_b) \quad (2.42)$$

The loading due to bending moment actuated by PZT patches can be expressed as in (2.22):

$$Q_i = \int_0^{L_b} \frac{\partial^2 M_p}{\partial r^2} \psi_i(r) dr \quad (2.43)$$

In this thesis, the assumed modes (i.e. the admissible functions) of the fixed-free smart beam are taken as the eigenfunctions of the fixed-free passive beam:

$$\phi_i(r) = L_b \left\{ \cosh \beta_i r - \cos \beta_i r - \frac{\cos \beta_i L_b + \cosh \beta_i L_b}{\sin \beta_i L_b + \sinh \beta_i L_b} (\sinh \beta_i r - \sin \beta_i r) \right\} \quad (2.44)$$

where the orthogonality conditions given in equations (2.14) and (2.15) reduce to [37]:

$$\int_0^{L_b} \rho_b A_b \phi_i(r) \phi_j(r) dr = \rho_b A_b L_b^3 \delta_{ij}, \quad i \neq j \quad (2.45)$$

$$\int_0^{L_b} E_b I_b \frac{d^2 \phi_i(r)}{dr^2} \frac{d^2 \phi_j(r)}{dr^2} dr = \rho_b A_b L_b^3 \omega_i^2 \delta_{ij}, \quad i \neq j \quad (2.46)$$

where  $\delta_{ij}$  is the Kronecker's delta function:

$$\delta_{ij} = \begin{cases} 1 & i = j \\ 0 & i \neq j \end{cases} \quad (2.47)$$

Substituting the expressions of equations (2.28), (2.31), (2.34) and (2.43) into equation (2.17) will lead to the following ordinary differential equations of motion:

$$\ddot{q}_i(t) + 2\xi_i \omega_i \dot{q}_i(t) + \omega_i^2 q_i(t) = \frac{C_p V_a(t) [\phi'_i(r_2) - \phi'_i(r_1)]}{\rho_b A_b L_b^3 + 2\rho_p A_p L_p^3} \quad (2.48)$$

where ' ' represents the first derivative with respect to spatial coordinate, i.e.  $d/dr$ .

As a consequence, the transfer function,  $\bar{G}_N(s, r)$ , from the input voltage to the beam deflection in the frequency domain, including  $N$  number of eigenfunctions, is obtained as:

$$\bar{G}_N(s, r) = \sum_{i=1}^N \frac{\bar{P}_i \phi_i(r)}{s^2 + 2\xi_i \omega_i s + \omega_i^2} \quad (2.49)$$

where

$$\bar{P}_i = \frac{C_p [\phi'_i(r_2) - \phi'_i(r_1)]}{\{\rho AL^3\}_{sb}} \quad (2.50)$$

and

$$\{\rho AL^3\}_{sb} = \rho_b A_b L_b^3 + 2\rho_p A_p L_p^3 \quad (2.51)$$

The detailed derivation of equation (2.49) can be found in Appendix B.

## 2.4 Model Correction Technique

Assumed-modes method uses admissible functions in order to model the dynamics of the system, but ignores the nonuniform mass and stiffness distributions. If one uses a large number of admissible functions, or more general if it goes to infinity, the model will be exactly the same as the original one. However, using infinite number of admissible functions is not

convenient to apply for real structures at least for huge amount of computing requirements. Therefore, it is generally believed that the utilization of sufficiently large number of admissible functions will be enough to increase the accuracy of the approximate system model [38].

Including large number of admissible functions leads to not only a more accurate but also a high order approximate system model. Usually such a higher order model yields a high order controller which may not be possible to implement. However, the controller design techniques generally focus on a particular bandwidth which includes only a few vibration modes of the system. In this respect, the reduction of the order of the model is required.

One of the most popular techniques for reducing the order of the system model is the direct model reduction, which simplifies the system model by directly truncating the higher modes of frequency range of interest. However, removing the higher modes may perturb the zeros of the system which will affect the closed-loop performance and stability [14].

One particular approach to compensate the error of the model truncation was presented by Moheimani [39] which considers adding a correction term that minimizes the weighted spatial  $H_2$  norm of the truncation error. The additional correction term had a good improvement on low frequency dynamics of the truncated model. Moheimani [15] and Moheimani et al. [16] developed their corresponding approach to the spatial models which are obtained by different analytical methods. Moheimani [40] presented an application of the model correction technique on a simply-supported

piezoelectric laminate beam experimentally. However, in all those studies, the damping in the system was neglected. Halim [7] improved the model correction approach with damping effect in the system. This section will give a brief explanation of the model correction technique with damping effect based on those previous works [15, 16, 39] and for more detailed explanation the reader is advised to refer to the references [7, 41].

Recall the transfer function of the system from system input to the beam deflection including  $N$  number of modes given in equation (2.25). The spatial system model expression includes  $N$  number of resonant modes assuming that  $N$  is sufficiently large. The controller design however interests in the first few vibration modes of the system, say  $M$  number of lowest modes. So the truncated model including first  $M$  number of modes can be expressed as:

$$G_M(s, r) = \sum_{i=1}^M \frac{P_i \psi_i(r)}{s^2 + 2\xi_i \omega_i s + \omega_i^2} \quad (2.52)$$

where  $M \ll N$ .

This truncation may cause error due to the removed modes which can be expressed as an error system model,  $E(s, r)$ :

$$\begin{aligned} E(s, r) &= G_N(s, r) - G_M(s, r) \\ &= \sum_{i=M+1}^N \frac{P_i \psi_i(r)}{s^2 + 2\xi_i \omega_i s + \omega_i^2} \end{aligned} \quad (2.53)$$

In order to compensate the model truncation error, a correction term should be added to the truncated model [7]:

$$G_C(s, r) = G_M(s, r) + K(r) \quad (2.54)$$

where  $G_C(s, r)$  and  $K(r)$  are the corrected transfer function and correction term, respectively.

The correction term  $K(r)$  involves the effects of the removed modes of the system on the frequency range of interest, and can be expressed as:

$$K(r) = \sum_{i=M+1}^N \psi_i(r) k_i \quad (2.55)$$

where  $k_i$  is a constant term. The reasonable value of  $k_i$  should be determined by keeping the difference between  $G_N(s, r)$  and  $G_C(s, r)$  to be minimum, i.e. corrected system model should approach more to the higher ordered one given in equation (2.25). Moheimani [39] represents this condition by a cost function,  $J$ , which describes that the spatial  $H_2$  norm of the difference between  $G_N(s, r)$  and  $G_C(s, r)$  should be minimized:

$$J = \lll W(s, r) \{G_N(s, r) - G_C(s, r)\} \ggg_2^2 \quad (2.56)$$

The notation  $\lll \dots \ggg_2^2$  represents the spatial  $H_2$  norm of a system where spatial norm definitions are given in Appendix C.  $W(s, r)$  is an ideal low-pass weighting function distributed spatially over the entire domain  $R$  with

its cut-off frequency  $\omega_c$  chosen to lie within the interval  $(\omega_M, \omega_{M+1})$  [39]. That is:

$$|W(j\omega, r)| = \begin{cases} 1 & -\omega_c < \omega < \omega_{c+1}, r \in R \\ 0 & \text{elsewhere} \end{cases} \quad (2.57)$$

and  $\omega_c \in (\omega_M, \omega_{M+1})$

where  $\omega_M$  and  $\omega_{M+1}$  are the natural frequencies associated with mode number  $M$  and  $M + 1$ , respectively.

The reason of selecting  $W(s, r)$  as an ideal low-pass weighting function with its cut-off frequency lower than the first out-of-bandwidth mode, i.e.  $\omega_{M+1}$ , is that the cost function (2.57) will remain finite [41]. Hence, it will be possible to find a finite  $k_i$ .

Halim [7] showed that, by taking the derivative of cost function  $J$  with respect to  $k_i$  and using the orthogonality of eigenfunctions, the general optimal value of the correction term, so called  $k_i^{opt}$ , for the spatial model of resonant systems, including the damping effect, can be shown to be:

$$k_i^{opt} = \frac{1}{4\omega_c\omega_i} \frac{1}{\sqrt{1-\xi_i^2}} \ln \left\{ \frac{\omega_c^2 + 2\omega_c\omega_i\sqrt{1-\xi_i^2} + \omega_i^2}{\omega_c^2 - 2\omega_c\omega_i\sqrt{1-\xi_i^2} + \omega_i^2} \right\} P_i \quad (2.58)$$

An interesting result of equation (2.58) is that, if damping coefficient is selected as zero for each mode, i.e. undamped system, the resultant correction term is equivalent to those given in references [15, 16, 39] for an

undamped system. Therefore, equation (2.58) can be considered as not only the optimal but also the general expression of the correction term.

Substituting equation (2.58) into equation (2.55) gives the general correction term as:

$$K(r) = \sum_{i=M+1}^N \psi_i(r) \left\{ \frac{1}{4\omega_c \omega_i} \frac{1}{\sqrt{1-\xi_i^2}} \ln \left\{ \frac{\omega_c^2 + 2\omega_c \omega_i \sqrt{1-\xi_i^2} + \omega_i^2}{\omega_c^2 - 2\omega_c \omega_i \sqrt{1-\xi_i^2} + \omega_i^2} \right\} P_i \right\} \quad (2.59)$$

So, substituting equation (2.59) into equation (2.54), one will obtain the corrected system model including the effect of out-of-range modes as:

$$G_C(s, r) = \sum_{i=1}^M \frac{P_i \psi_i(r)}{s^2 + 2\xi_i \omega_i s + \omega_i^2} + \sum_{i=M+1}^N \psi_i(r) \left\{ \frac{1}{4\omega_c \omega_i} \frac{1}{\sqrt{1-\xi_i^2}} \ln \left\{ \frac{\omega_c^2 + 2\omega_c \omega_i \sqrt{1-\xi_i^2} + \omega_i^2}{\omega_c^2 - 2\omega_c \omega_i \sqrt{1-\xi_i^2} + \omega_i^2} \right\} P_i \right\} \quad (2.60)$$

## 2.5 Spatial $H_\infty$ Control Technique

Obtaining an accurate system model lets one to understand the system dynamics more clearly and gives him the opportunity to design a consistent controller. Various control design techniques have been developed for active vibration control like  $H_\infty$  or  $H_2$  methods [23, 24].

The effectiveness of  $H_\infty$  controller on suppressing the vibrations of a smart beam due to its first two flexural modes was studied by Yaman et al. [19] and the experimental implementation of the controller was presented [26]. By means of  $H_\infty$  theory, an additive uncertainty weight was included to account the effects of truncated high frequency modes as the model correction. Similar work has been done for suppressing the in-vacuo vibrations due to the first two modes of a smart fin [27, 28] and the effectiveness of the  $H_\infty$  control technique in the modeling of uncertainties was also shown. However,  $H_\infty$  theory does not take into account the multiple sources of uncertainties, which yield unstructured uncertainty and increase controller conservativeness, at different locations of the plant. That problem can be handled by using the  $\mu$ -synthesis control design method [9]. Ülker [20] and Yaman et al. [42] presented the application of  $\mu$ -synthesis active vibration control technique to smart structures.

Whichever the controller design technique, the major objective of vibration control of a flexible structure is to suppress the vibration for the first few vibration modes on well-defined specific locations over the structure. As the flexible structures are distributed parameter systems, the vibration at a specific point is actually related to the vibration over the rest of the structure. As a remedy, minimizing the vibration over entire structure rather than at specific points should be the controller design criteria. The cost functions minimized as design criteria in standard  $H_2$  or  $H_\infty$  control methodologies do not contain any information about the spatial nature of the system. In order to handle this absence, Moheimani and Fu [30], and Moheimani et al. [13, 31] redefined  $H_2$  and  $H_\infty$  norm concepts. They introduced spatial  $H_2$  and

spatial  $H_\infty$  norms of both signals and systems to be used as performance measures.

The concept of spatial control has been developed since last decade. Moheimani et al. [31] studied the application of spatial LQG and  $H_\infty$  control technique for active vibration control of a cantilevered piezoelectric laminate beam. They presented simulation based results in their various works [31, 32, 33]. Experimental implementation of the spatial  $H_2$  and  $H_\infty$  controllers were studied by Halim [7, 21, 34]. These studies proved that the implementation of the spatial controllers on real systems is possible and that kind of controllers show considerable superiority compared to pointwise controllers on suppressing the vibration over entire structure. However, these works examined only simply-supported piezoelectric laminate beam. The contribution to the need of implementing spatial control technique on different systems was done by Lee [35]. Beside vibration suppression, Lee studied attenuation of acoustic noise due to structural vibration on a simply-supported piezoelectric laminate plate.

This section gives a brief explanation of the spatial  $H_\infty$  control technique based on the complete theory presented in reference [41]. For more detailed explanation the reader is advised to refer to the references [7, 41]. Necessary spatial norm definitions can be found in Appendix C.

Consider the state space representation of a spatially distributed linear time-invariant (LTI) system:

$$\begin{aligned}
\dot{x}(t) &= Ax(t) + B_1 w(t) + B_2 u(t) \\
z(t, r) &= C_1(r)x(t) + D_1(r)w(t) + D_2(r)u(t) \\
y(t) &= C_2 x(t) + D_3 w(t) + D_4 u(t)
\end{aligned} \tag{2.61}$$

where  $r$  is the spatial coordinate of the domain  $R$ ,  $x$  is the state vector,  $w$  is the disturbance input,  $u$  is the control input,  $z$  is the performance output and  $y$  is the measured output. The state space representation variables are as follows:  $A$  is the state matrix,  $B_1$  and  $B_2$  are the input matrices from disturbance and control actuators, respectively,  $C_1$  is the output matrix of error signals,  $C_2$  is the output matrix of sensor signals,  $D_1$ ,  $D_2$ ,  $D_3$  and  $D_4$  are the correction terms from disturbance actuator to error signal, control actuator to error signal, disturbance actuator to feedback sensor and control actuator to feedback sensor, respectively.

The spatial  $H_\infty$  control problem is to design a controller which is:

$$\begin{aligned}
\dot{x}_k(t) &= A_k x_k(t) + B_k y(t) \\
u(t) &= C_k x_k(t) + D_k y(t)
\end{aligned} \tag{2.62}$$

such that the closed loop system satisfies:

$$\inf_{K \in U} \sup_{w \in L_2[0, \infty)} J_\infty < \gamma^2 \tag{2.63}$$

where  $U$  is the set of all stabilizing controllers and  $\gamma$  is a constant. The spatial cost function to be minimized as the design criterion of spatial  $H_\infty$  control design technique is:

$$J_\infty = \frac{\int_0^\infty \int_R z(t,r)^T Q(r) z(t,r) dr dt}{\int_0^\infty w(t)^T w(t) dt} \quad (2.64)$$

where  $Q(r)$  is a spatial weighting function that designates the region over which the effect of the disturbance is to be reduced. Since the numerator is the weighted spatial  $H_2$  norm of the performance signal  $z(t,r)$  (see Appendix C),  $J_\infty$  can be considered as the ratio of the spatial energy of the system output to that of the disturbance signal [41]. The control problem is depicted in Figure 2.4:

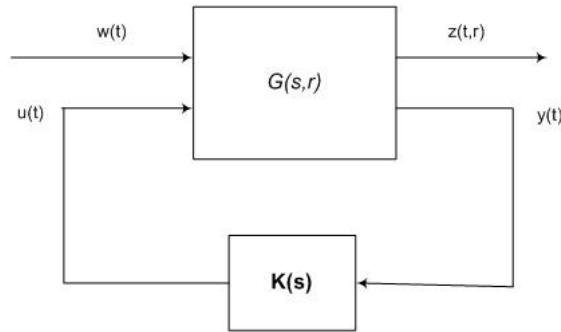


Figure 2.4: Spatial  $H_\infty$  control problem

Spatial  $H_\infty$  control problem can be solved by the equivalent ordinary  $H_\infty$  problem [41] by taking:

$$\int_0^\infty \int_R z(t,r)^T Q(r) z(t,r) dr dt = \int_0^\infty \bar{z}(t)^T \bar{z}(t) dt \quad (2.65)$$

so, the spatial cost function becomes:

$$J_{\infty} = \frac{\int_0^{\infty} \tilde{z}(t)^T \tilde{z}(t) dt}{\int_0^{\infty} w(t)^T w(t) dt} \quad (2.66)$$

The representation in equation (2.66) can be obtained from state space representation of  $z(t, r)$ . Consider  $z(t, r)$  representation:

$$z(t, r) = [C_1(r) \ D_1(r) \ D_2(r)] \begin{bmatrix} x \\ w \\ u \end{bmatrix} \quad (2.67)$$

Substitute equation (2.67) into equation (2.65) and simplify the common integral of  $[0, \infty)$ :

$$\int_R \left\{ [C_1(r) \ D_1(r) \ D_2(r)] \begin{bmatrix} x \\ w \\ u \end{bmatrix} \right\}^T Q(r) \left\{ [C_1(r) \ D_1(r) \ D_2(r)] \begin{bmatrix} x \\ w \\ u \end{bmatrix} \right\} dr = \tilde{z}(t)^T \tilde{z}(t) \quad (2.68)$$

Application of transpose of multiplication of matrices given below to equation (2.68) will yield equation (2.70):

$$(XY)^T = Y^T X^T \quad (2.69)$$

$$\int_R \begin{bmatrix} x \\ w \\ u \end{bmatrix}^T [C_1(r) D_1(r) D_2(r)]^T Q(r) [C_1(r) D_1(r) D_2(r)] \begin{bmatrix} x \\ w \\ u \end{bmatrix} dr = \tilde{z}(t)^T \tilde{z}(t) \quad (2.70)$$

Performing necessary rearrangements, one can reach the following equation:

$$\begin{bmatrix} x^T & w^T & u^T \end{bmatrix} \Gamma^T \Gamma \begin{bmatrix} x \\ w \\ u \end{bmatrix} = \tilde{z}(t)^T \tilde{z}(t) \quad (2.71)$$

where  $\Gamma = [\Pi \quad \Theta_1 \quad \Theta_2]$  is a matrix [7] that satisfies:

$$\Gamma^T \Gamma = \int_R \begin{bmatrix} C_1(r)^T \\ D_1(r)^T \\ D_2(r)^T \end{bmatrix} Q(r) [C_1(r) D_1(r) D_2(r)] dr \quad (2.72)$$

So the spatial  $H_\infty$  control problem is reduced to a standard  $H_\infty$  control problem for the following system:

$$\begin{aligned} \dot{x}(t) &= Ax(t) + B_1 w(t) + B_2 u(t) \\ \tilde{z}(t) &= \Pi x(t) + \Theta_1 w(t) + \Theta_2 u(t) \\ y(t) &= C_2 x(t) + D_3 w(t) + D_4 u(t) \end{aligned} \quad (2.73)$$

However, in order to limit the controller gain and avoid actuator saturation problem, a control weight should be added to the system.

$$\begin{aligned}
\dot{x}(t) &= Ax(t) + B_1 w(t) + B_2 u(t) \\
\tilde{z}(t) &= \begin{bmatrix} \Pi \\ 0 \end{bmatrix} x(t) + \begin{bmatrix} \Theta_1 \\ 0 \end{bmatrix} w(t) + \begin{bmatrix} \Theta_2 \\ \kappa \end{bmatrix} u(t) \\
y(t) &= C_2 x(t) + D_3 w(t) + D_4 u(t)
\end{aligned} \tag{2.74}$$

where  $\kappa$  is the control weight and it designates the level of vibration suppression. Control weight prevents the controller having excessive gain and smaller  $\kappa$  results in higher level of vibration suppression. However, optimal value of  $\kappa$  should be determined in order not to destabilize or neutrally stabilize the system.

## 2.6 Conclusion

This chapter described the underlying theory of the thesis. It was shown that the assumed-modes method can be used to model both the cantilevered passive beam and the smart beam. The model correction technique can be applied to minimize the effect of out-of-range modes. Finally, the spatial  $H_\infty$  control method was described.

## **CHAPTER 3**

### **IDENTIFICATION OF THE SMART BEAM**

#### **3.1 Introduction**

This chapter describes the identification of the smart beam. Recall that analytical system model of the smart beam under transverse vibration was obtained by the help of assumed-modes method and presented in Section 2.3. In this chapter, the modeling was conducted to include the first two flexural modes of the smart beam and so was followed by the model correction technique in order to reduce the effect of neglected high frequency dynamics of the smart beam. Later, in order to obtain the modal damping ratios, resonance frequency values and the uncertainty on them, experimental system identification work was performed.

#### **3.2 Model Correction of the Smart Beam System Model**

Consider the cantilevered smart beam depicted in Figure (2.2) with the structural properties given at Table 3.1.

Table 3.1: Properties of the smart beam

	<b>Aluminum Passive Beam</b>	<b>PZT</b>
Length	$L_b = 0.494m$	$L_p = 0.05m$
Width	$w_b = 0.051m$	$w_p = 0.04m$
Thickness	$t_b = 0.002m$	$t_p = 0.0005m$
Density	$\rho_b = 2710kg / m^3$	$\rho_p = 7650kg / m^3$
Young's Modulus	$E_b = 69GPa$	$E_p = 64.52GPa$
Cross-sectional Area	$A_b = 1.02 \times 10^{-4} m^2$	$A_p = 0.2 \times 10^{-4} m^2$
Second Moment of Area	$I_b = 3.4 \times 10^{-11} m^4$	$I_p = 6.33 \times 10^{-11} m^4$
Piezoelectric charge constant	-	$d_{31} = -175 \times 10^{-12} m/V$

The beginning and end locations of the PZT patches  $r_1 = 0.027m$  and  $r_2 = 0.077m$  away from the fixed end, respectively. Note that, although the actual length of the passive beam is 507mm, the effective length, or span, reduces to 494mm due to the clamping in the fixture.

The system model given in equation (2.49) includes  $N$  number of modes of the smart beam, where as  $N$  gets larger, the model becomes more accurate. In this study, first 50 flexural resonant modes are included into the model (i.e.  $N = 50$ ) and the resultant model is called *the full order model*:

$$\bar{G}_{50}(s, r) = \sum_{i=1}^{50} \frac{\bar{P}_i \phi_i(r)}{s^2 + 2\xi_i \omega_i s + \omega_i^2} \quad (3.1)$$

However, the control design criterion of this thesis is to suppress only the first two flexural modes of the smart beam. Hence, the full order model is directly truncated to a lower order model, including only the first two flexural modes, and the resultant model is called *the truncated model*:

$$\bar{G}_2(s, r) = \sum_{i=1}^2 \frac{\bar{P}_i \phi_i(r)}{s^2 + 2\xi_i \omega_i s + \omega_i^2} \quad (3.2)$$

As previously explained, the direct model truncation may cause the zeros of the system to perturb, which consequently affect the closed-loop performance and stability of the system considered [14]. For this reason, the general correction term, given in equation (2.58), is added to the truncated model and the resultant model is called *the corrected model*:

$$\begin{aligned} \bar{G}_c(s, r) = & \sum_{i=1}^2 \frac{\bar{P}_i \phi_i(r)}{s^2 + 2\xi_i \omega_i s + \omega_i^2} \\ & + \sum_{i=3}^{50} \phi_i(r) \left\{ \frac{1}{4\omega_c \omega_i} \frac{1}{\sqrt{1-\xi_i^2}} \ln \left[ \frac{\omega_c^2 + 2\omega_c \omega_i \sqrt{1-\xi_i^2} + \omega_i^2}{\omega_c^2 - 2\omega_c \omega_i \sqrt{1-\xi_i^2} + \omega_i^2} \right] \right\} \bar{P}_i \end{aligned} \quad (3.3)$$

where the cut-off frequency, based on the selection criteria given in equation (2.57), is taken as:

$$\omega_c = (\omega_2 + \omega_3) / 2 \quad (3.4)$$

The assumed-modes method gives the first three resonance frequencies of the smart beam as shown in Table 3.2.

Table 3.2: First three resonance frequencies of the smart beam

Resonance Frequencies	Value (Hz)
$\omega_1$	6.680
$\omega_2$	41.865
$\omega_3$	117.214

Hence, the cut-off frequency becomes 79.539 Hz. Figure 3.1 shows the effect of model correction on the locations of the zeros of the system. By applying the model correction to the truncated model, the zeros of the truncated system approach to the zeros of the full order model. The performance of model correction for various system models obtained from different measurement points along the beam is shown in Figure 3.2, Figure 3.3, Figure 3.4 and Figure 3.5.

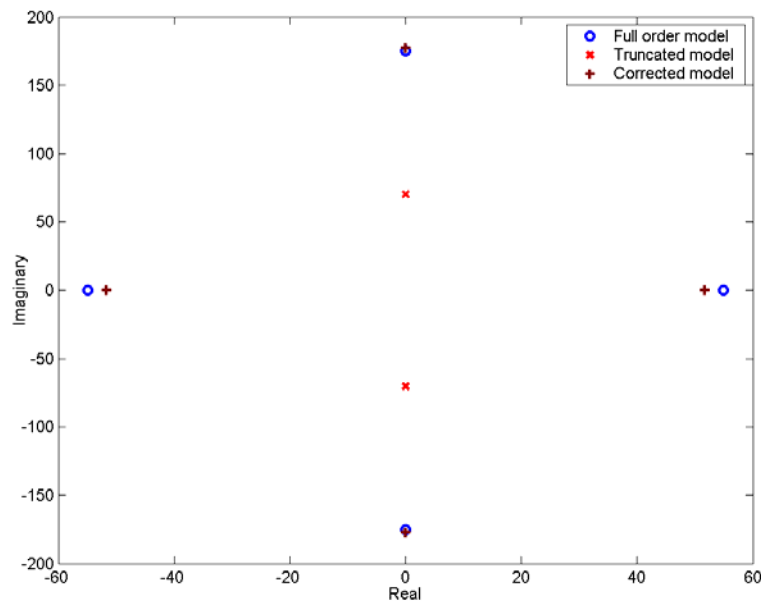


Figure 3.1: Zeros of the full order, truncated and corrected models.

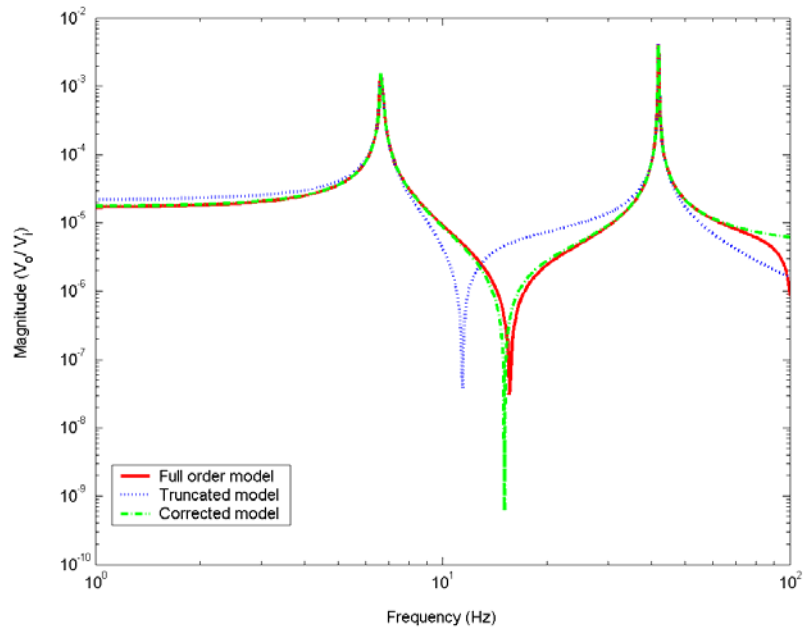


Figure 3.2: Frequency response of the smart beam at  $r = 0.1397L_b$

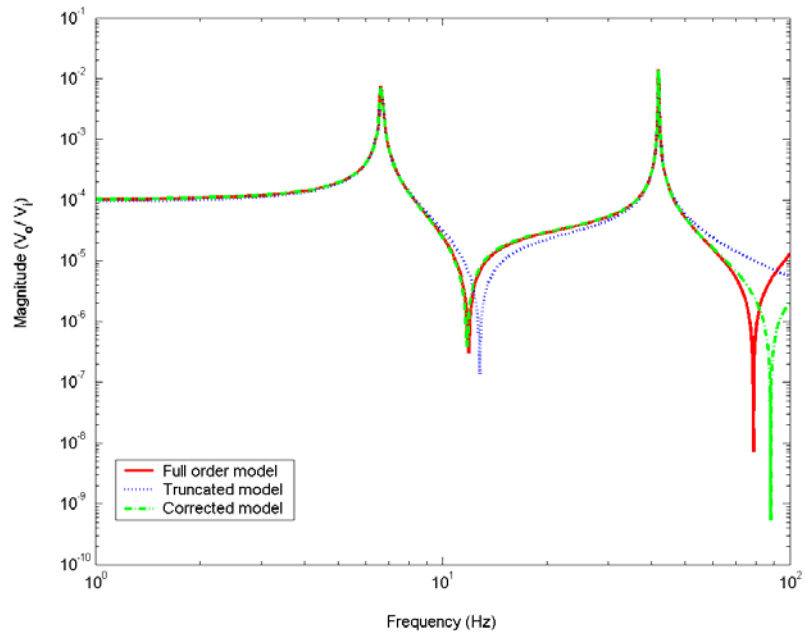


Figure 3.3: Frequency response of the smart beam at  $r = 0.3219L_b$

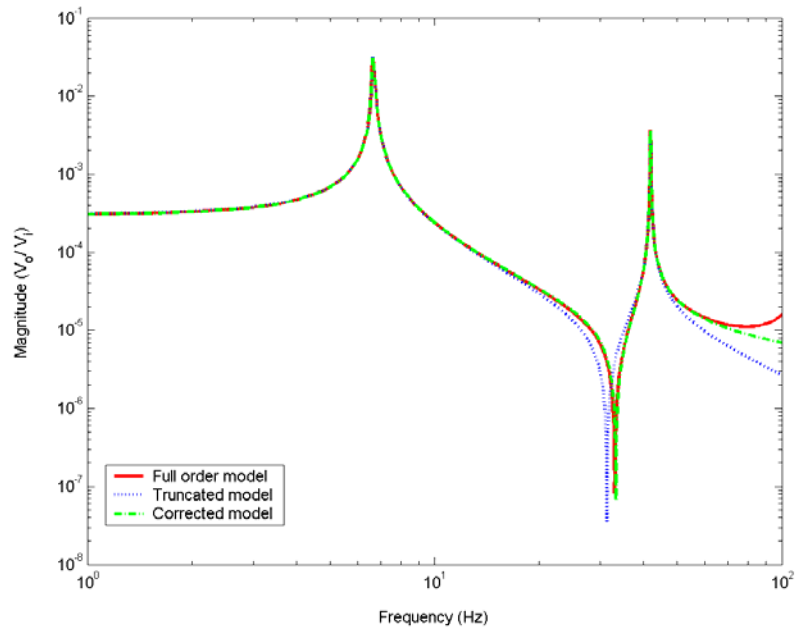


Figure 3.4: Frequency response of the smart beam at  $r = 0.7470L_b$

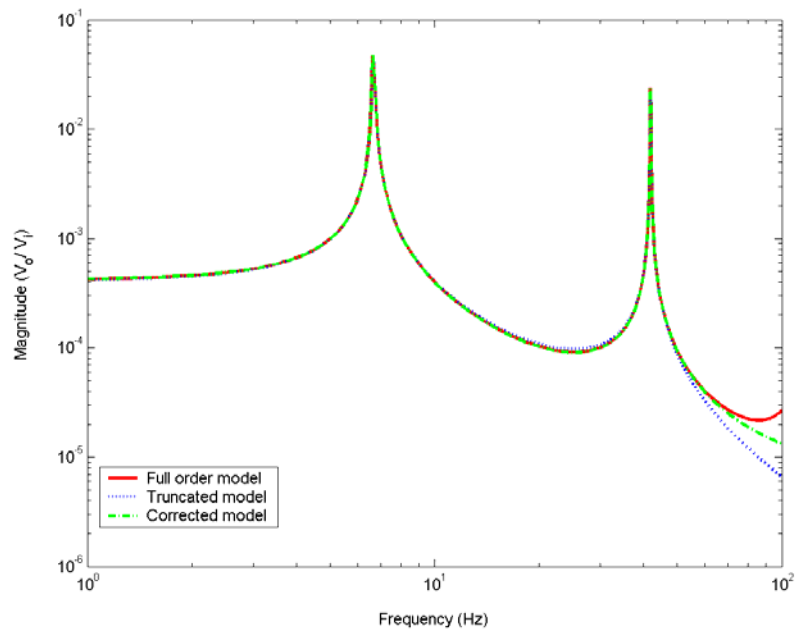


Figure 3.5: Frequency response of the smart beam at  $r = 0.9899L_b$

The error between full order model-truncated model, and the error between full order model-corrected model, so called the error system models  $\bar{E}_{F-T}$  and  $\bar{E}_{F-C}$ , allow one to see the effect of model correction more comprehensively.

$$\bar{E}_{F-T} = \bar{G}_N(s, r) - \bar{G}_M(s, r) \quad (3.5)$$

$$\bar{E}_{F-C} = \bar{G}_N(s, r) - \bar{G}_C(s, r) \quad (3.6)$$

The frequency responses of the error system models are shown in Figure 3.6, Figure 3.7, Figure 3.8 and Figure 3.9.

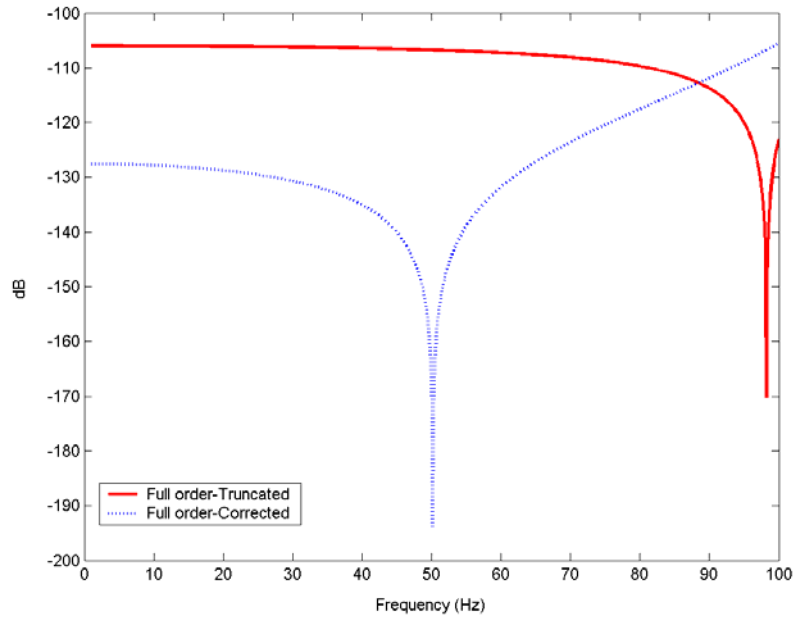


Figure 3.6: Frequency responses of the error system models at  $r = 0.1397L_b$

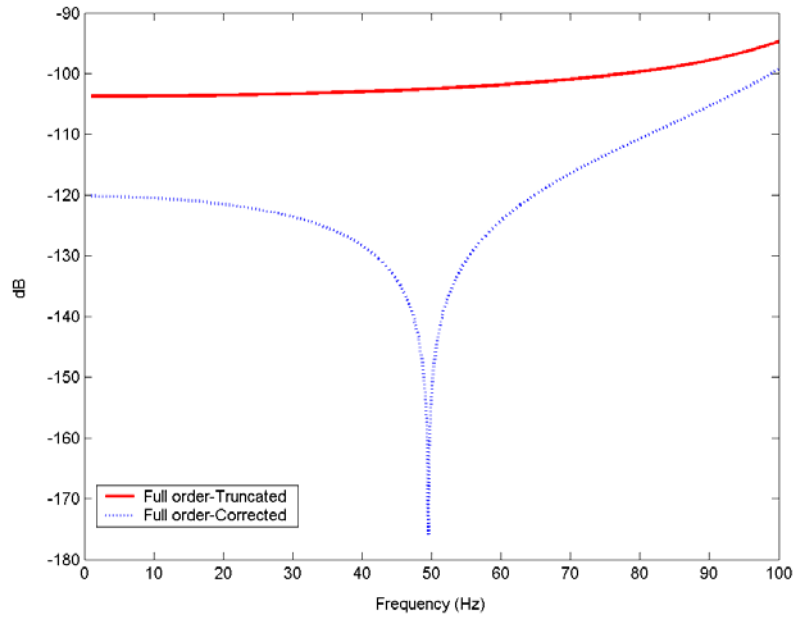


Figure 3.7: Frequency responses of the error system models at  $r = 0.3219L_b$

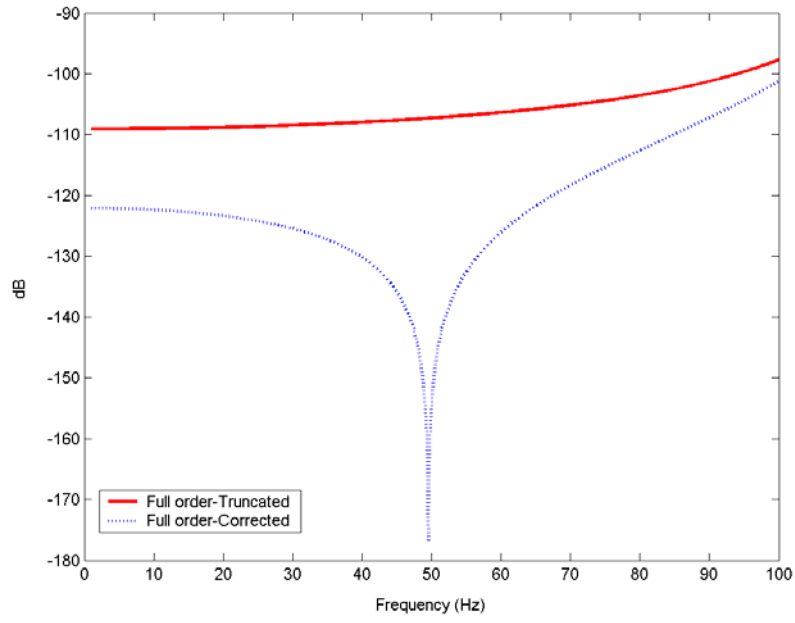


Figure 3.8: Frequency responses of the error system models at  $r = 0.7470L_b$

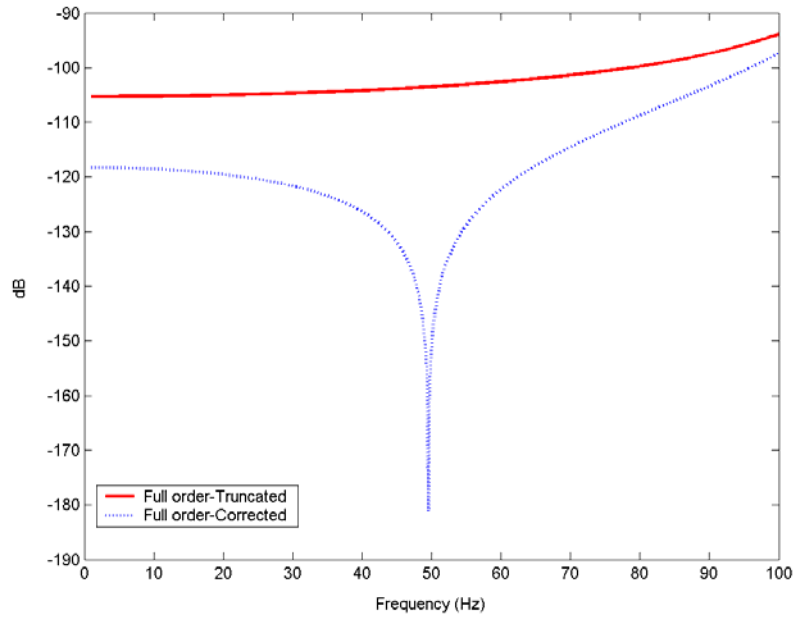


Figure 3.9: Frequency responses of the error system models at  $r = 0.9899L_b$

One can easily notice from the above figures that, the error between the full order and corrected models is less than the error between the full order and truncated ones in a wide range of the interested frequency bandwidth. That is, the model correction minimizes error considerably and makes the truncated model approach the full order one. The error between the full order and corrected models is smaller at low frequencies and around 50 Hz it reaches a minimum value. As a result, model correction reduces the overall error due to model truncation, as desired.

### **3.3 Spatial System Identification of the Smart Beam**

Theoretical assumed-modes modeling does not provide any information about the damping of the system. Experimental system identification, on the other hand, when used in collaboration with the analytical model, helps one to obtain more accurate spatial characteristics of the structure.

System identification technique consists of two main branches called as nonparametric identification and parametric identification [43]. In nonparametric identification, the system is excited, for example, by a sine-wave and one can obtain the transfer function of the system [9]. In parametric identification, basically, curve fitting is conducted to give a proper system model that best matches with the frequency response of that transfer function. Additionally, comparing the experimental model with the analytical one leads to determine the modal damping terms and the uncertainty on resonance frequencies [44].

The smart beam of this study, shown in Figure 3.10, consists of piezoelectric patches which are used as the actuators. Keyence LB-1201(W) LB-300 laser displacement sensor (LDS) is used as the sensor.

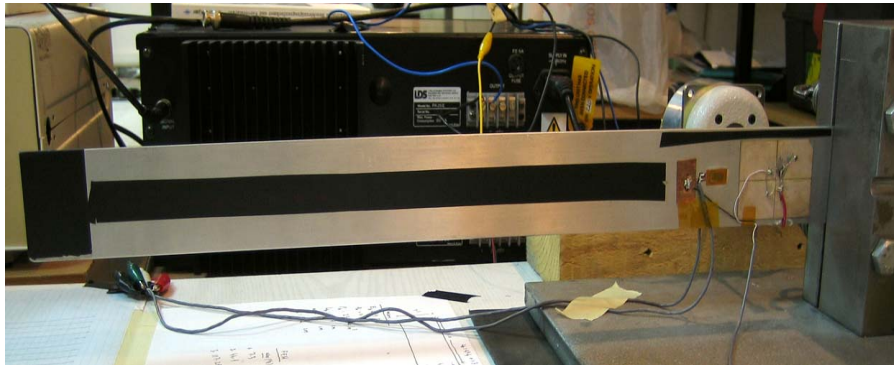


Figure 3.10: The smart beam used in the study

In this study, the experimental transfer functions based on displacement measurements were obtained by nonparametric identification. The smart beam was excited by piezoelectric patches with sinusoidal chirp signal of amplitude 5V within bandwidth of 0.1-60 Hz, which covers the first two flexural modes of the smart beam. The response of the smart beam was acquired via laser displacement sensor from specified measurement points. Since the patches are relatively thin compared to the passive aluminum beam, the system was considered as 1-D single input multi output system, where all the vibration modes are flexural modes. One should note that, system identification technique uses the input and output data in order to form the transfer function. Hence, performing a healthy identification and obtaining an accurate system model is strictly dependent on the amount of data collected. That is to say the excitation period should be long enough to sweep the interested frequency range which yields a higher sampling rate. In

this study, the smart beam was excited for 240 seconds, where longer time was prevented due to hardware constraints. The open loop experimental setup is shown in Figure 3.11.

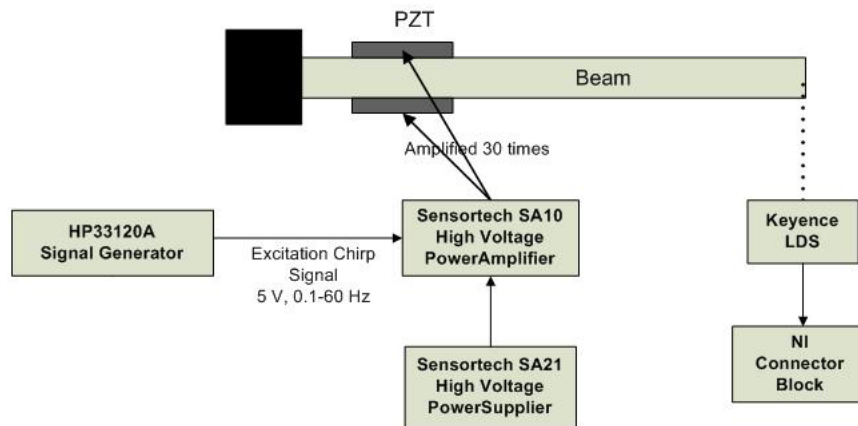


Figure 3.11: Experimental setup for the spatial system identification of the smart beam

The applied force and the time response of the smart beam measured from the point  $r=0.9899 L_b$  are given in Figure 3.12 and Figure 3.13, respectively:

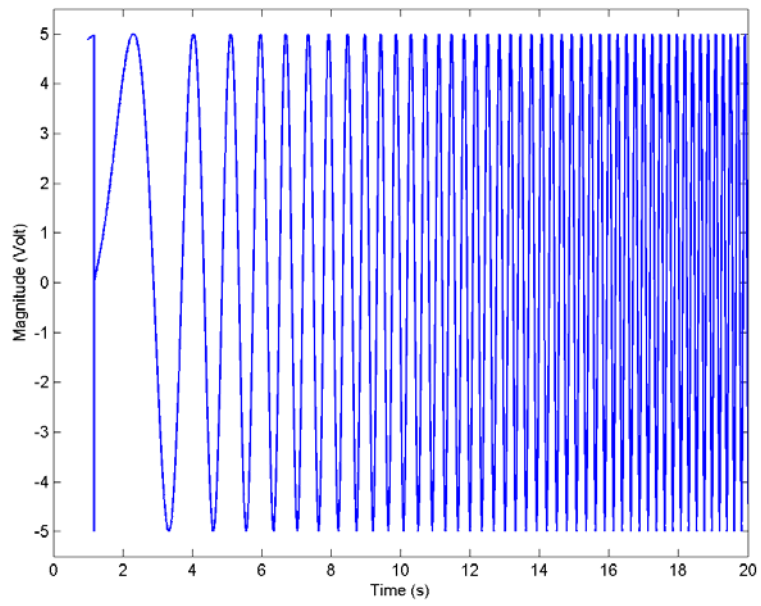


Figure 3.12: Applied force

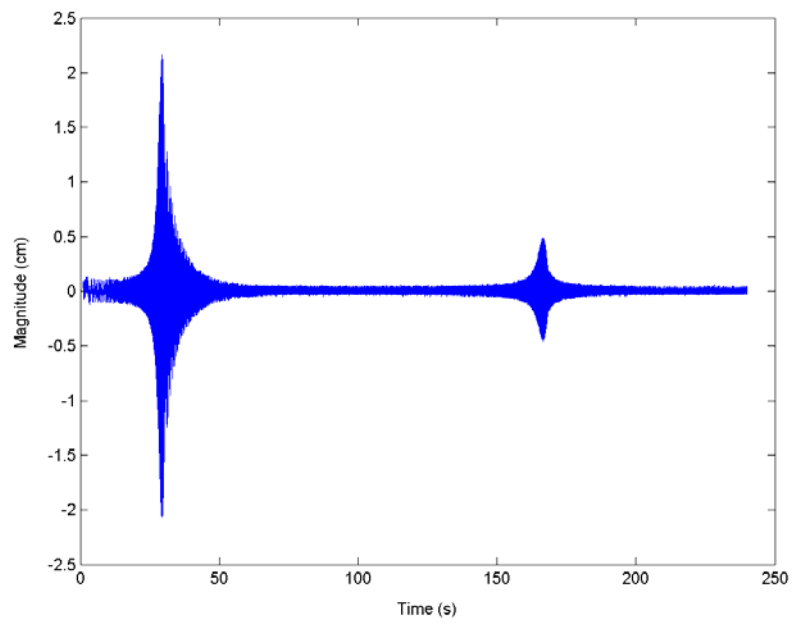


Figure 3.13: Time response of the smart beam measured at  $r=0.9899L_b$

In order to have more accurate information about spatial characteristics of the smart beam, 17 different measurement points, shown in Figure 3.14, were specified. They are defined at 0.03m intervals from tip to the root of the smart beam. The values of the measurement points from the root and their corresponding ratios to the smart beam length are given in Table 3.3.

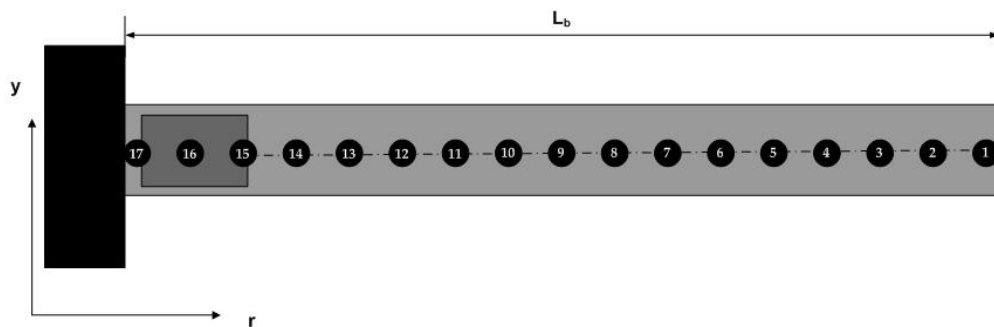


Figure 3.14: The locations of the measurement points

The smart beam was actuated by applying voltage to the piezoelectric patches and the transverse displacements were measured at those locations. Since the smart beam is a spatially distributed system, that analysis resulted in 17 different single input single output system models where all the models were supposed to share the same poles. That kind of analysis yields to determine uncertainty of resonance frequencies due to experimental approach. Besides, comparison of the analytical and experimental system models obtained for each measurement points was used to determine modal damping ratios and the uncertainties on them. That is the reason why measurement from multiple locations was employed. The rest of this section presents the comparison of the analytical and experimental system models to

determine modal damping ratios and clarify the uncertainties on resonance frequencies and modal damping ratios.

Table 3.3: The measurement points and their ratios to the length of the smart beam.

<b>Point</b>	$r/L_b$	<b>Distance from root (m)</b>
1	0.9899	0.489
2	0.9291	0.459
3	0.8684	0.429
4	0.8077	0.399
5	0.7470	0.369
6	0.6862	0.339
7	0.6255	0.309
8	0.5648	0.279
9	0.5040	0.249
10	0.4433	0.219
11	0.3826	0.189
12	0.3219	0.159
13	0.2611	0.129
14	0.2004	0.099
15	0.1397	0.069
16	0.0789	0.039
17	0.0182	0.009

Consider the experimental frequency response of the smart beam at point  $r=0.9899 L_b$  given in Figure 3.15:

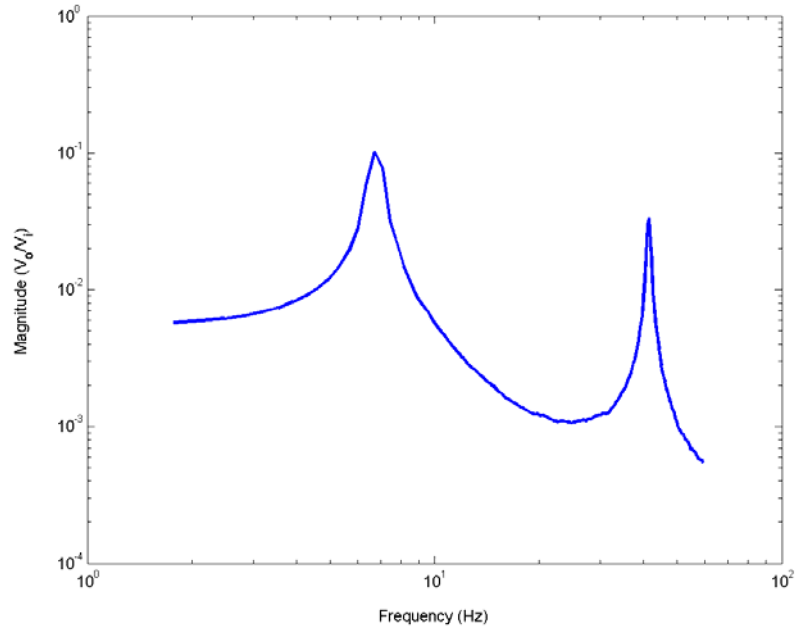


Figure 3.15: Experimental frequency response of the smart beam at  $r=0.9899L_b$

Because experimental frequency analysis is based upon the exact dynamics of the smart beam, the values of the resonance frequencies determined from experimental identification were accepted more accurate than the ones obtained analytically, where the analytical values are presented in Table 3.2. Hence, the first two resonance frequencies were extracted as 6.728 Hz and 41.433 Hz from experimental system given in Figure 3.15. Since the analytical and experimental models should share the same resonance frequencies in order to coincide in the frequency domain, the analytical model for the location  $r=0.9899 L_b$  was coerced to have the same resonance frequencies given above. Notice that, the corresponding measurement point (i.e.

$r=0.9899 L_b$ ) can be selected from any of the measurement locations given in Table 3.3. Also note that, the analytical system model is the corrected model of the form given in equation (3.3). The resultant frequency responses are shown in Figure 3.16.

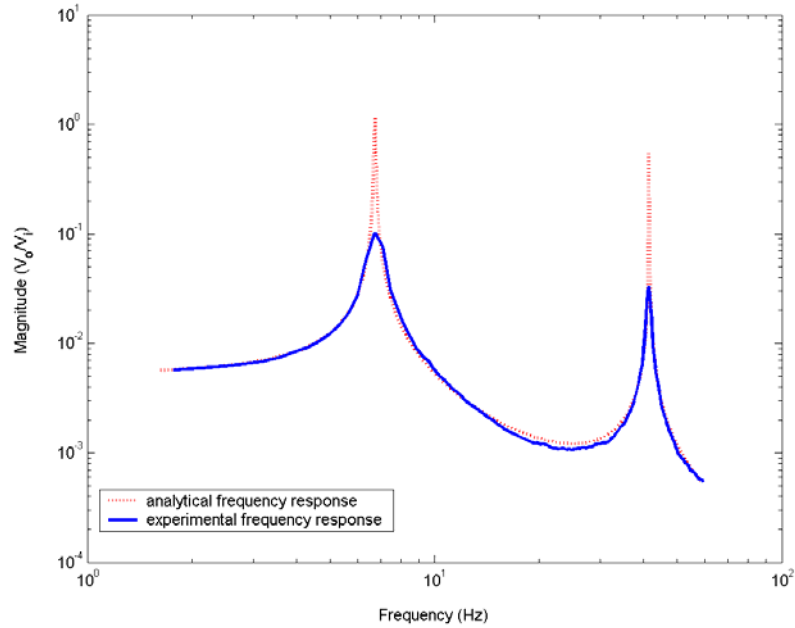


Figure 3.16: Analytical and experimental frequency responses of the smart beam at  $r=0.9899L_b$

The analytical frequency response was obtained by considering the system as undamped. The point  $r=0.9899 L_b$  was selected as measurement point because of the fact that the free end displacement is significant enough for the laser displacement sensor measurements to be more reliable. After obtaining both experimental and analytical system models, the modal damping ratios were tuned until the magnitude of both frequency responses coincide at resonance frequencies, i.e.:

$$\left|G_E(s, r) - \bar{G}_C(s, r)\right|_{\omega=\omega_i} < \lambda \quad (3.7)$$

where  $G_E(s, r)$  is the experimental transfer function and  $\lambda$  is a very small constant term. Similar approach can be employed by minimizing the 2-norm of the differences of the displacements by using least square estimates [44].

Figure 3.17 shows the effect of tuning modal damping ratios on matching both system models in frequency domain where  $\lambda$  is taken as  $10^{-6}$ . Note that each modal damping ratio can be tuned independently.

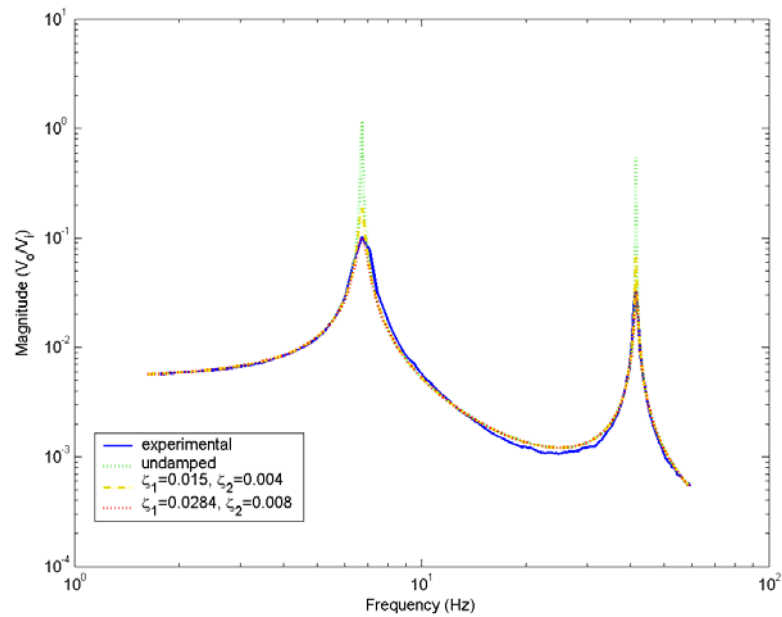


Figure 3.17: Experimental and tuned analytical frequency responses at  $r=0.9899L_b$

Consequently, the first two modal damping ratios were obtained as 0.0284 and 0.008, respectively. As the resonance frequencies and damping ratios are independent of the location of the measurement point, they were used to

obtain the analytical system models of the smart beam for all measurement points. Afterwards, experimental system identification was again performed for each point and both system models were again compared in frequency domain. The experimentally identified flexural resonance frequencies and modal damping ratios determined by tuning are given at Table 3.4 for each point. The frequency responses obtained both analytically and experimentally for various measurement points are shown in Figure 3.18 and Figure 3.19.

Table 3.4: First two flexural resonance frequencies and modal damping ratios  
of the smart beam

$r/L_b$	$\omega_1$ (Hz)	$\omega_2$ (Hz)	$\xi_1$	$\xi_2$
0.9899	6.728	41.433	0.0284	0.008
0.9291	6.740	41.149	0.0282	0.008
0.8684	6.749	41.206	0.0284	0.009
0.8077	6.738	41.135	0.0278	0.008
0.7470	6.742	41.164	0.0256	0.006
0.6862	6.738	41.490	0.0286	0.009
0.6255	6.735	41.121	0.0272	0.007
0.5648	6.745	41.178	0.0300	0.008
0.5040	6.745	41.533	0.0282	0.008
0.4433	6.745	41.178	0.0244	0.007
0.3826	6.745	41.533	0.0256	0.007
0.3219	6.761	41.277	0.0262	0.007
0.2611	6.731	41.093	0.0210	0.006
0.2004	6.735	41.476	0.0290	0.009
0.1397	6.766	41.305	0.0272	0.009
0.0789	6.740	41.504	0.0338	0.012
0.0182	6.733	41.461	0.0520	0.117

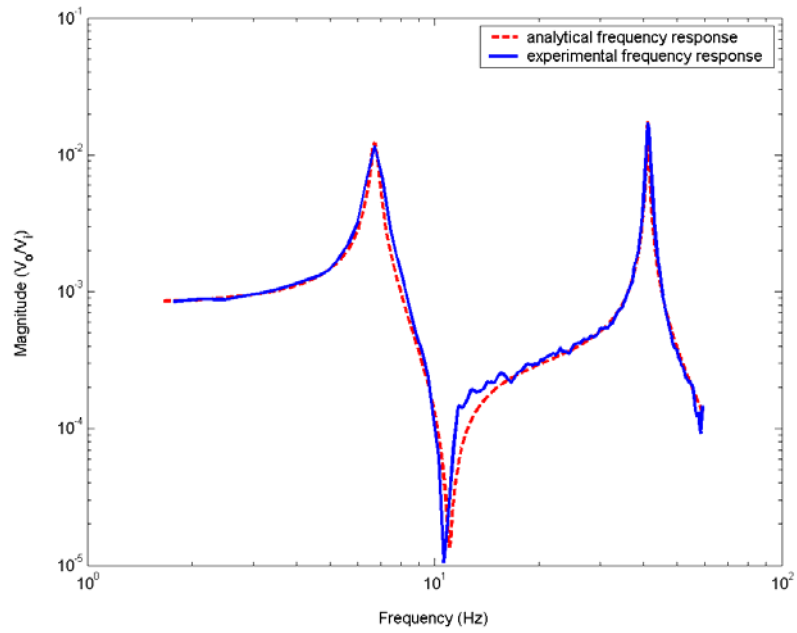


Figure 3.18: Analytical and experimental frequency responses of the smart beam at  $r=0.2611L_b$

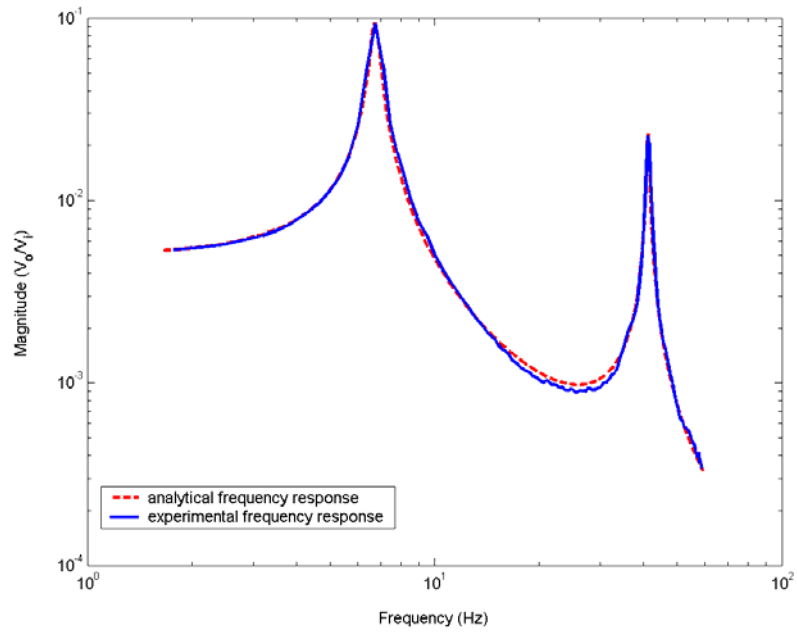


Figure 3.19: Analytical and experimental frequency responses of the smart beam at  $r=0.9291L_b$

The results given in Table 3.4 show that, the corresponding values of the resonance frequencies and the modal damping ratios slightly differ at each measurement point. That is because of the uncertainty due to measurement via laser displacement sensor.

The amount of uncertainty on resonance frequencies and modal damping ratios can be determined by spatial system identification. There are different methods which can be applied to determine the uncertainty and improve the values of the parameters  $\omega$  and  $\xi$  such as boot-strapping [44]. However, in this study the uncertainty is considered as the standard deviation of the parameters and the mean values are accepted as the final values, which are presented at Table 3.5

Table 3.5: Mean and standard deviation of the first two resonance frequencies and modal damping ratios

	$\omega_1$ (Hz)	$\omega_2$ (Hz)	$\xi_1$	$\xi_2$
Mean	6.742	41.308	0.027	0.008
Standard Deviation	0.010	0.166	0.002	0.001

It should be noted that, the modal damping ratio values determined at locations  $r = 0.0789L_b$  and  $r = 0.0182L_b$  are in contradiction with the rest of the others. These are due to the fact that the possibility of sensing by laser displacement sensor is too low because of low flexural displacement close to the fixed end of the smart beam. Hence, while taking the mean and standard deviation of the values, these two data were omitted. Tuning the modal damping terms to satisfy equation (3.7) results in an estimate of the

magnitude of the mode shapes of the smart beam. So, by using the estimated values at the measurement points, the magnitude of the mode shapes at any arbitrary point along the beam can be estimated by interpolation. Figure 3.20 and Figure 3.21 show the analytical and estimated mode shapes normalized with respect to the tip of the beam.

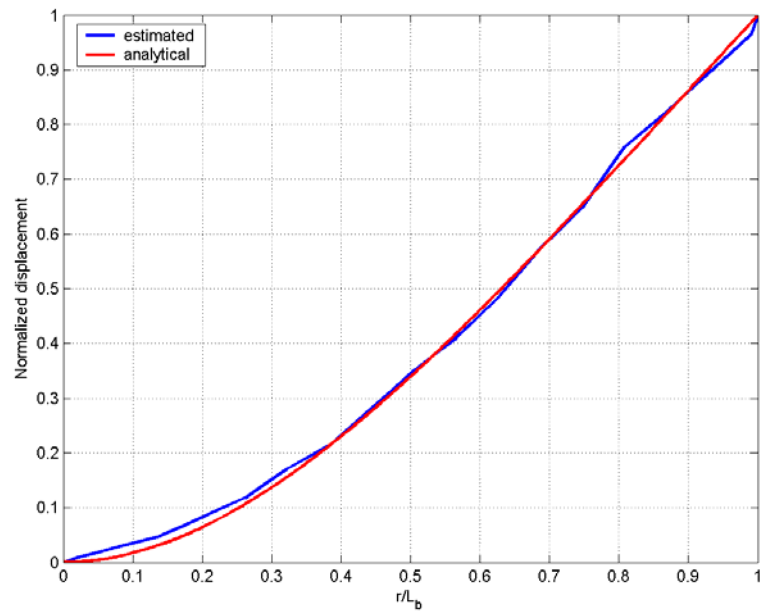


Figure 3.20: First mode shape of the smart beam

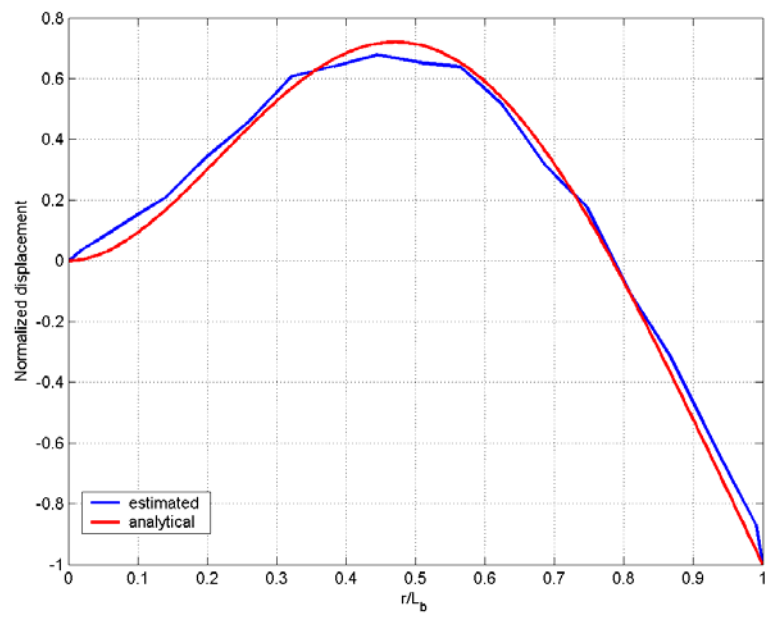


Figure 3.21: Second mode shape of the smart beam

### **3.4 Conclusion**

This chapter described the identification of the smart beam. The system model of the smart beam including the first two flexural modes was corrected by the model correction technique. Later, experimental system identification was employed. And, by using both analytical and experimental system models, the spatial characteristics of the smart beam were obtained. As a result, the system model of the smart beam to be used in spatial control was obtained.

## CHAPTER 4

### ACTIVE CONTROL OF THE SMART BEAM

#### 4.1 Introduction

This chapter describes the methodologies utilized in the active control of the smart beam. The spatial  $H_\infty$  controller was designed for the suppression of first two flexural modes of the smart beam. In order to maintain the simplicity and the clarity, the detailed formulations are given in Appendix D. The simulations conducted showed that the designed controller was performing satisfactorily. The designed controller was then experimentally implemented and the results were demonstrated. Later, a pointwise  $H_\infty$  controller was designed, and the necessary simulations were performed and the implementation was conducted. The two controllers were compared in order to see their effectiveness on suppressing the vibrational levels over the entire beam.

## 4.2 Spatial $H_\infty$ Control of the Smart Beam

### 4.2.1 Controller Design

Consider the closed loop system of the smart beam shown in Figure 4.1. The aim of the controller,  $K$ , is to reduce the effect of disturbance signal over the entire beam by the help of the PZT actuators.

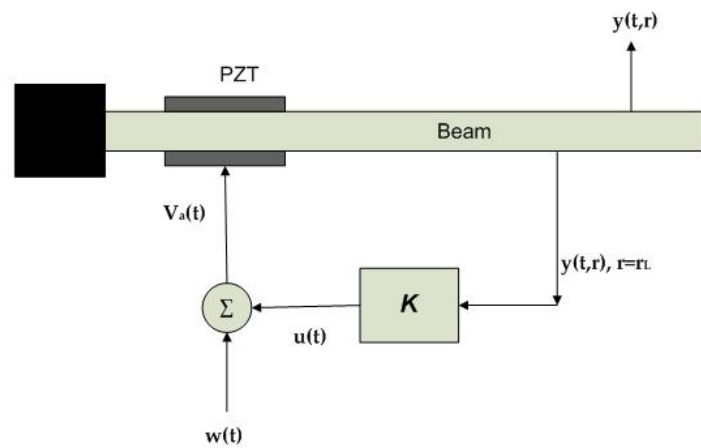


Figure 4.1: The closed loop system of the smart beam

The state space representation of the system above can be shown to be (see Appendix D):

$$\begin{aligned}
 \dot{x}(t) &= Ax(t) + B_1 w(t) + B_2 u(t) \\
 y(t, r) &= C_1(r)x(t) + D_1(r)w(t) + D_2(r)u(t) \\
 y(t, r_L) &= C_2 x(t) + D_3 w(t) + D_4 u(t)
 \end{aligned} \tag{4.1}$$

where all the state space parameters were defined at Section 2.4, except the performance output and the measured output which are now denoted as  $y(t, r)$  and  $y(t, r_L)$ , respectively. The performance output represents the displacement of the smart beam along its entire body, and the measured output represents the displacement of the smart beam at a specific location, i.e.  $r = r_L$ . The disturbance  $w(t)$  is accepted to enter to the system through the actuator channels, hence,  $B_1 = B_2$ ,  $D_1(r) = D_2(r)$  and  $D_3 = D_4$ .

The state space form of the controller design, given in equation (2.62), can now be represented as:

$$\begin{aligned} \dot{x}_k(t) &= A_k x_k(t) + B_k y(t, r_L) \\ u(t) &= C_k x_k(t) + D_k y(t, r_L) \end{aligned} \quad (4.2)$$

Hence, the spatial  $H_\infty$  control problem can be represented as a block diagram which is given in Figure 4.2:

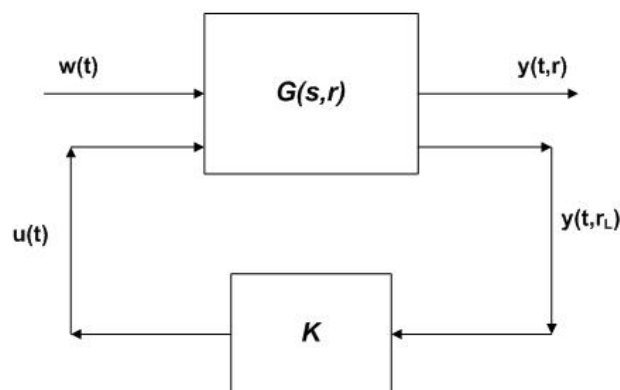


Figure 4.2: The spatial  $H_\infty$  control problem of the smart beam

As stated in Section 2.5, the spatial  $H_\infty$  control problem can be reduced to a standard  $H_\infty$  control problem. The state space representation given in equation (2.74) can be adapted for the smart beam model for a standard  $H_\infty$  control design as:

$$\begin{aligned}
\dot{x}(t) &= Ax(t) + B_1 w(t) + B_2 u(t) \\
\tilde{y}(t) &= \begin{bmatrix} \Pi \\ 0 \end{bmatrix} x(t) + \begin{bmatrix} \Theta_1 \\ 0 \end{bmatrix} w(t) + \begin{bmatrix} \Theta_2 \\ \kappa \end{bmatrix} u(t) \\
y(t, r_L) &= C_2 x(t) + D_3 w(t) + D_4 u(t)
\end{aligned} \tag{4.3}$$

The state space variables given in equations (4.1) and (4.3) can be obtained from the transfer function of equation (3.3) as:

$$A = \begin{bmatrix} 0 & 0 & 1 & 0 \\ 0 & 0 & 0 & 1 \\ -\omega_1^2 & 0 & -2\xi_1\omega_1 & 0 \\ 0 & -\omega_2^2 & 0 & -2\xi_2\omega_2 \end{bmatrix} \tag{4.4}$$

$$B_1 = B_2 = \begin{bmatrix} 0 \\ 0 \\ \bar{P}_1 \\ \bar{P}_2 \end{bmatrix} \tag{4.5}$$

$$C_1 = [\phi_1(r) \quad \phi_2(r) \quad 0 \quad 0] \tag{4.6}$$

$$C_2 = [\phi_1(r_L) \quad \phi_2(r_L) \quad 0 \quad 0] \tag{4.7}$$

$$D_1 = D_2 = \sum_{i=3}^{50} \phi_i(r) k_i^{opt} \quad (4.8)$$

$$D_3 = D_4 = \sum_{i=3}^{50} \phi_i(r_L) k_i^{opt} \quad (4.9)$$

$$\Pi = \begin{bmatrix} L_b^{3/2} & 0 & 0 & 0 \\ 0 & L_b^{3/2} & 0 & 0 \\ 0 & 0 & 0 & 0 \\ 0 & 0 & 0 & 0 \\ 0 & 0 & 0 & 0 \end{bmatrix} \quad (4.10)$$

$$\Theta_1 = \Theta_2 = \begin{bmatrix} 0 \\ 0 \\ 0 \\ 0 \\ \left( \sum_{i=3}^{50} L_b^3 (k_i^{opt})^2 \right)^{1/2} \end{bmatrix} \quad (4.11)$$

The detailed derivation of the above parameters can be found in Appendix D.

One should note that, in the absence of the control weight,  $\kappa$ , the major problem of designing an  $H_\infty$  controller for the system given in equation (4.1) is that, such a design will result in a controller with an infinitely large gain [33]. As described in Section 2.5, in order to overcome this problem, an appropriate control weight, which is determined by the designer, is added to the system. Since the smaller  $\kappa$  will result in higher vibration suppression but larger controller gain, it should be determined optimally such that not

only the gain of the controller does not cause implementation difficulties but also the suppression of the vibration levels are satisfactory. In this study,  $\kappa$  was decided to be taken as  $7.87 \times 10^{-7}$  by trial-and-error. The Bode plot of the resultant spatial  $H_\infty$  controller is shown in Figure 4.3. The simulation of the effect of the controller is shown in Figure 4.4 as a magnitude plot. The frequency domain simulation is done by Matlab v6.5.

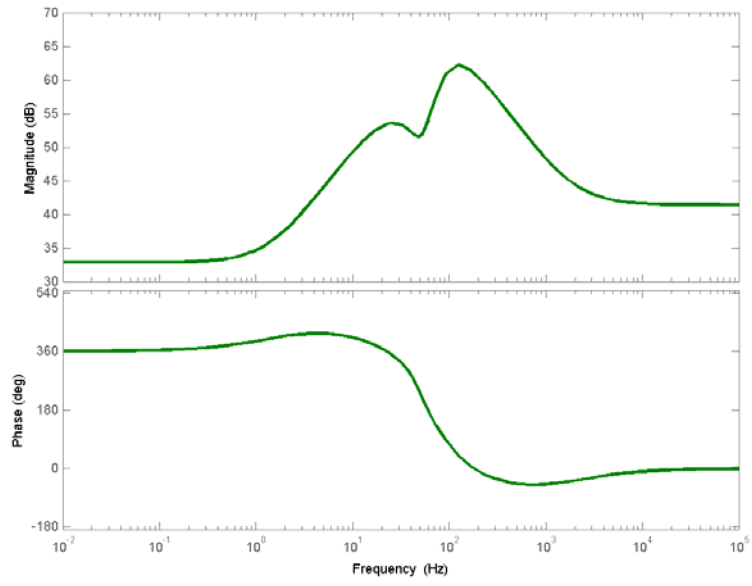


Figure 4.3: Bode plot of the spatial  $H_\infty$  controller

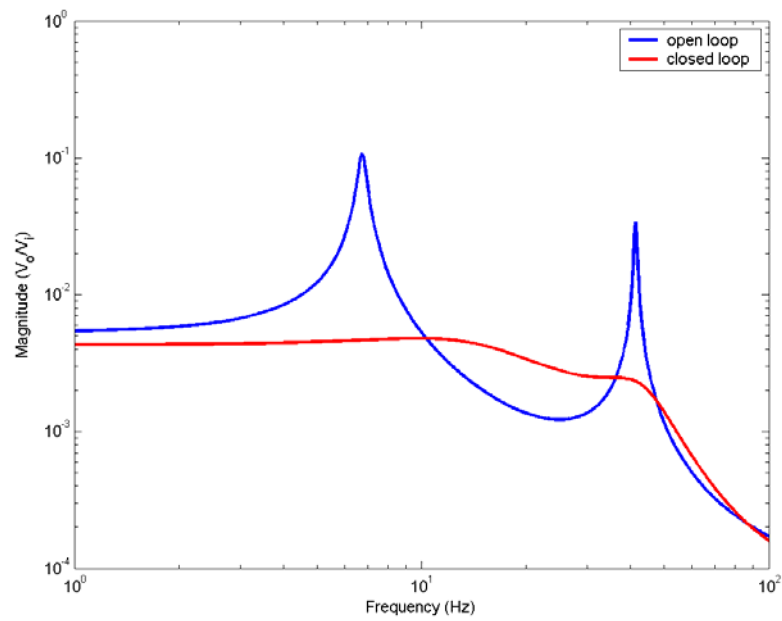


Figure 4.4: Open and closed loop frequency responses of the smart beam under the effect of spatial  $H_\infty$  controller

In order to observe the stability of the system, the Nyquist plot of the nominal system loop gain of the smart beam was analyzed. Figure 4.5 shows that the nominal system is stable since there is no encirclement of the point  $(-1, 0)$  which is the stability criterion of Nyquist [45].

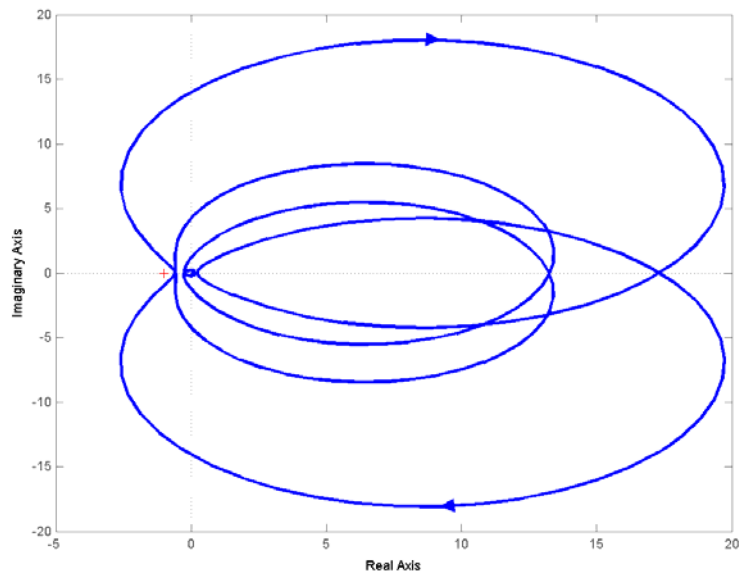


Figure 4.5: Nyquist plot of the nominal system loop gain under the effect of spatial  $H_{\infty}$  controller

The vibration attenuation levels at the first two flexural resonance frequencies were determined from the Bode plots of the controlled and uncontrolled systems shown in Figure 4.6. The resultant attenuation levels of the first two flexural modes were found to be 27.2 dB and 23.1 dB, respectively. The simulated results show that the designed controller is effective on the suppression of undesired vibration levels.

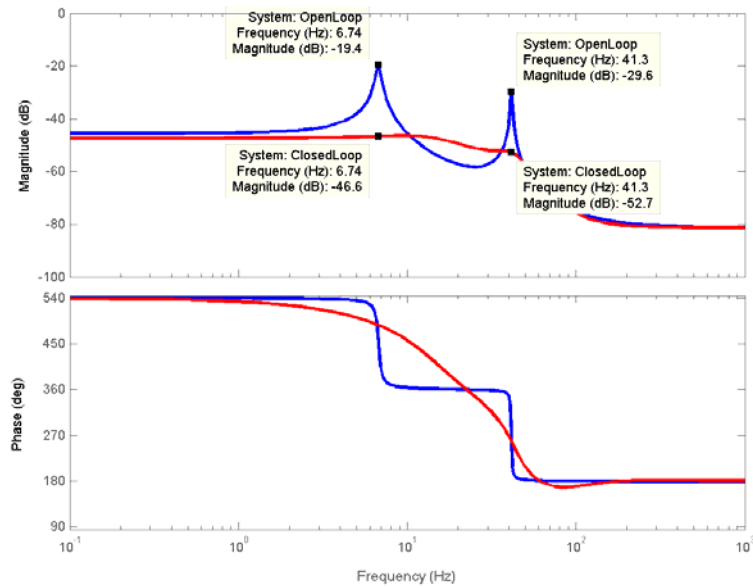


Figure 4.6: Bode plots of the open and closed loop systems under the effect of spatial  $H_{\infty}$  controller

## 4.2.2 Implementation

This section presents the implementation of the spatial  $H_{\infty}$  controller for suppressing the free and forced vibrations of the smart beam. The closed loop experimental setup is shown in Figure 4.7. The displacement of the smart beam at a specific location was measured by using a Keyence Laser Displacement Sensor (LDS) and converted to a voltage output that was sent to the SensorTech SS10 controller unit via the connector block. The controller output was converted to the analog signal and amplified 30 times by SensorTech SA10 high voltage power amplifier before applied to the piezoelectric patches. The controller unit is hosted by a Linux machine on

which a shared disk drive is present to store the input/output data and the C programming language based executable code that is used for real-time signal processing. The hardware properties are detailed in Reference [20]:

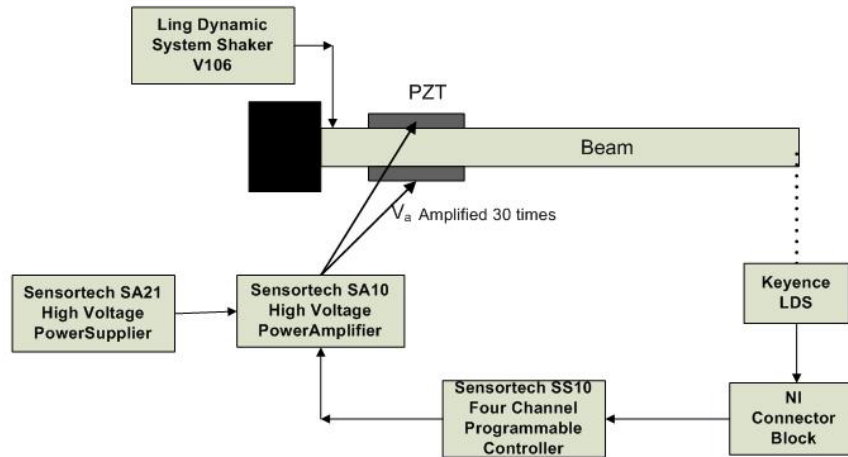


Figure 4.7: The closed loop experimental setup

#### 4.2.2.1 Free Vibration Control of the Smart Beam

For the free vibration control, the smart beam was given an initial 5 cm tip deflection and the open loop and closed loop time responses of the smart beam were measured. The results are presented in Figure 4.8:

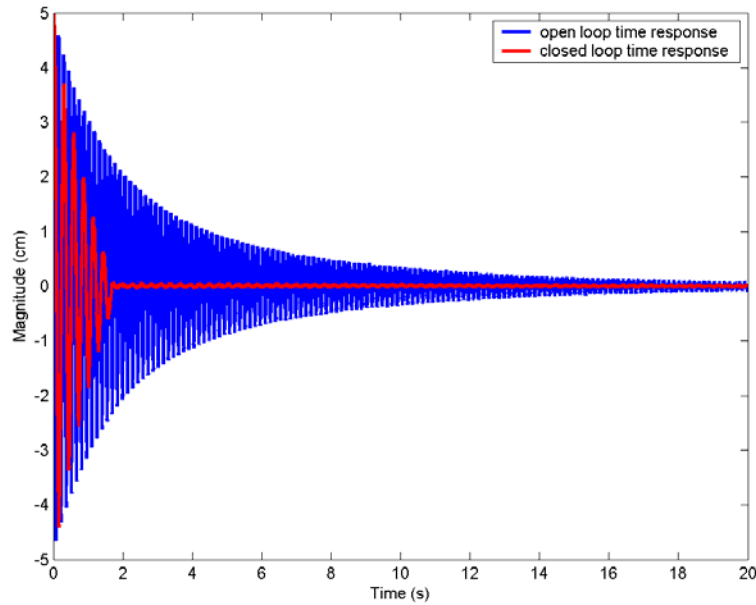


Figure 4.8: Open and closed loop time responses of the smart beam under the effect of spatial  $H_{\infty}$  controller

Figure 4.8 shows that the controlled time response of the smart beam settles nearly in 1.7 seconds. Hence, the designed controller proves to be very effective on suppressing the free vibration of the smart beam.

#### 4.2.2.2 Forced Vibration Control of the Smart Beam

The forced vibration control of the smart beam was analyzed in two different configurations. In the first one, the smart beam was excited for 180 seconds with a shaker located very close to the root of the smart beam, on which a sinusoidal chirp signal of amplitude 4.5V was applied. The excitation bandwidth was taken first 5 to 8 Hz and later 40 to 44 Hz to include the first two flexural resonance frequencies separately. The open loop and closed loop

time and frequency responses of the smart beam under respective excitations are shown in Figure 4.9, Figure 4.10, Figure 4.11 and Figure 4.12.

The experimental attenuation of vibration levels at first two resonance frequencies were determined from the Bode magnitude plots of the frequency responses of the smart beam and shown in Figure 4.13 and Figure 4.14. The resultant attenuation levels were found as 19.8 dB and 14.2 dB, respectively. Hence, the experimental results show that the controller is effective on suppression of the vibration levels. The reason why experimental attenuation levels are less than the simulated ones is that, the excitation power of the shaker was not enough to make the smart beam to reach the larger deflections which in turn causes a smaller magnitude of the open loop time response. The hardware constraints prevent one to apply higher voltages to the shaker. On the other hand, the magnitude of the experimental and simulated closed loop frequency responses at resonance frequencies being close to each other makes one to realize that, the controller works exactly according to the design criteria. Additionally, one should note that the attenuation levels were obtained from the decibel magnitudes of the frequency responses. Hence, a simple mathematical manipulation can give the absolute attenuation levels as a ratio of the maximum time responses of the open and closed loop systems at the specified resonance frequencies.

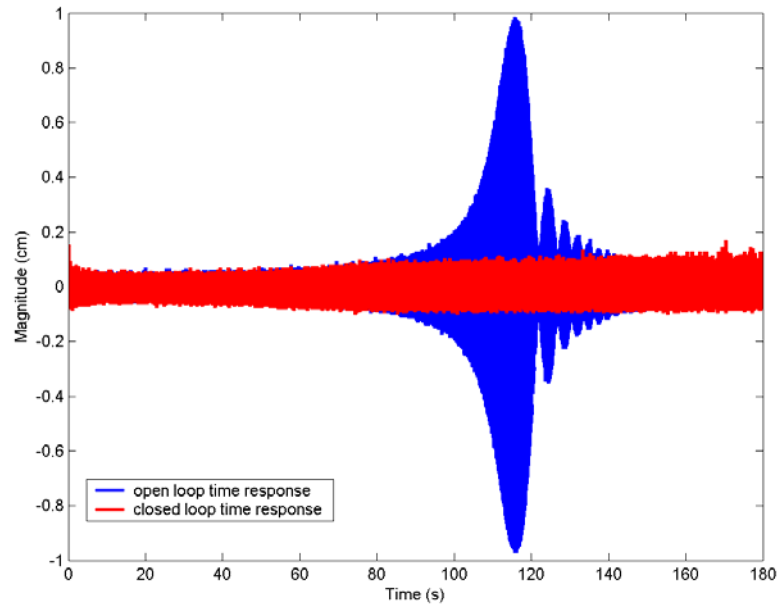


Figure 4.9: Open and closed loop time responses of the smart beam within excitation of 5-8 Hz under the effect of spatial  $H_\infty$  controller

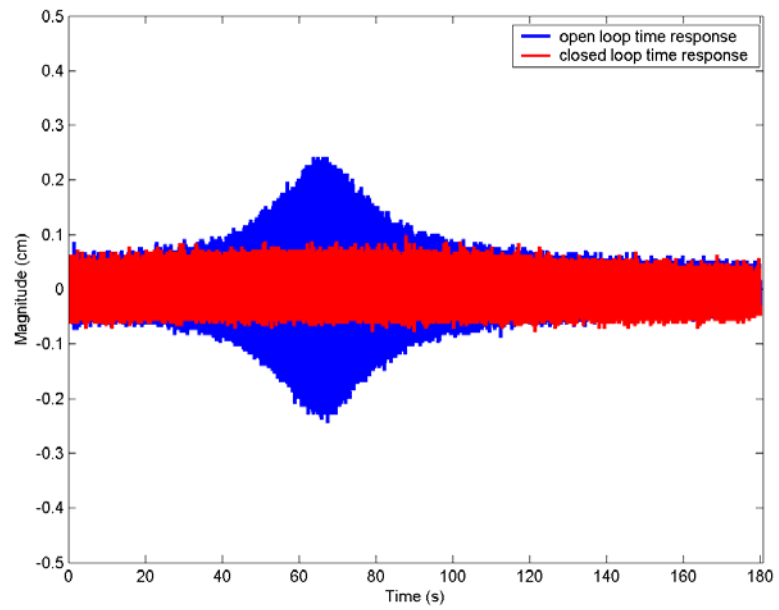


Figure 4.10: Open and closed loop time responses of the smart beam within excitation of 40-44 Hz under the effect of spatial  $H_\infty$  controller

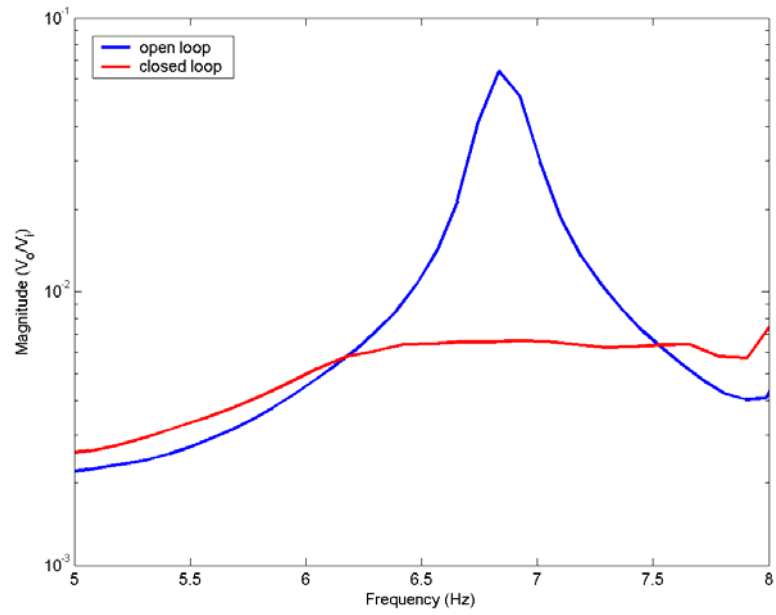


Figure 4.11: Open and closed loop frequency responses of the smart beam within excitation of 5-8 Hz under the effect of spatial  $H_\infty$  controller

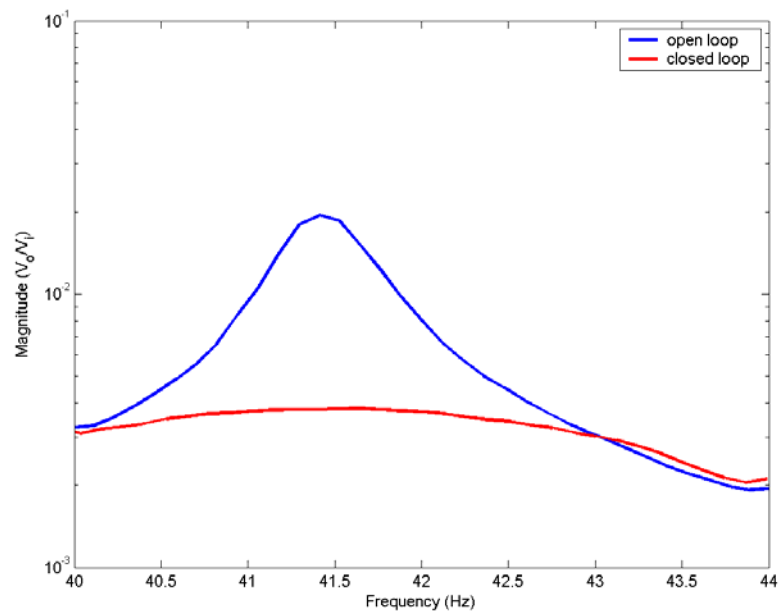


Figure 4.12: Open and closed loop frequency responses of the smart beam within excitation of 40-44 Hz under the effect of spatial  $H_\infty$  controller

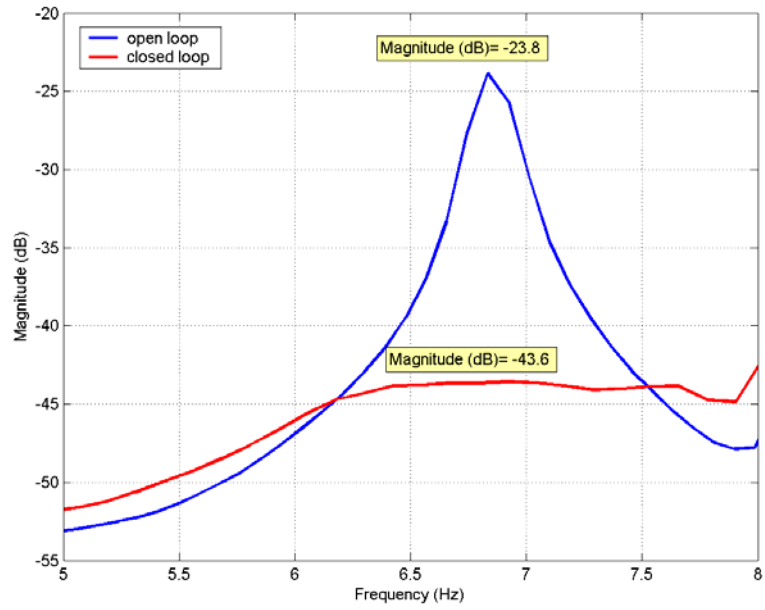


Figure 4.13: Bode magnitude plot of the frequency responses of the open and closed loop systems within excitation of 5-8 Hz under the effect of spatial  $H_\infty$  controller

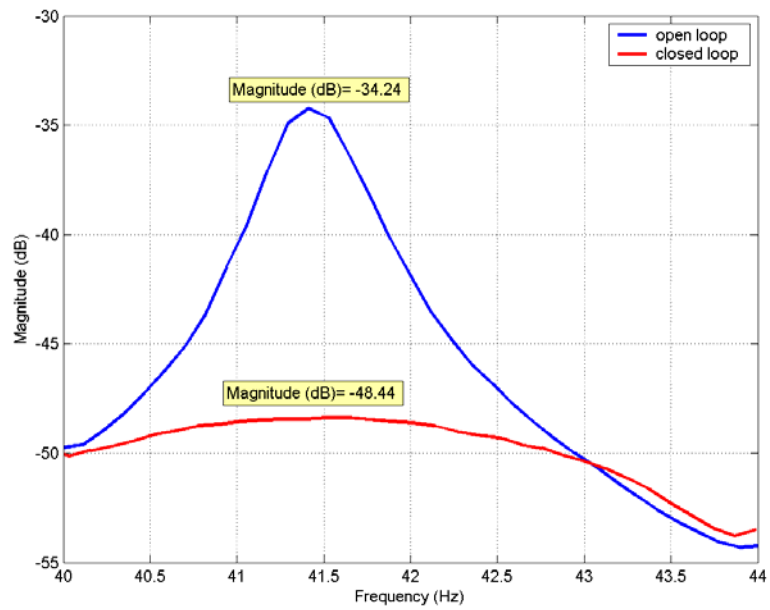


Figure 4.14: Bode magnitude plot of the frequency responses of the open and closed loop systems within excitation of 40-44 Hz under the effect of spatial  $H_\infty$  controller

In the second configuration, instead of using a sinusoidal chirp signal, constant excitation was applied for 20 seconds at the resonance frequencies with a mechanical shaker. The open loop and closed loop time responses of the smart beam were measured and shown in Figure 4.15 and Figure 4.16. Although, it is hard to control such a resonant excitation, the time responses show that the designed controller is still very effective on suppressing the vibration levels. Recall that the ratio of the maximum time responses of the open and closed loop systems can be considered as absolute attenuation levels; hence, for this case, the attenuation levels at each resonance frequency were calculated approximately as 10.4 and 4.17, respectively.

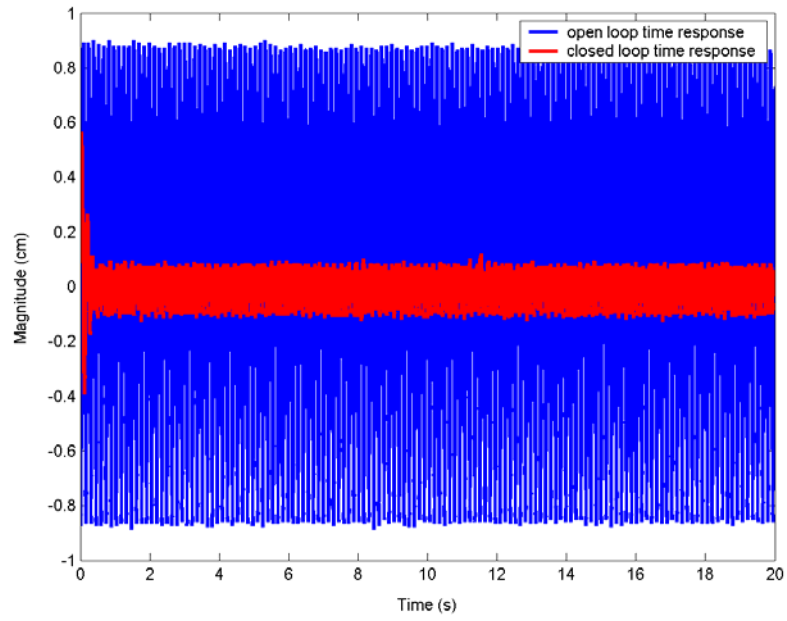


Figure 4.15: Open and closed loop time responses of the smart beam under constant excitation at first resonance frequency under the effect of spatial  $H_\infty$  controller

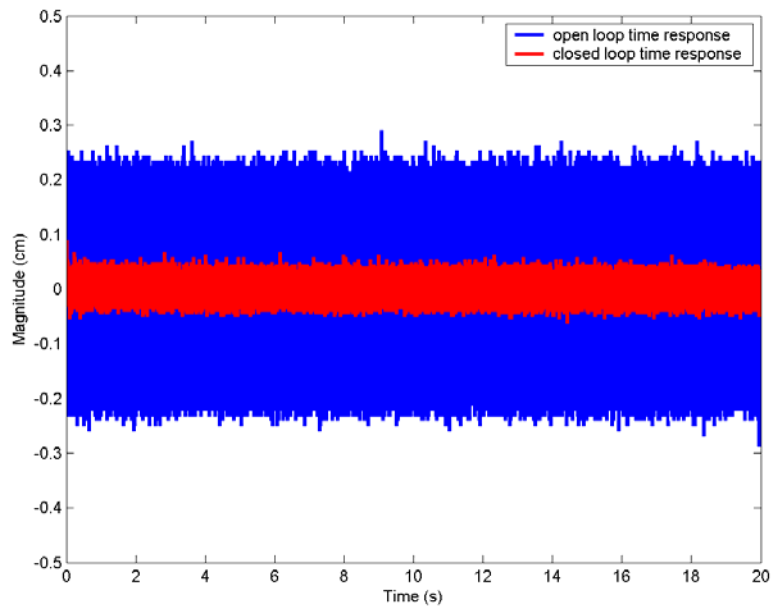


Figure 4.16: Open and closed loop time responses of the smart beam under constant excitation at second resonance frequency under the effect of spatial  $H_\infty$  controller

### 4.3 Pointwise $H_\infty$ Control of the Smart Beam

#### 4.3.1 Controller Design

This section gives only a brief description of pointwise  $H_\infty$  controller design methodology since the scope of this thesis is mainly spatial control. For a more detailed explanation, the interested reader may refer to the references [46, 47]. Consider the general framework of the controller design given in Figure 4.17. The pointwise  $H_\infty$  controller design may yield to fit the general control framework where  $\mathcal{G}$  represents the generalized plant and  $\Delta$  represents the uncertainty block. The feedback diagram of the pointwise  $H_\infty$  controller design is depicted in Figure 4.18.

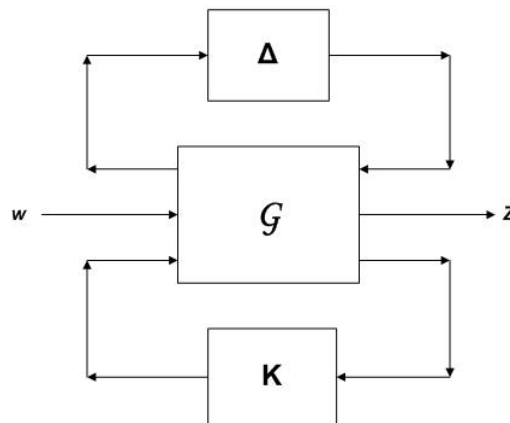


Figure 4.17: General framework for control design

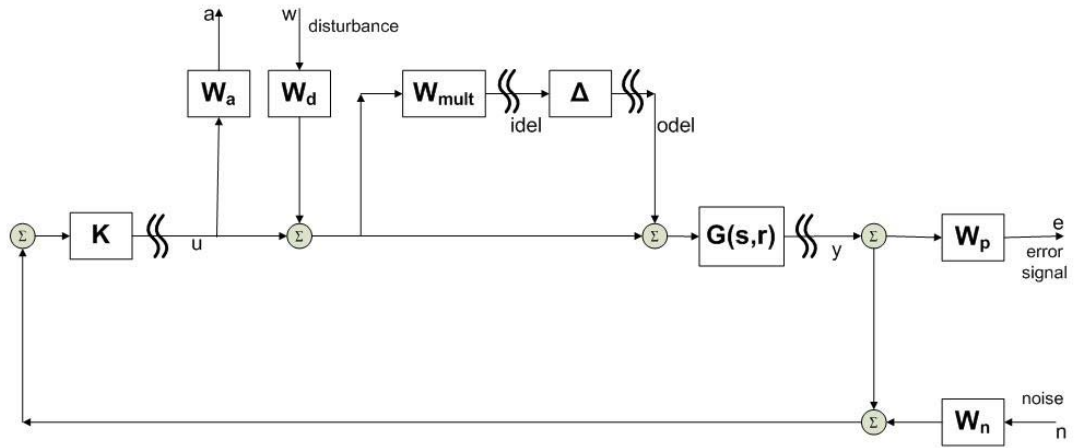


Figure 4.18: General feedback diagram for pointwise  $H_\infty$  controller design

The feedback diagram shown in Figure 4.18 includes the necessary weights representing the design objectives.  $G(s,r)$  is the nominal system model to be controlled. The level of the disturbance,  $w$ , entering to the system through the controller output channel is set by the disturbance weight  $W_d$ .  $W_a$  represents the actuator weight that prevents the actuator saturation,  $W_{mult}$  is the multiplicative, or uncertainty weight, and defines the unmodeled dynamics of the system.  $W_p$  is the performance weight which tunes the controller to show higher performance on defined bandwidth and less at the rest of the frequency range, and finally  $W_n$  is the signal to noise ratio which represents the amount of the sensor measurement that is affected by the noise.

The parametric uncertainty may also be included in the general  $H_\infty$  framework on condition that the perturbations are real, i.e. structured uncertainty [47]. In Section 3.4, the identification of the uncertainty on the resonance frequencies and modal damping ratios were given in detail.

However, as shown in (Table 3.5), the standard deviations of the parameters are very small; hence, the perturbed plants do not deviate significantly from the nominal system model. So, the uncertainty on these parameters can be directly included in the frequency domain multiplicative uncertainty.

The selected weights,  $W_p$  and  $W_{mult}$ , are shown in Figure 4.19. The disturbance weight was selected as unity, i.e. the system is directly affected by the disturbance, the signal to noise ratio was selected as 0.01 and the actuator weight was selected as 0.2. The Bode plot of the resultant pointwise  $H_\infty$  controller is shown in Figure 4.20. The simulation of the effect of the controller is given in Figure 4.21 as a magnitude plot, and the stability of the nominal system was again guaranteed. The relevant Nyquist plot is shown in Figure 4.22.

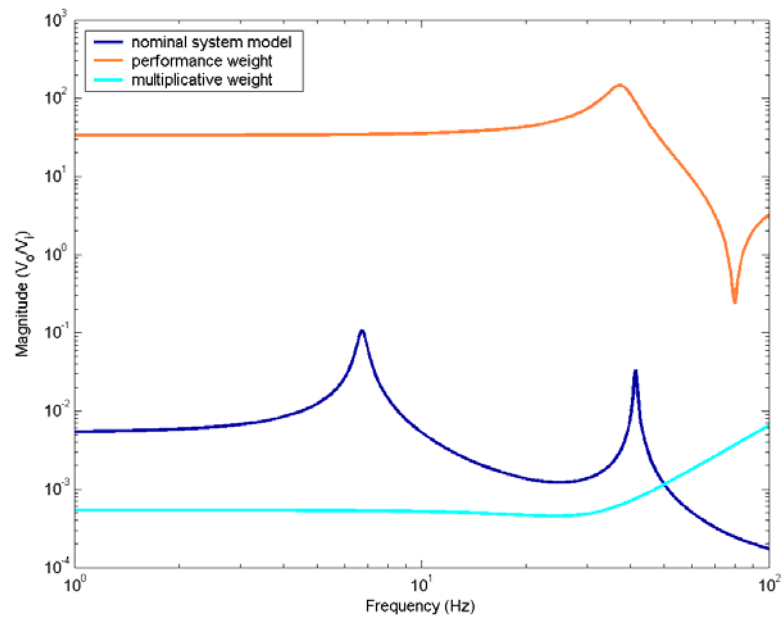


Figure 4.19: Weights for pointwise  $H_\infty$  controller design

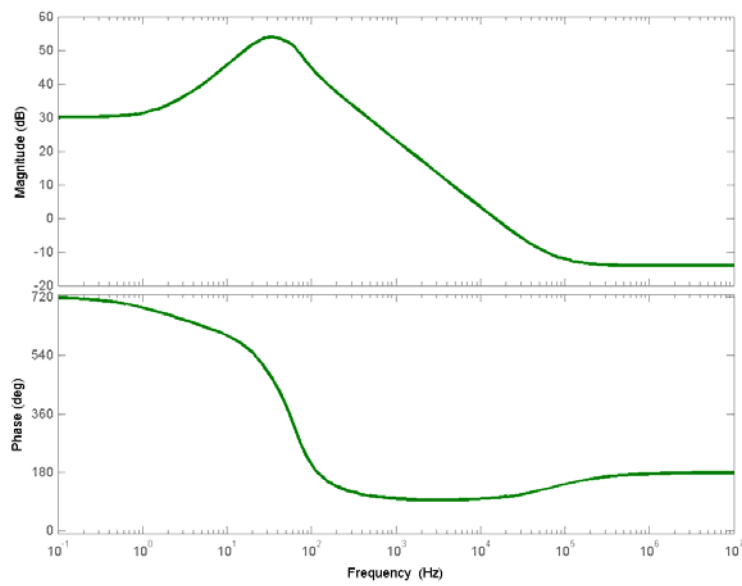


Figure 4.20: Bode plot of the pointwise  $H_\infty$  controller

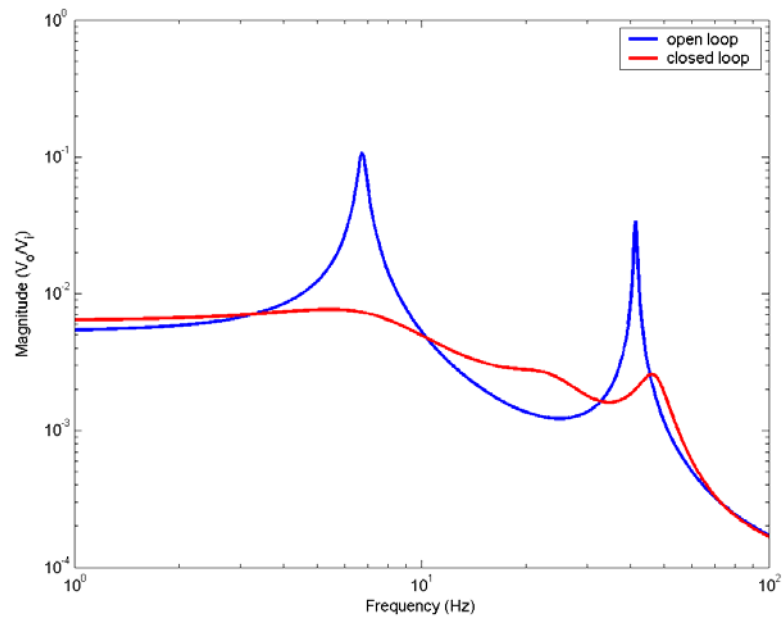


Figure 4.21: Open and closed loop frequency responses of the smart beam under the effect of pointwise  $H_\infty$  controller

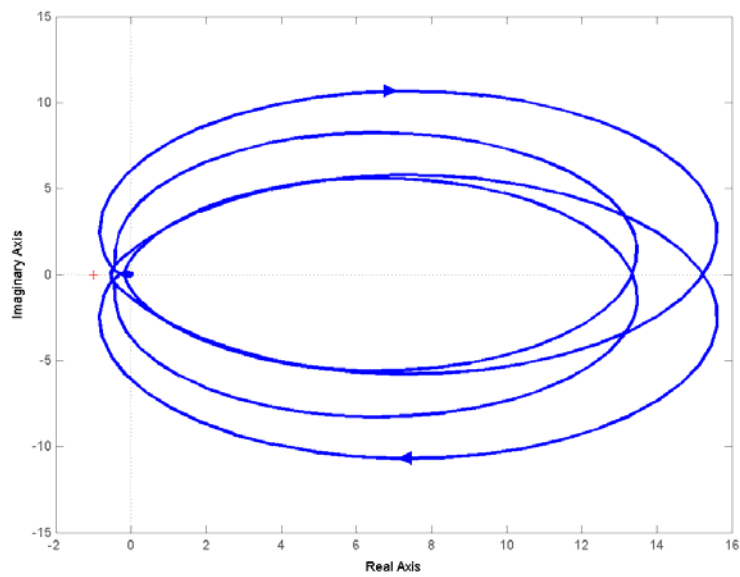


Figure 4.22: Nyquist plot of the nominal system loop gain under the effect of pointwise  $H_\infty$  controller

The vibration attenuation levels can be determined from the Bode plot of the controlled and uncontrolled systems shown in Figure 4.23. The resultant attenuation levels at first two resonance frequencies were found to be 23.5 dB and 24.4 dB, respectively. Hence, the simulated results show that the pointwise controller is also very effective on suppression of the vibration levels.

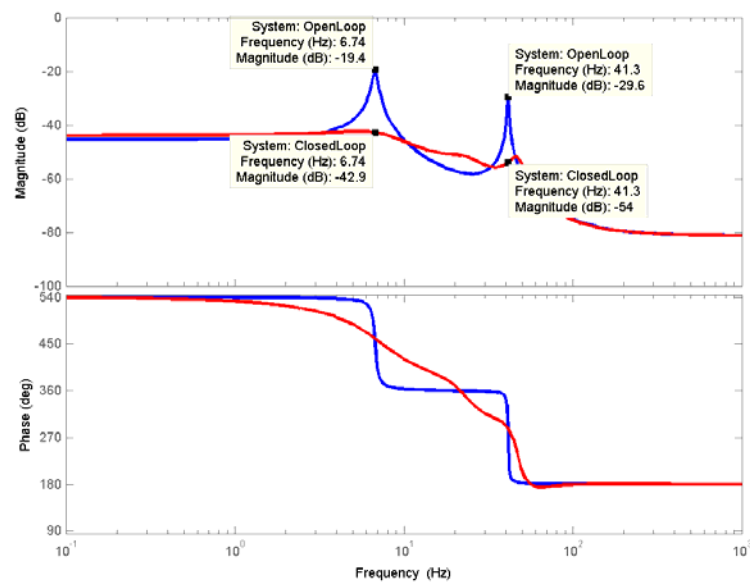


Figure 4.23: Bode plots of the open and closed loop systems under the effect of pointwise  $H_{\infty}$  controller

### 4.3.2 Implementation

This section presents the implementation of the pointwise  $H_\infty$  controller for suppressing the free and forced vibrations of the smart beam. The closed loop experimental setup is shown in Figure 4.7.

#### 4.3.2.1 Free Vibration Control of the Smart Beam

For the free vibration control, the smart beam was given an initial 5 cm tip deflection and the open loop and closed loop time responses of the smart beam were measured. The results are presented in Figure 4.24:

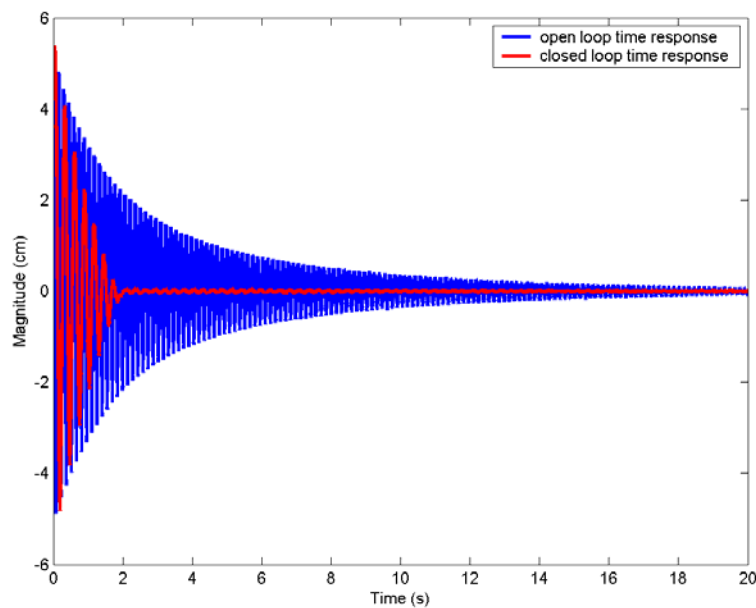


Figure 4.24: Open and closed loop time responses of the smart beam under the effect of pointwise  $H_\infty$  controller

The controlled time response of the smart beam settles nearly in 1.9 seconds. Hence, the pointwise  $H_\infty$  controller is very effective on suppressing the free vibration of the smart beam.

#### 4.3.2.2 Forced Vibration Control of the Smart Beam

The forced vibration control of the smart beam was analyzed in the same two different configurations as considered in spatial controller implementation. The open loop and closed loop time and frequency responses of the smart beam under sinusoidal sweep excitations are shown in Figure 4.25, Figure 4.26, Figure 4.27 and Figure 4.28. The experimental attenuation of vibration levels at first two resonance frequencies were determined from the Bode magnitude plots of the frequency responses of the smart beam given in Figure 4.29 and Figure 4.30. The resultant attenuation levels were found as 21.02 dB and 21.66 dB, respectively. Hence, the experimental results show that the pointwise  $H_\infty$  controller is effective on suppression of the vibration levels. In the second configuration, the open loop and closed loop time responses of the smart beam were measured and shown in Figure 4.31 and Figure 4.32. The absolute attenuation levels at each resonance frequencies were calculated approximately as 5.8 and 4.37, respectively.

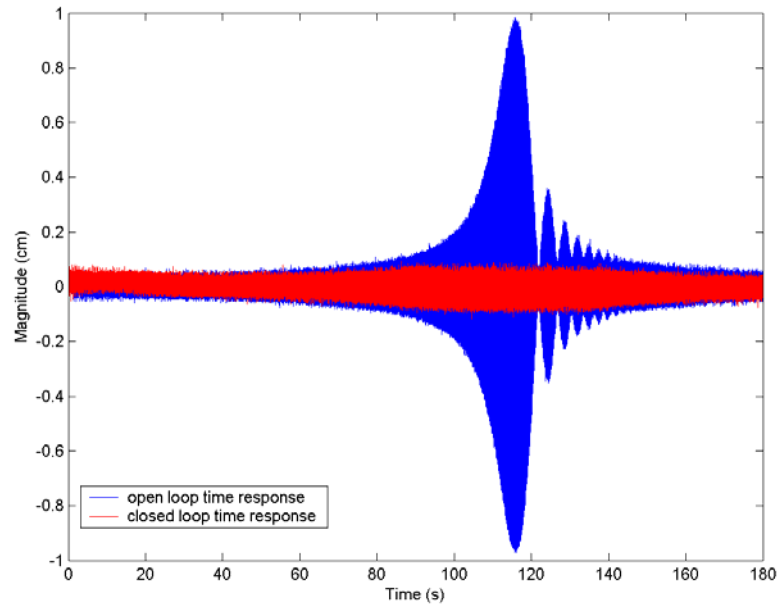


Figure 4.25: Open and closed loop time responses of the smart beam within excitation of 5-8 Hz under the effect of pointwise  $H_\infty$  controller

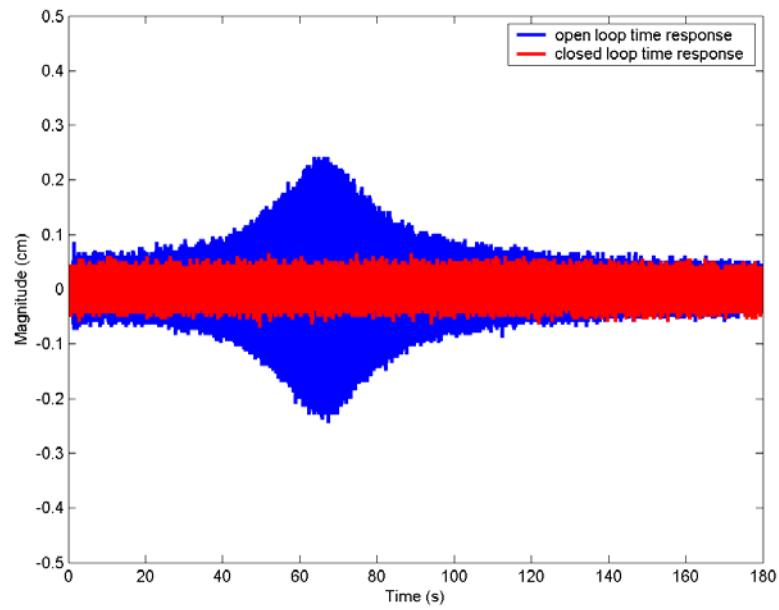


Figure 4.26: Open and closed loop time responses of the smart beam within excitation of 5-8 Hz under the effect of pointwise  $H_\infty$  controller

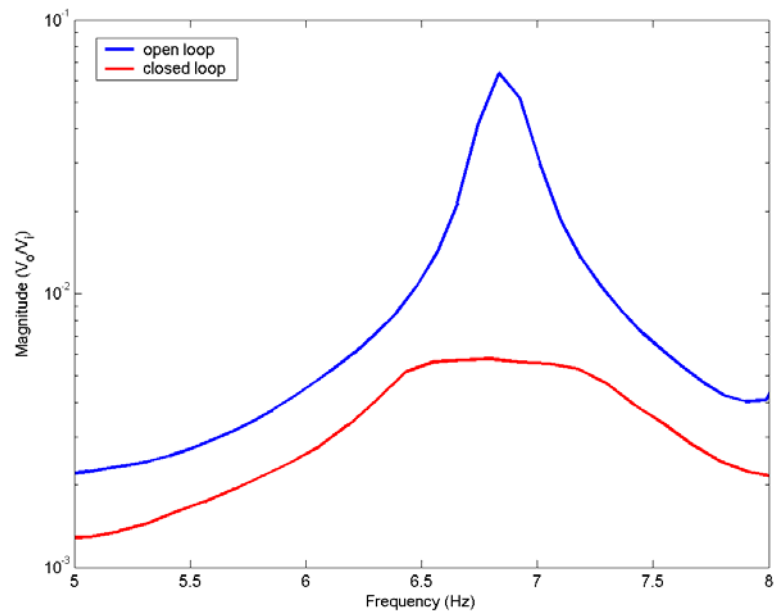


Figure 4.27: Open and closed loop frequency responses of the smart beam within excitation of 5-8 Hz under the effect of pointwise  $H_\infty$  controller

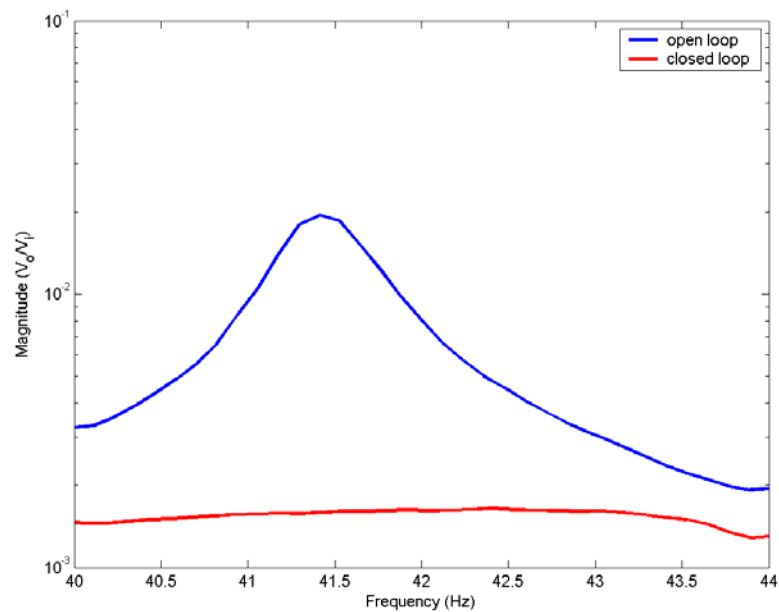


Figure 4.28: Open and closed loop frequency responses of the smart beam within excitation of 40-44 Hz under the effect of pointwise  $H_\infty$  controller

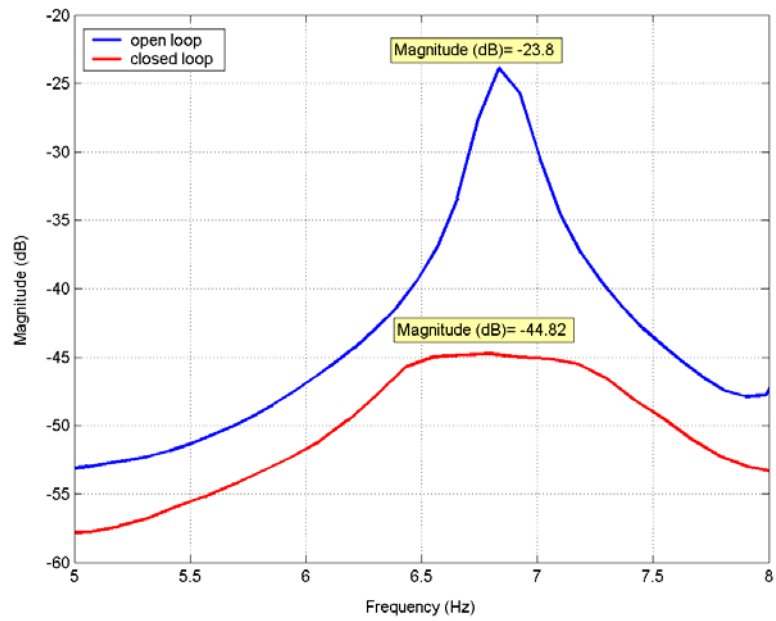


Figure 4.29: Bode magnitude plot of the frequency responses of the open and closed loop systems within excitation of 5-8 Hz under the effect of pointwise  $H_\infty$  controller

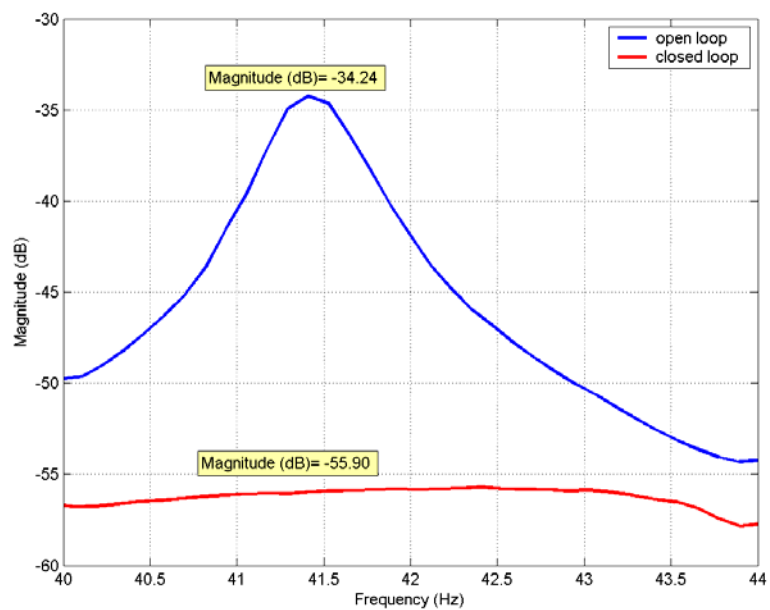


Figure 4.30: Bode magnitude plot of the frequency responses of the open and closed loop systems within excitation of 40-44 Hz under the effect of pointwise  $H_\infty$  controller

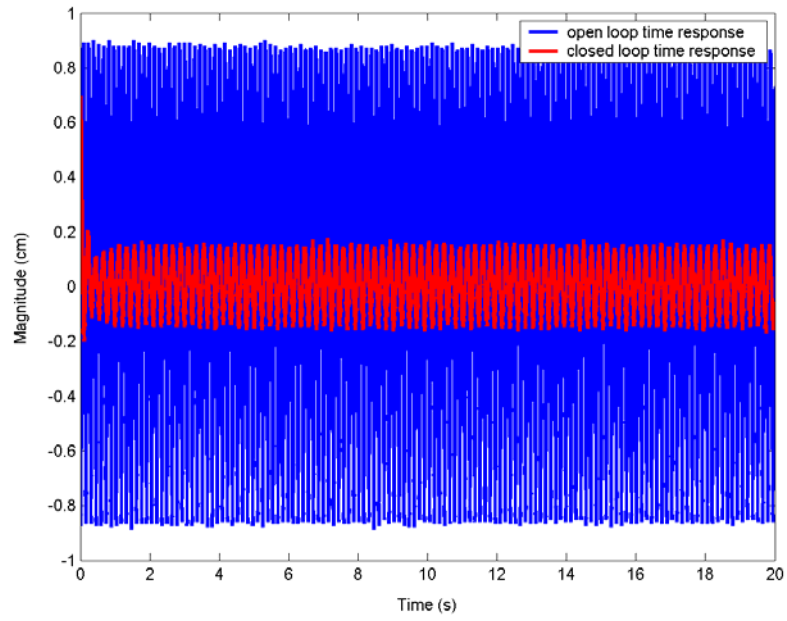


Figure 4.31: Open and closed loop time responses of the smart beam under constant excitation at first resonance frequency under the effect of pointwise  $H_\infty$  controller

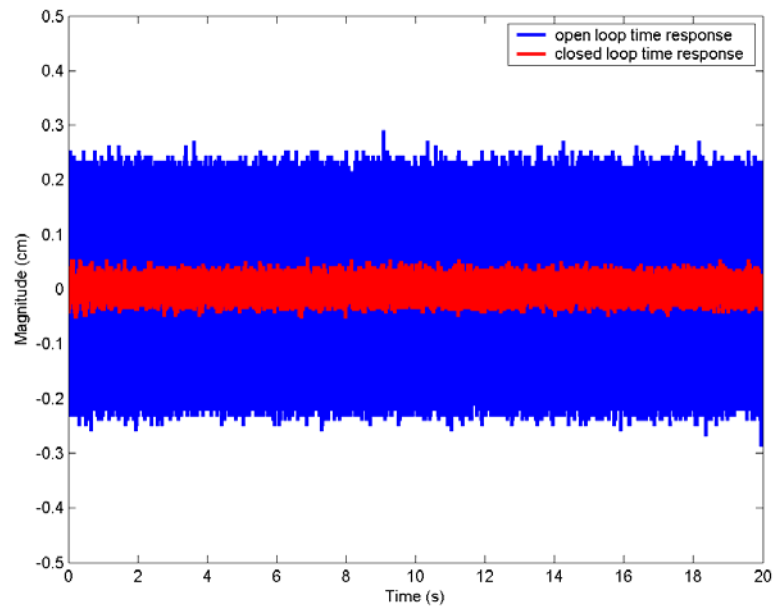


Figure 4.32: Open and closed loop time responses of the smart beam under constant excitation at second resonance frequency under the effect of pointwise  $H_\infty$  controller

#### 4.4 Comparison of Pointwise and Spatial $H_\infty$ Controllers

The comparative effects of the spatial and pointwise  $H_\infty$  controllers on suppressing the first two flexural vibrations of the smart beam are presented in Table 4.1:

Table 4.1: The comparison of attenuation levels under the effect of spatial and pointwise  $H_\infty$  controllers in forced vibrations

Modes	Spatial $H_\infty$ controller		Pointwise $H_\infty$ controller	
	1 <sup>st</sup> mode	2 <sup>nd</sup> mode	1 <sup>st</sup> mode	2 <sup>nd</sup> mode
Simulated attenuation levels (dB)	27.2	23.1	23.5	24.4
Experimentally obtained attenuation levels (dB)	19.8	14.2	21.02	21.66
Absolute attenuation levels under constant resonant excitation (max. OL time response/ max. CL time response)	10.4	4.17	5.75	4.37

The simulations show that both controllers work efficiently on suppressing the vibration levels. The forced vibration control experiments of first configuration show that the attenuation levels of pointwise controller are slightly higher than those of the spatial one. Although the difference is not significant especially for the first flexural mode, better attenuation of

pointwise controller would not be a surprise since the respective design criterion of a pointwise controller is to suppress the undesired vibration level at the specific measurement point. Additionally, absolute attenuation levels show that under constant resonant excitation at the first flexural mode, the spatial  $H_\infty$  controller has better performance than the pointwise one. This is because the design criterion of spatial controller is to suppress the vibration over entire beam; hence, the negative effect of the vibration at any point over the beam on the rest of the other points is prevented by spatial means. So, the spatial  $H_\infty$  controller resists more robustly to the constant resonant excitation than the pointwise one.

The effect of both controllers on suppressing the first two flexural vibrations of the smart beam over entire structure can be analyzed by considering the  $H_\infty$  norm of the entire beam. Figure 4.33 and Figure 4.34 show the plots of  $H_\infty$  norm of the controlled (closed loop) and uncontrolled (open loop) smart beam as a function of  $r$ . Finally, Figure 4.35 shows the  $H_\infty$  norm plots of the smart beam as a function of  $r$  under the effect of both controllers.

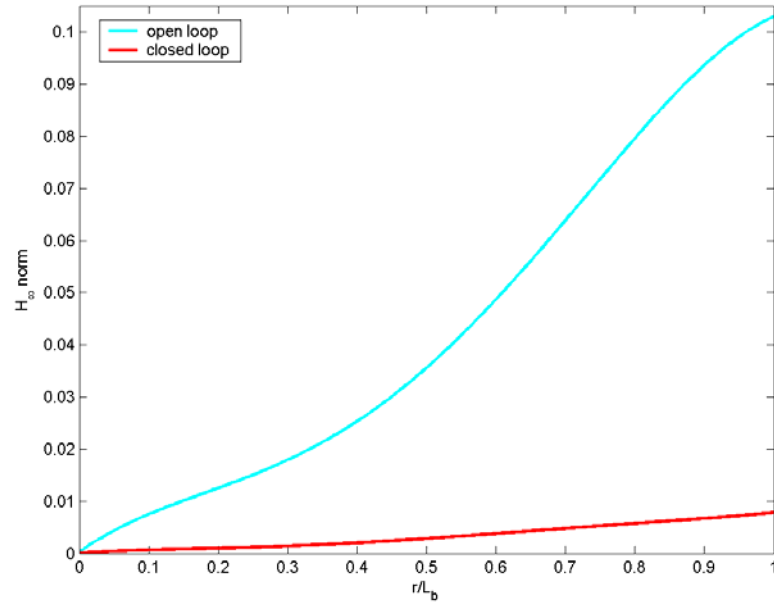


Figure 4.33: Simulated  $H_\infty$  norm plots of open loop and closed loop systems under the effect of pointwise  $H_\infty$  controller

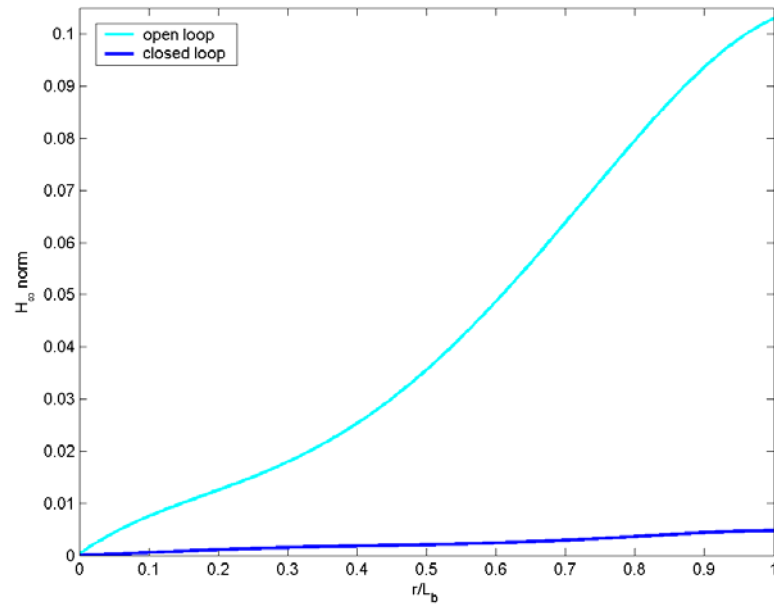


Figure 4.34: Simulated  $H_\infty$  norm plots of open loop and closed loop systems under the effect of spatial  $H_\infty$  controller

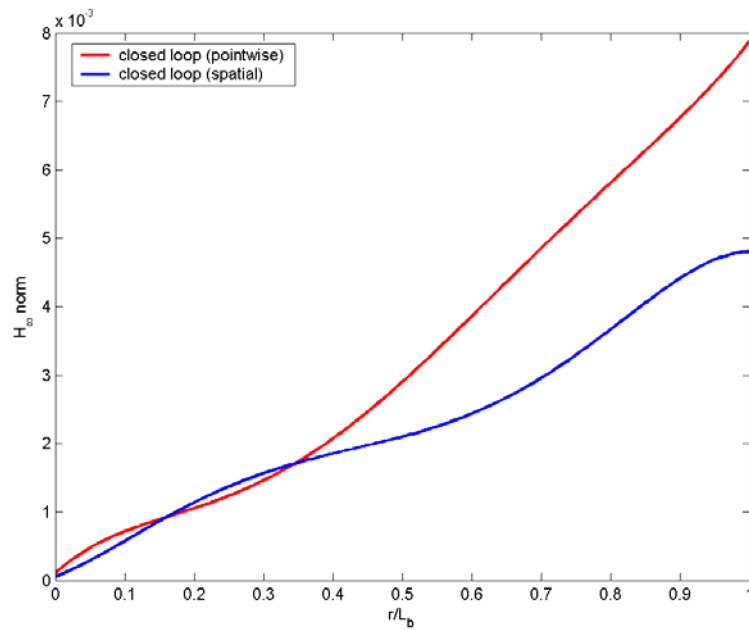


Figure 4.35: Simulated  $H_\infty$  norm plots of closed loop systems under the effect of pointwise and spatial  $H_\infty$  controllers

The robustness analysis of the designed controllers is also an important issue, since the controlled system should resist to the uncertainties in order to preserve a consistency. As given in Figure 4.17, the general control framework includes the uncertainty block so as to represent all the perturbed plants as an uncertainty set. In order to maintain robust stability, the designed controller should keep the system stable for all plants in that uncertainty set. However, stability by only itself cannot guarantee the robustness. Beside satisfying the nominal performance, the system should also resist to the exogenous disturbances (such as noise) acting on itself in order to keep the possible errors due to that disturbances small, which can be defined as the robust performance.

The robustness analysis of the designed controllers was performed by Matlab v6.5  $\mu$ -synthesis toolbox. The results are presented in Figure 4.36 and Figure 4.37. The theoretical background of  $\mu$ -synthesis is detailed in the References [20, 46, 47]. One should know that the  $\mu$  values should be less than unity to accept the controllers to be robust. The Figure 4.36 and Figure 4.37 show that both spatial and pointwise  $H_\infty$  controllers are robust to the perturbations.

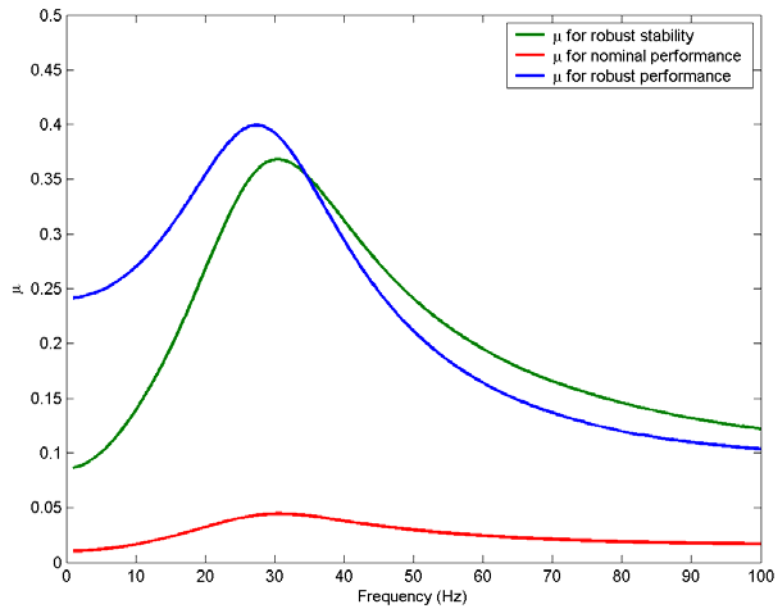


Figure 4.36:  $\mu$ -analysis for spatial  $H_\infty$  controller

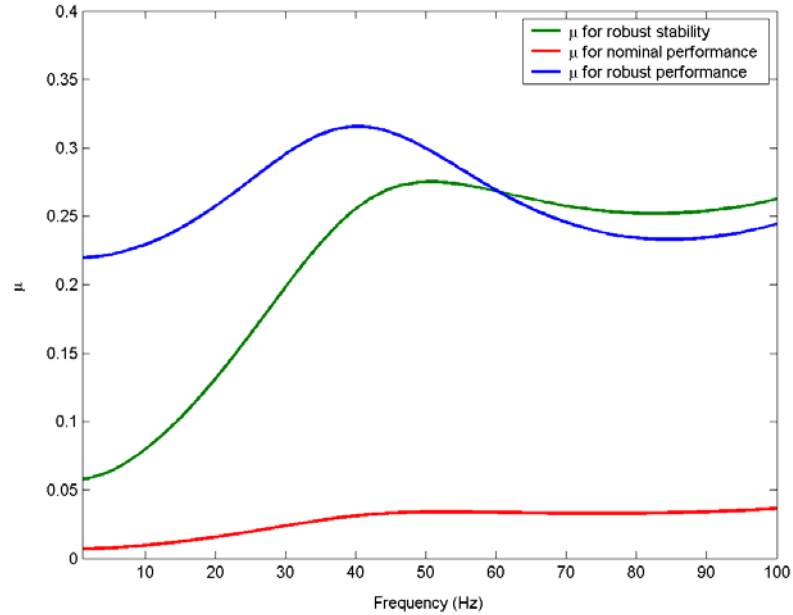


Figure 4.37:  $\mu$ -analysis for pointwise  $H_\infty$  controller

## 4.5 Conclusion

This chapter described the methodologies developed and implemented in the active vibration control of the smart beam. First, a spatial  $H_\infty$  controller was designed for suppressing the first two flexural vibrational levels of the smart beam and the effect of the controller was demonstrated by simulations. The experimental implementation of the spatial  $H_\infty$  controller was also performed and successful attenuation of the vibration levels was achieved. Later, a pointwise  $H_\infty$  controller was designed based on the same performance criteria. The simulations and experimental results were showed that, the pointwise  $H_\infty$  controller was also effective to suppress the vibrations. Finally, the comparison of both controllers was conducted. Although both controllers were robust and effective on suppressing the vibrations of the smart beam, the results showed that the spatial  $H_\infty$  controller has a slight superiority over the pointwise  $H_\infty$  controller in attenuating the vibration levels of the entire structure.

## CHAPTER 5

### GENERAL CONCLUSIONS AND RECOMMENDATIONS

#### 5.1 General Conclusions

This thesis presented a different approach in active vibration control of a cantilevered smart beam.

The required mathematical modeling of the smart beam was conducted by using the assumed-modes method. This inevitably resulted in a high order model including a large number of resonant modes of the beam. This higher order model was truncated to a lower model by including only the first two flexural vibrational modes of the smart beam. The possible error due to that model truncation was compensated by employing a model correction technique which considered the addition of a correction term that consequently minimized the weighted spatial  $H_2$  norm of the truncation error. Hence, the effect of out-of-range modes on the dynamics of the system was included by the correction term.

This study first presented the modeling and identification aspects of a smart beam. The results showed that for the case of cantilevered smart beam the

eigenfunctions of the respective cantilevered passive beam can be utilized as the assumed modes of the smart beam. During the modeling phase the effect of piezoelectric patches was also conveniently included in the model to increase the accuracy of the system model. Additionally, the model correction helps one to obtain more proper system model in the frequency range of interest and the utilized model correction decreases the uncertainty due to the unmodeled high frequency dynamics. However, the assumed-modes modeling alone does not provide any information about the damping of the system. It was shown that experimental system identification, when used in collaboration with the analytical model, helps one to obtain more accurate spatial characteristics of the structure. Since the smart beam is a spatially distributed structure, experimental system identification based on several measurement locations along the beam results in a number of system models providing the spatial nature of the beam. Comparison of each experimental and analytical system models in the frequency domain yields a significant improvement on the determination of the resonance frequencies and helps one to identify the uncertainty on them. Also, tuning the modal damping ratios until the magnitude of both frequency responses coincide at resonance frequencies gives valid damping values and the corresponding uncertainty for each modal damping ratio.

This study also presented the active vibration control of the smart beam. A spatial  $H_\infty$  controller was designed for suppressing the first two flexural vibrations of the smart beam. The efficiency of the controller was demonstrated both by simulations and experimental implementation. Later, a pointwise  $H_\infty$  controller was designed and the efficiency of it was again

verified by simulations and experimental implementations. Then the effectiveness of both controllers on suppressing the vibrations of the smart beam over its entire body was compared.

The implementations of the controllers showed that both pointwise and spatial  $H_\infty$  controllers managed to reduce the vibration levels of the cantilevered smart beam due to its first two flexural modes in nearly equal significance and the simulated  $H_\infty$  norms of the smart beam as a function of  $r$  showed that spatial  $H_\infty$  controller has a slight superiority on suppressing the vibration levels over entire beam.

Additionally, this study also proved that, the corrected assumed-modes modeling in collaboration with the experimental system identification yields a more accurate system model to be used in controller design.

## **5.2 Recommendations for Future Work**

The current study only concentrated on a smart beam. Further studies may investigate the implementation of spatial controllers on a two or three-dimensional smart structures like plates and/or shells.

As a further research topic, a robust spatial controller design methodology can be investigated by introducing spatial uncertainties on the system model. The robust spatial controller may be verified experimentally on the cantilevered smart beam.

Another future work subject may be to investigate the efficiency of a spatial controller for suppressing the vibrations of a smart beam and/or plate subjected to aerodynamic loads. Since that kind of aerodynamic load will cause a distributed loading on the structure, the effectiveness of the spatial controller may be tested more clearly.

## REFERENCES

- [1] Çalışkan T., "Smart Materials and Their Applications in Aerospace Structures", PhD Thesis, Middle East Technical University, September 2002
- [2] Mason W.P., "Piezoelectricity, its History and Applications", Journal of Acoustical Society of America, Vol. 70, No. 6, December 1981
- [3] Prasad S.E., Ahmad A., Wheat T.A., "The Role of Smart Structures in Robotics", Canada-US CanSmart Workshop on Smart Materials and Structures, Quebec, Canada Proceedings pp:133-147, 1998
- [4] Crawley E.F., Louis J., "Use of Piezoelectric Actuators as Elements of Intelligent Structures", AIAA Journal Vol. 125, No. 10, pp. 1373-1385, October 1989
- [5] Dimitridis E.K.C., Fuller R., Rogers C. A., "Piezoelectric Actuators for Distributed Vibration Excitation of Thin Plates", Journal of Vibration and Acoustics, Vol. 113, pp. 100-107, January 1991

- [6] Pota H.R., Alberts T.E., "Multivariable Transfer Functions for a Slewing Piezoelectric Laminate Beam", Proceedings IEEE International Conference on Systems Engineering, Japan, September 1992
  
- [7] Halim D., "Vibration Analysis and Control of Smart Structures", PhD. Thesis, School of Electrical Engineering and Computer Science, University of Newcastle, Australia, August 2002
  
- [8] Meirovitch L., "Elements of Vibration Analysis", The McGraw-Hill Company, 1986
  
- [9] Nalbantoğlu V., "Robust Control and System Identification for Flexible Structures", Ph. D. Thesis, University of Minnesota, 1998
  
- [10] Nalbantoğlu V., Bokor J., Balas G., Gaspar P., "System Identification with Generalized Orthonormal Basis Functions: an Application to Flexible Structures", Control Engineering Practice , Vol. 11, pp.245-259, 2003
  
- [11] Hughes P.C., Skelton R.E., "Modal Truncation for Flexible Spacecraft", Journal of Guidance and Control, Vol. 4 No.3, 1981
  
- [12] Balas G., Young P. M., "Control Design for Variations in Structural Natural Frequencies", Journal of Guidance, Control and Dynamics, Vol. 18, No. 2, March-April 1995

- [13] Moheimani S.O.R., Pota H.R., Petersen I.R., "Spatial Balanced Model Reduction for Flexible Structures", Proceedings of the American Control Conference, pp. 3098-3102, Albuquerque, New Mexico, June 1997
  
- [14] Clark R.L., "Accounting for Out-of-Bandwidth Modes in the Assumed Modes Approach: Implications on Colocated Output Feedback Control", Transactions of the ASME, Journal of Dynamic Systems, Measurement, and Control, Vol. 119, pp. 390-395, September 1997
  
- [15] Moheimani S.O.R., "Minimizing the Effect of out of Bandwidth Modes in Truncated Structure Models", Transactions of the ASME, Journal of Dynamic Systems, Measurement, and Control, Vol. 122, pp.237-239, March 2000
  
- [16] Moheimani S.O.R., Clark R.L., "Minimizing the Truncation Error in Assumed Modes Models of Structures", Transactions of the ASME, Journal of Vibration and Acoustics, Vol. 122, pp.332-335, July 2000
  
- [17] Hanagoud S., Obal M. W., Calise A. J., "Optimal Vibration Control by the Use of Piezoceramic Sensors and Actuators", Journal of Guidance, Control and Dynamics, Vol. 15, No. 5, pp. 1199-1206, October 1992

- [18] Bai M., Lin G. M., "The Development of DSP-Based Active Small Amplitude Vibration Control System for Flexible Beams by Using the LQG Algorithms and Intelligent Materials", Journal of Sound and Vibration, 198, Vol. 4, pp. 411-427, 1996
- [19] Yaman Y., Çalışkan T., Nalbantoğlu V., Prasad E., Waechter D., Yan B., "Active Vibration Control of a Smart Beam", Canada-US CanSmart Workshop on Smart Materials and Structures, Montreal, Canada Proceedings pp:137-147, 2001
- [20] Ülker F.D., "Active Vibration Control of Smart Structures", M.S. Thesis, Middle East Technical University, September 2003
- [21] Halim D., Moheimani S.O.R., "Spatial  $H_2$  Control of a Piezoelectric Laminate Beam: Experimental Implementation", IEEE Transactions on Control System Technology, Vol. 10, No:4, July 2002
- [22] Zames G., "Feedback and Optimal Sensitivity: Model Reference Transformations, Multiplicative Seminorms, and Approximate Inverses", IEEE Transactions on Automatic Control, Vol. AC-26, No.2, April 1981
- [23] Francis B. A., Zames G., "On  $H_\infty$  Optimal Sensitivity Theory for SISO Feedback Systems", IEEE Transactions on Automatic Control, Vol. AC-29, No.1, January 1984

- [24] Doyle J. C., Glover K., Khargonekar P.P., Francis B. A., "State-Space Solutions to Standard  $H_2$  and  $H_\infty$  Control Problems", IEEE Transactions on Automatic Control, 34(8), pp. 831-847, August 1989
- [25] Lenz K., Özbay H., "Analysis and Robust Control Techniques for an Ideal Flexible Beam", Control and Dynamic Systems, 57: 369-421, 1993
- [26] Yaman Y., Ülker F. D., Nalbantoğlu V., Çalışkan T., Prasad E., Waechter D., Yan B., "Application of  $H_\infty$  Active Vibration Control Strategy in Smart Structures", AED2003, 3rd International Conference on Advanced Engineering Design, Paper A5.3, Prague, Czech Republic, 01-04 June, 2003
- [27] Yaman Y., Çalışkan T., Nalbantoğlu V., Ülker F. D., Prasad E., Waechter D., Yan B., "Active Vibration Control of Smart Plates by Using Piezoelectric Actuators", ESDA2002, 6th Biennial Conference on Engineering Systems Design and Analysis, Paper APM-018, Istanbul, Turkey, July 8-11, 2002
- [28] Yaman Y., Çalışkan T., Nalbantoğlu V., Prasad E., Waechter D., "Active Vibration Control of a Smart Plate", ICAS2002, International Council of the Aeronautical Sciences, Paper 424, Toronto, Canada, September 8-13, 2002

- [29] Lenz K., Özbay H., Tannenbaum A., Turi J., Morton B., "Robust Control Design for a Flexible Beam Using a Distributed Parameter  $H_\infty$  Method", Proceedings of the 28<sup>th</sup> IEEE Conference on Decision and Control, pp: 2674-2678, 1989
- [30] Moheimani S.O.R, Fu M., "Spatial  $H_2$  Norm of Flexible Structures and its Application in Model Order Selection", International Proceedings of 37<sup>th</sup> IEEE Conference on Decision and Control, Tampa Florida, USA, 1998
- [31] Moheimani S.O.R., Pota H.R., Petersen I.R., "Spatial Control for Active Vibration Control of Piezoelectric Laminates", International Proceedings of 37<sup>th</sup> IEEE CDC, Tampa, Florida, USA, December 1998
- [32] Moheimani S.O.R., Pota H.R., Petersen I.R., "Active Control of Noise and Vibration in Acoustic Ducts and Flexible Structures – a Spatial Control Approach", Proceedings of ACC, Philadelphia, Pennsylvania, USA, June 1998
- [33] Moheimani S.O.R., Petersen I.R., Pota H.R., "Broadband Disturbance Attenuation over an Entire Beam", Journal of Sound and Vibration 227(4): 807-832, 1999

- [34] Halim D., Moheimani S.O.R., "Experimental Implementation of Spatial  $H_\infty$  Control on a Piezoelectric Laminate Beam", IEEE/ASME Transactions on Mechatronics, Vol. 7, No:3, September 2002
- [35] Lee Y.K., "Active Vibration Control of a Piezoelectric Laminate Plate Using Spatial Control Approach", M.S. Thesis, Department of Mechanical Engineering, University of Adelaide, Australia, 2005
- [36] Baz A., Poh S., "Performance of an Active Control System with Piezoelectric Actuators", Journal of Sound and Vibration, 126(2), pp. 327-343, 1988
- [37] Gosavi S.V., Kelkar A.G., "Passivity-Based Robust Control of Piezo-Actuated Flexible Beam", Journal of Vibration and Acoustics, Vol. 126, pp. 260-271, April 2004
- [38] Hughes P.C., "Space Structure Vibration Modes: How Many Exist? Which Ones Are Important?", IEEE Control Systems Magazine, pp. 22-28, February 1987
- [39] Moheimani S.O.R., "Minimizing the Effect of Out-of-Bandwidth Dynamics in the Models of Reverberant Systems That Arise in Modal Analysis: Implications on Spatial  $H_\infty$  Control", Automatica, Vol. 36, pp. 1023-1031, 2000

- [40] Moheimani S.O.R., "Experimental Verification of the Corrected Transfer Function of a Piezoelectric Laminate Beam", IEEE Transactions on Control Systems Technology, Vol. 8, No. 4, pp. 660-666, 2000
- [41] Moheimani S.O.R., Halim D., Fleming A.J., "Spatial Control of Vibration. Theory and Experiments", World Scientific Publishing Co. Pte. Ltd., 2003
- [42] Yaman Y., Ülker F.D., Nalbantoğlu V., Çalışkan T., Prasad E., Waechter D., Yan B., "Application of  $\mu$ -Synthesis Active Vibration Control Technique to a Smart Fin", 6<sup>th</sup> CanSmart, International Workshop on Smart Materials and Structures, Montreal, Canada Proceedings pp:109-118, 2003
- [43] Ljung L., "System Identification: Theory for the User", Prentice-Hall, 1987
- [44] Reinelt W., Moheimani S.O.R., "Identification of a Flexible Beam", In Proceedings of the 8th International Mechatronics Conference, Enschede, Netherlands, 2002
- [45] Kuo B.C., "Automatic Control Systems", 6<sup>th</sup> Ed., Prentice-Hall, 1991
- [46] Zhou K., Doyle J.C., "Essentials of Robust Control", Prentice-Hall, 1998

- [47] Skogestad S., Postlethwaite I., "Multivariable Feedback Control",  
John Wiley & Sons Ltd., 1996
- [48] Bracewell R., "The Impulse Symbol", 3<sup>rd</sup> ed., McGraw-Hill, 1999

## APPENDIX A

### MODELLING OF THE CANTILEVERED PASSIVE BEAM BY ASSUMED MODES METHOD

Consider equation (2.7), which is the equation of motion of an Euler-Bernoulli beam, for  $r^{\text{th}}$  eigenvalue:

$$\frac{d^2}{dr^2} \left[ E_b I_b \frac{d^2 \phi_r}{dr^2} \right] = \rho_b A_b \phi_r \omega_r^2 \quad 0 < r < L_b \quad (\text{A.1})$$

Multiply both sides by  $\phi_s$  and integrate over the length:

$$\int_0^{L_b} \phi_s \frac{d^2}{dr^2} \left[ E_b I_b \frac{d^2 \phi_r}{dr^2} \right] dr = \int_0^{L_b} \phi_s \rho_b A_b \phi_r \omega_r^2 dr \quad (\text{A.2})$$

Consider only the left hand side of the equation (A.2) and denote as *LHS*. By applying the integration by parts, it can be found that:

$$\begin{aligned} LHS &= \int_0^{L_b} \phi_s \frac{d^2}{dr^2} \left[ E_b I_b \frac{d^2 \phi_r}{dr^2} \right] dr \\ &= \phi_s \frac{d}{dr} \left[ E_b I_b \frac{d^2 \phi_r}{dr^2} \right] \Big|_0^{L_b} - \int_0^{L_b} \frac{d}{dr} \left[ E_b I_b \frac{d^2 \phi_r}{dr^2} \right] \frac{d\phi_s}{dr} dr \end{aligned} \quad (\text{A.3})$$

Recall the boundary conditions given in equations (2.8) and (2.11). It can be seen that the first term of the integral (A.3) is zero at the boundaries,  $r=0$  and  $r=L_b$ . Hence, the above equation becomes:

$$LHS = - \int_0^{L_b} \frac{d}{dr} \left[ E_b I_b \frac{d^2 \phi_r}{dr^2} \right] \frac{d\phi_s}{dr} dr \quad (A.4)$$

If one conducts integration by parts one more time, the *LHS* becomes:

$$LHS = - \left\{ \frac{d\phi_s}{dr} \left[ E_b I_b \frac{d^2 \phi_r}{dr^2} \right] \right\} \Big|_0^{L_b} + \int_0^{L_b} \left[ E_b I_b \frac{d^2 \phi_r}{dr^2} \right] \frac{d^2 \phi_s}{dr^2} dr \quad (A.5)$$

Equations (2.9) and (2.10) yield that; the first term of the integral (A.5) is zero at the beam boundaries. Then, *LHS* finally becomes:

$$LHS = \int_0^{L_b} \left[ E_b I_b \frac{d^2 \phi_r}{dr^2} \right] \frac{d^2 \phi_s}{dr^2} dr \quad (A.6)$$

and the equation (A.2) turns out to be:

$$\int_0^{L_b} \left[ E_b I_b \frac{d^2 \phi_r}{dr^2} \right] \frac{d^2 \phi_s}{dr^2} dr = \int_0^{L_b} \phi_s \rho_b A_b \phi_r \omega_r^2 dr \quad (A.7)$$

In equation (A.7) one can define the following:

$$\int_0^{L_b} \rho_b A_b \phi_s \phi_r dr = m_{rs} \quad (A.8)$$

$$\int_0^{L_b} E_b I_b \phi_r'' \phi_s'' dr = k_{rs} \quad (\text{A.9})$$

$$= \omega_r^2 m_{rs}$$

$$\int_0^{L_b} c_r \rho_b A_b \phi_s \phi_r dr = c_{rs} \quad (\text{A.10})$$

$$= c_r m_{rs}$$

The above definitions are symmetrical, i.e.  $m_{rs} = m_{sr}$ .

Substitute equation (2.16) into equation (2.18) and follow the necessary mathematical manipulations as shown below, one can define the kinetic energy  $T(t)$  as:

$$\begin{aligned} T(t) &= \frac{1}{2} \int_0^{L_b} \rho_b A_b \left[ \frac{\partial}{\partial t} \left( \sum_{r=1}^N \psi_r(r) q_r(t) \right) \right]^2 dr \\ &= \frac{1}{2} \int_0^{L_b} \rho_b A_b \left[ \sum_{r=1}^N \psi_r(r) \dot{q}_r(t) \right]^2 dr \\ &= \frac{1}{2} \int_0^{L_b} \rho_b A_b \left[ \sum_{r=1}^N \psi_r(r) \dot{q}_r(t) \right] \left[ \sum_{s=1}^N \psi_s(r) \dot{q}_s(t) \right] dr \\ &= \frac{1}{2} \sum_{r=1}^N \sum_{s=1}^N \left( \int_0^{L_b} \rho_b A_b \psi_r(r) \psi_s(r) dr \right) \dot{q}_r(t) \dot{q}_s(t) \end{aligned} \quad (\text{A.11})$$

So, use the definition given in equation (A.8), the final form of the kinetic energy definition becomes:

$$T(t) = \frac{1}{2} \sum_{r=1}^N \sum_{s=1}^N m_{rs} \dot{q}_r \dot{q}_s \quad (\text{A.12})$$

Similarly, substitute equation (2.16) into equation (2.19):

$$\begin{aligned}
V(t) &= \frac{1}{2} \int_0^{L_b} E_b I_b \left[ \frac{\partial^2}{\partial r^2} \left( \sum_{r=1}^N \psi_r(r) q_r(t) \right) \right]^2 dr \\
&= \frac{1}{2} \int_0^{L_b} E_b I_b \left[ \sum_{r=1}^N \psi_r''(r) q_r(t) \right]^2 dr \\
&= \frac{1}{2} \int_0^{L_b} E_b I_b \left[ \sum_{r=1}^N \psi_r''(r) q_r(t) \right] \left[ \sum_{s=1}^N \psi_s''(r) q_s(t) \right] dr \\
&= \frac{1}{2} \sum_{r=1}^N \sum_{s=1}^N \left( \int_0^{L_b} E_b I_b \psi_r''(r) \psi_s''(r) dr \right) q_r q_s
\end{aligned} \tag{A.13}$$

So, use the definition given in equation (A.9), final form of the potential energy definition becomes:

$$V(t) = \frac{1}{2} \sum_{r=1}^N \sum_{s=1}^N k_{rs} q_r q_s \tag{A.14}$$

Similarly, substitute equation (2.16) into equation (2.20):

$$\begin{aligned}
F(t) &= \frac{1}{2} \int_0^{L_b} c \rho_b A_b \left[ \frac{\partial}{\partial t} \left( \sum_{r=1}^N \psi_r(r) \dot{q}_r(t) \right) \right]^2 dr \\
&= \frac{1}{2} \int_0^{L_b} c \rho_b A_b \left[ \sum_{r=1}^N \psi_r(r) \dot{q}_r(t) \right] \left[ \sum_{s=1}^N \psi_s(r) \dot{q}_s(t) \right] dr \\
&= \frac{1}{2} \sum_{r=1}^N \sum_{s=1}^N \left( \int_0^{L_b} c \rho_b A_b \psi_r(r) \psi_s(r) dr \right) \dot{q}_r \dot{q}_s
\end{aligned} \tag{A.15}$$

So, use the definition given in equation (A.10) and assuming a proportional viscous damping coefficient  $c$  associated with the  $r^{th}$  mode, final form of the viscous damping expression can be written as:

$$F(t) = \frac{1}{2} \sum_{r=1}^N \sum_{s=1}^N c_{rs} \dot{q}_r \dot{q}_s \quad (\text{A.16})$$

Let us write the Lagrange's equation (2.17) as:

$$\begin{aligned} \frac{d}{dt} \left( \frac{\partial(T-V)}{\partial \dot{q}_i} \right) - \frac{\partial(T-V)}{\partial q_i} + \frac{\partial F}{\partial \dot{q}_i} &= Q_i \Rightarrow \\ \frac{d}{dt} \left( \frac{\partial T}{\partial \dot{q}_i} - \frac{\partial V}{\partial \dot{q}_i} \right) - \frac{\partial T}{\partial q_i} + \frac{\partial V}{\partial q_i} + \frac{\partial F}{\partial \dot{q}_i} &= Q_i \Rightarrow \\ \frac{d}{dt} \left( \frac{\partial T}{\partial \dot{q}_i} \right) + \frac{\partial V}{\partial q_i} + \frac{\partial F}{\partial \dot{q}_i} &= Q_i \end{aligned} \quad (\text{A.17})$$

By substituting the expressions of  $T(t)$ ,  $V(t)$  and  $F(t)$ , the final form of the equation (A.17) can be obtained as following:

$$\begin{aligned} \frac{d}{dt} \left( \frac{\partial T}{\partial \dot{q}_i} \right) &= \frac{d}{dt} \left( \frac{\partial}{\partial \dot{q}_i} \left\{ \frac{1}{2} \sum_{r=1}^N \sum_{s=1}^N m_{rs} \dot{q}_r \dot{q}_s \right\} \right) \\ &= \frac{d}{dt} \left( \frac{1}{2} \sum_{r=1}^N \sum_{s=1}^N \left\{ m_{rs} \frac{\partial \dot{q}_r}{\partial \dot{q}_i} \dot{q}_s + m_{rs} \dot{q}_r \frac{\partial \dot{q}_s}{\partial \dot{q}_i} \right\} \right) \end{aligned} \quad (\text{A.18})$$

where:

$$\frac{\partial \dot{q}_r}{\partial \dot{q}_i} = \delta_{ri} \quad \text{and} \quad \frac{\partial \dot{q}_s}{\partial \dot{q}_i} = \delta_{si} \quad (\text{A.19})$$

so, equation (A.18) becomes:

$$\frac{d}{dt} \left( \frac{\partial T}{\partial \dot{q}_i} \right) = \frac{d}{dt} \left( \frac{1}{2} \sum_{r=1}^N \sum_{s=1}^N \{ m_{rs} \delta_{ri} \dot{q}_s + m_{rs} \delta_{si} \dot{q}_r \} \right) \quad (\text{A.20})$$

note that:

$$m_{rs} \delta_{ri} = m_{si} \quad \text{or} \quad m_{rs} \delta_{si} = m_{ri} \quad (\text{A.21})$$

If one substitutes (A.21) into (A.18), it can be found that:

$$\begin{aligned} \frac{d}{dt} \left( \frac{\partial T}{\partial \dot{q}_i} \right) &= \frac{d}{dt} \left( \frac{1}{2} \sum_{r=1}^N \sum_{s=1}^N \{ m_{si} \dot{q}_s + m_{ri} \dot{q}_r \} \right) \\ &= \frac{d}{dt} \left( \frac{1}{2} \sum_{s=1}^N m_{si} \dot{q}_s + \frac{1}{2} \sum_{r=1}^N m_{ri} \dot{q}_r \right) \end{aligned} \quad (\text{A.22})$$

Let's put  $r$  instead of  $s$ , the final form of (A.22) becomes:

$$\begin{aligned} \frac{d}{dt} \left( \frac{\partial T}{\partial \dot{q}_i} \right) &= \frac{d}{dt} \left( \frac{1}{2} \sum_{r=1}^N m_{ri} \dot{q}_r + \frac{1}{2} \sum_{r=1}^N m_{ri} \dot{q}_r \right) \\ &= \frac{d}{dt} \left( \sum_{r=1}^N m_{ri} \dot{q}_r \right) \\ &= \sum_{r=1}^N m_{ri} \ddot{q}_r \quad i = 1, 2, \dots, N \end{aligned} \quad (\text{A.23})$$

As mentioned before  $m_{ri}$  is symmetrical, so the final form of equation (A.23)

becomes:

$$\frac{d}{dt} \left( \frac{\partial T}{\partial \dot{q}_i} \right) = \sum_{r=1}^N m_{ir} \ddot{q}_r \quad i = 1, 2, \dots, N \quad (\text{A.24})$$

Following a similar procedure, one can obtain that:

$$\frac{\partial V}{\partial q_i} = \sum_{r=1}^N k_{ir} q_r \quad i = 1, 2, \dots, N \quad (\text{A.25})$$

and

$$\frac{\partial F}{\partial \dot{q}_i} = \sum_{r=1}^N c_{ir} \dot{q}_r \quad i = 1, 2, \dots, N \quad (\text{A.26})$$

Consequently, substitute (A.24), (A.25) and (A.26) into (A.17) and consider the equalities given in (A.9) and (A.10):

$$\sum_{r=1}^N m_{ir} \{ \ddot{q}_r + \omega_r^2 q_r + c_r \dot{q}_r \} = Q_i \quad (\text{A.27})$$

Rearrange the orthogonality expression given in equation (2.14):

$$\int_0^{L_b} \rho_b A_b \phi_i \phi_j dr = Z \delta_{ij} \quad (\text{A.28})$$

where  $Z$  is a constant. If eigenfunctions are normalized,  $Z$  will be equal to 1. Otherwise, it should be determined. One can easily notice that the left hand sides of equation (A.28) and (A.8) are identical. Hence, substitute the external force expression given in equation (2.23) and the viscous damping coefficient expression given in equation (2.21) into equation (A.27), and for simplicity,  $Z$  is taken as 1, then the general equation of motion will finally be:

$$\ddot{q}_i + 2\xi_i \omega_i \dot{q}_i + \omega_i^2 q_i = P_i u \quad (\text{A.29})$$

This equation, which is in time domain, can be easily transferred to the frequency domain by using Laplace transform with zero initial conditions.

$$s^2 Q_i(s) + 2\xi_i \omega_i s Q_i(s) + \omega_i^2 Q_i(s) = P_i U(s) \quad (\text{A.30})$$

where:

$$Q_i(s) = \frac{P_i U(s)}{s^2 + 2\xi_i \omega_i s + \omega_i^2} \quad (\text{A.31})$$

Note that the Laplace transform of the assumed modes solution (2.16) is:

$$Y(s, r) = \sum_{i=1}^N \psi_i(r) Q_i(s) \quad (\text{A.32})$$

Hence, substitute equation (A.31) into equation (A.32), and rearrange to give the final form of the transfer function from  $U(s)$  to  $Y(s, r)$ :

$$\frac{Y(s, r)}{U(s)} = \sum_{i=1}^N \frac{P_i \psi_i(r)}{s^2 + 2\xi_i \omega_i s + \omega_i^2} \quad (\text{A.33})$$

which is equal to the transfer function of the system given in equation (2.25).

## APPENDIX B

### MODELING OF THE SMART BEAM BY ASSUMED MODES METHOD

As mentioned in Section 2.3, in this thesis the admissible functions are selected as the exact eigenfunctions of a cantilevered passive beam given in equation (2.44). So, substitute the eigenfunctions into equations (2.28), (2.31) and (2.34) and apply the orthogonality conditions given in equations (2.45) and (2.46), the total energy expressions and viscous damping force of the smart beam become:

$$T_{sb}(t) = \frac{1}{2} \sum_{i=1}^N \sum_{j=1}^N \left\{ \rho_b A_b L_b^3 + 2\rho_p A_p L_p^3 \right\} \dot{q}_i \dot{q}_j \quad (\text{B.1})$$

$$V_{sb}(t) = \frac{1}{2} \sum_{i=1}^N \sum_{j=1}^N \left\{ \rho_b A_b L_b^3 + 2\rho_p A_p L_p^3 \right\} \omega_i^2 q_i q_j \quad (\text{B.2})$$

$$F_{sb}(t) = \frac{1}{2} \sum_{i=1}^N \sum_{j=1}^N \left\{ \rho_b A_b L_b^3 + 2\rho_p A_p L_p^3 \right\} 2\xi_i \omega_i \dot{q}_i \dot{q}_j \quad (\text{B.3})$$

Following the same formulation procedure given in Appendix A, i.e. substituting the above equations into Lagrange's equation of motion given in (2.17), one will yield the equations of motion as:

$$\ddot{q}_i(t) + 2\xi_i \omega_i \dot{q}_i(t) + \omega_i^2 q_i(t) = \frac{1}{\rho_b A_b L_b^3 + 2\rho_p A_p L_p^3} Q_i \quad (\text{B.4})$$

Now, recall external forcing expression given in equation (2.43). Substitute the bending moment expression given in equation (2.41) and the voltage term given in equation (2.35) into equation (2.43):

$$\begin{aligned} Q_i &= \int_0^{L_b} \frac{\partial^2}{\partial r^2} (C_p V_a(t) [H(r-r_1) - H(r-r_2)]) \phi_i(r) dr \\ &= \int_0^{L_b} C_p V_a \frac{d^2}{dr^2} (H(r-r_1) - H(r-r_2)) \phi_i(r) dr \end{aligned} \quad (\text{B.5})$$

The relation between Heaviside's function and Dirac's delta function,  $\delta$ , is [48]:

$$\delta(r-a) = \frac{d}{dr} [H(r-a)] \quad (\text{B.6})$$

where the Dirac's delta function satisfies:

$$\delta(x) = \begin{cases} \infty & x = 0 \\ 0 & x \neq 0 \end{cases} \quad (\text{B.7})$$

Hence, the external forcing expression reduces to:

$$Q_i = \int_0^{L_b} C_p V_a (\delta'(r-r_1) - \delta'(r-r_2)) \phi_i(r) dr \quad (\text{B.8})$$

The property of the derivative of Dirac's delta function is given as [48]:

$$\int_{-\infty}^{\infty} f(x)\delta'(x-a)dx = -f'(a) \quad (\text{B.9})$$

Hence using the above equality, the final expression of the external forcing expression becomes:

$$Q_i = C_p V_a [\phi'_i(r_2) - \phi'_i(r_1)] \quad (\text{B.10})$$

Substitution of equation (B.10) into equation (B.4) yields:

$$\ddot{q}_i(t) + 2\xi_i \omega_i \dot{q}_i(t) + \omega_i^2 q_i(t) = \frac{C_p V_a [\phi'_i(r_2) - \phi'_i(r_1)]}{\rho_b A_b L_b^3 + 2\rho_p A_p L_p^3} \quad (\text{B.11})$$

which is equivalent to the equation (2.48).

Taking Laplace transform of equation (B.11) and following the necessary mathematical manipulations as given in Appendix A, the frequency domain transfer function of the smart beam from the input voltage to the beam deflection becomes:

$$\bar{G}_N(s, r) = \frac{Y(s, r)}{V_a(s)} = \sum_{i=1}^N \frac{C_p [\phi'_i(r_2) - \phi'_i(r_1)] \phi_i(r)}{(\rho_b A_b L_b^3 + 2\rho_p A_p L_p^3)(s^2 + 2\xi_i \omega_i s + \omega_i^2)} \quad (\text{B.12})$$

For simplicity, define:

$$\bar{P}_i = \frac{C_p [\phi'_i(r_2) - \phi'_i(r_1)]}{\{\rho AL^3\}_{sb}} \quad (\text{B.13})$$

and

$$\{\rho AL^3\}_{sb} = \rho_b A_b L_b^3 + 2\rho_p A_p L_p^3 \quad (\text{B.14})$$

So, the final form of equation (B.12) becomes:

$$\bar{G}_N(s, r) = \sum_{i=1}^N \frac{\bar{P}_i \phi_i(r)}{s^2 + 2\xi_i \omega_i s + \omega_i^2} \quad (\text{B.15})$$

which is equivalent to the equation (2.49).

## APPENDIX C

### SPATIAL NORMS

The spatial  $H_2$  and  $H_\infty$  norms involve the spatial information of the spatially distributed systems. They can be used as performance measures in model correction and spatial control design [7]. The definitions and theorems given in this Appendix can be found in any of the following references [7, 13, 30, 31, 41] in detail. This appendix presents the definitions based on reference [41].

Consider the spatially distributed linear time-invariant (LTI) system which maps an input signal to an output signal as shown below:

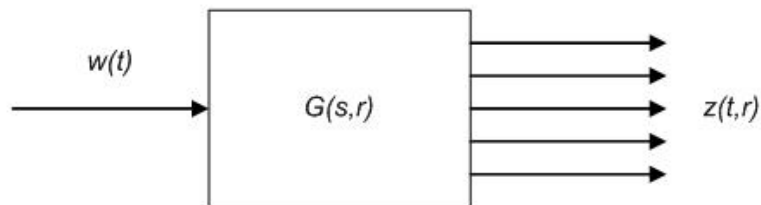


Figure C.1: A spatially distributed LTI system

where  $w(t)$  represents the system input and  $z(t,r)$  represents the system output.

### C.1 Spatial $H_2$ norm of a signal

The spatial  $H_2$  norm of a signal can be defined as the total energy of the spatially distributed signal  $z(t, r)$ :

$$\langle\langle z(t, r) \rangle\rangle_2^2 = \int_0^\infty \int_R z(t, r)^T z(t, r) dr dt \quad (\text{C.1})$$

In flexible one-dimensional structures, this norm can be interpreted as the deflection of every point along the structure.

### C.2 Spatial $H_2$ norm of a system

The spatial  $H_2$  norm of a system  $G(s, r)$  is defined as:

$$\langle\langle G(s, r) \rangle\rangle_2^2 = \frac{1}{2\pi} \int_{-\infty}^\infty \int_R \text{tr} \{ G(j\omega, r)^* G(j\omega, r) \} dr dt \quad (\text{C.2})$$

The spatial  $H_2$  norm of a system takes into account the spatial information embedded in the system such as the deflection of entire structure.

Theorem C.2.1: Consider a stable system  $G(s, r)$  that is represented in state-space form as:

$$\begin{aligned} \dot{x}(t) &= Ax(t) + Bu(t) \\ y(t, r) &= C(r)x(t) \end{aligned} \quad (\text{C.3})$$

Then

$$\langle\langle G(s, r) \rangle\rangle_2 = \|\tilde{G}(s)\|_2 \quad (\text{C.4})$$

where  $\tilde{G}(s)$  is a finite-dimensional system defined by:

$$\tilde{G}(s) = \Gamma(sI - A)^{-1} B \quad (\text{C.5})$$

and

$$\Gamma^T \Gamma = \int_R C(r)^T C(r) dr \quad (\text{C.6})$$

Theorem C.2.2: The spatial  $H_2$  norm of a spatially distributed system given in equation (2.25), where the eigenfunctions satisfy orthogonality condition given in equation (2.14), is equivalent to the  $H_2$  norm of a finite-dimensional LTI system.

$$\langle\langle G_N(s, r) \rangle\rangle_2^2 = \sum_{i=1}^N \|\tilde{G}_i(s)\|_2^2 \quad (\text{C.7})$$

where

$$\tilde{G}_i(s) = \frac{P_i}{s^2 + 2\xi_i \omega_i s + \omega_i^2} \quad (\text{C.8})$$

### C.3 Weighted spatial $H_2$ norm of signals and systems

The weighted spatial  $H_2$  norm of a signal  $z(t, r)$  is:

$$\|z(t, r)\|_{2, Q}^2 = \int_0^\infty \int_R z(t, r)^T Q(r) z(t, r) dr dt \quad (C.9)$$

The weighted spatial  $H_2$  norm of a system  $G(s, r)$  is:

$$\|G(s, r)\|_{2, Q}^2 = \frac{1}{2\pi} \int_{-\infty}^\infty \int_R \text{tr} \{ G(j\omega, r)^* Q(r) G(j\omega, r) \} d\omega dr \quad (C.10)$$

where in both case

$$Q(r) \geq 0 \quad (C.11)$$

The weighting function,  $Q(r)$ , emphasizes the certain regions within the domain. For example, in flexible structures, it shows the region over the structure where vibration levels will be controlled.

#### C.4 Spatial induced norm of a system

Let  $\mathbb{S}$  be the linear operator that maps the inputs of the system  $G(s,r)$  to its outputs. The spatial induced norm of  $\mathbb{S}$  is defined as:

$$\langle\langle \mathbb{S} \rangle\rangle^2 = \sup_{0 \neq w \in L_2[0, \infty)} \frac{\langle\langle z \rangle\rangle_2^2}{\|w\|_2^2} \quad (\text{C.12})$$

#### C.5 Spatial $H_\infty$ norm of a system

The spatial  $H_\infty$  norm of a system  $G(s,r)$  is defined as:

$$\langle\langle G \rangle\rangle_\infty^2 = \sup_{\omega \in R} \lambda_{\max} \left( \int_R G(j\omega, r)^* G(j\omega, r) dr \right) \quad (\text{C.13})$$

where  $\lambda_{\max}$  denotes the largest eigenvalue of the system.

Theorem C.5.1: Let  $\mathbb{S}$  be the linear operator that maps the inputs of the system  $G(s,r)$  to its infinite-dimensional outputs. Its induced operator norm  $\langle\langle \mathbb{S} \rangle\rangle$  satisfies:

$$\langle\langle \mathbb{S} \rangle\rangle = \langle\langle G \rangle\rangle_\infty \quad (\text{C.14})$$

## C.6 Weighted spatial induced norm of a system

Let  $\mathbb{S}$  be the linear operator that maps the inputs of the system  $G(s,r)$  to its outputs. The weighted spatial induced norm of  $\mathbb{S}$  is defined as:

$$\ll \mathbb{S} \gg_Q^2 = \sup_{0 \neq w \in L_2[0, \infty)} \frac{\ll z \gg_{2,Q}^2}{\|w\|_2^2} \quad (\text{C.15})$$

## C.7 Weighted spatial $H_\infty$ norm of a system

The weighted spatial  $H_\infty$  norm of a system  $G(s,r)$  is defined as:

$$\ll G \gg_{\infty,Q}^2 = \sup_{\omega \in R} \lambda_{\max} \left( \int_R G(j\omega, r)^* Q(r) G(j\omega, r) dr \right) \quad (\text{C.16})$$

From Theorem C.5.1:

$$\ll \mathbb{S} \gg_Q = \ll G \gg_{\infty,Q} \quad (\text{C.17})$$

## APPENDIX D

### SPATIAL $H_\infty$ CONTROL MODEL OF THE SMART BEAM

Consider the ordinary differential equations of motion given in equation (2.48):

$$\ddot{q}_i(t) + 2\xi_i \omega_i \dot{q}_i(t) + \omega_i^2 q_i(t) = \bar{P}_i V_a(t) \quad (\text{D.1})$$

where  $\bar{P}_i$  is given in equation (2.50).

In order to represent equation (D.1) in state space form, define states as:

$$\begin{aligned} x_1 &= q_1(t) \\ x_2 &= \dot{q}_1(t) \\ x_3 &= q_2(t) \\ x_4 &= \dot{q}_2(t) \end{aligned} \quad (\text{D.2})$$

From the above equations (D.1) and (D.2), time derivatives of the states can be found to be:

$$\begin{aligned}
\dot{x}_1 &= x_2 \\
\dot{x}_2 &= \bar{P}_1 V_a(t) - \omega_1^2 x_1 - 2\xi_1 \omega_1 x_2 \\
\dot{x}_3 &= x_4 \\
\dot{x}_4 &= \bar{P}_2 V_a(t) - \omega_2^2 x_3 - 2\xi_2 \omega_2 x_4
\end{aligned} \tag{D.3}$$

From equation (2.16), the displacement expression of the smart beam including the first two modes in terms of state variables will be as follows:

$$\begin{aligned}
y(t, r) &= \phi_1(r)q_1(t) + \phi_2(r)q_2(t) \\
&= \phi_1(r)x_1 + \phi_2(r)x_2
\end{aligned} \tag{D.4}$$

So, use  $u$  instead of  $V_a(t)$  to represent the system input in a more general form, one will yield the state space representation in matrix form as:

$$\begin{aligned}
\begin{bmatrix} \dot{x}_1 \\ \dot{x}_2 \\ \dot{x}_3 \\ \dot{x}_4 \end{bmatrix} &= \begin{bmatrix} 0 & 1 & 0 & 0 \\ -\omega_1^2 & -2\xi_1 \omega_1 & 0 & 0 \\ 0 & 0 & 0 & 1 \\ 0 & 0 & -\omega_2^2 & -2\xi_2 \omega_2 \end{bmatrix} \begin{bmatrix} x_1 \\ x_2 \\ x_3 \\ x_4 \end{bmatrix} + \begin{bmatrix} 0 \\ \bar{P}_1 \\ 0 \\ \bar{P}_2 \end{bmatrix} u \\
y(t, r) &= [\phi_1(r) \quad 0 \quad \phi_2(r) \quad 0] \begin{bmatrix} x_1 \\ x_2 \\ x_3 \\ x_4 \end{bmatrix}
\end{aligned} \tag{D.5}$$

Now, note that as mentioned in Chapter 4, the disturbance,  $w(t)$ , was assumed to enter our system through the actuator channel so it can be considered as another input to the system. Besides, the model correction term given in equation (2.59) was included in order to reduce the effect of

truncated higher modes on the system's output. So, the smart beam's spatial  $H_\infty$  controller design based state space model in matrix form will be:

$$\begin{aligned} \begin{bmatrix} \dot{x}_1 \\ \dot{x}_2 \\ \dot{x}_3 \\ \dot{x}_4 \end{bmatrix} &= \begin{bmatrix} 0 & 1 & 0 & 0 \\ -\omega_1^2 & -2\xi_1\omega_1 & 0 & 0 \\ 0 & 0 & 0 & 1 \\ 0 & 0 & -\omega_2^2 & -2\xi_2\omega_2 \end{bmatrix} \begin{bmatrix} x_1 \\ x_2 \\ x_3 \\ x_4 \end{bmatrix} + \begin{bmatrix} 0 & 0 \\ \bar{P}_1 & \bar{P}_1 \\ 0 & 0 \\ \bar{P}_2 & \bar{P}_2 \end{bmatrix} \begin{bmatrix} w \\ u \end{bmatrix} \\ y(t,r) &= \begin{bmatrix} \phi_1(r) & 0 & \phi_2(r) & 0 \end{bmatrix} \begin{bmatrix} x_1 \\ x_2 \\ x_3 \\ x_4 \end{bmatrix} + \left( \sum_{i=3}^{50} k_{ri}^{opt} \phi_i(r) \right) \begin{bmatrix} w \\ u \end{bmatrix} \\ y(t,r_L) &= \begin{bmatrix} \phi_1(r_L) & 0 & \phi_2(r_L) & 0 \end{bmatrix} \begin{bmatrix} x_1 \\ x_2 \\ x_3 \\ x_4 \end{bmatrix} + \left( \sum_{i=3}^{50} k_{ri}^{opt} \phi_i(r_L) \right) \begin{bmatrix} w \\ u \end{bmatrix} \end{aligned} \quad (D.6)$$

Rearranging the system will give:

$$\begin{aligned} \begin{bmatrix} \dot{x}_1 \\ \dot{x}_3 \\ \dot{x}_2 \\ \dot{x}_4 \end{bmatrix} &= \begin{bmatrix} 0 & 0 & 1 & 0 \\ 0 & 0 & 0 & 1 \\ -\omega_1^2 & 0 & -2\xi_1\omega_1 & 0 \\ 0 & -\omega_2^2 & 0 & -2\xi_2\omega_2 \end{bmatrix} \begin{bmatrix} x_1 \\ x_3 \\ x_2 \\ x_4 \end{bmatrix} + \begin{bmatrix} 0 \\ 0 \\ \bar{P}_1 \\ \bar{P}_2 \end{bmatrix} w + \begin{bmatrix} 0 \\ 0 \\ \bar{P}_1 \\ \bar{P}_2 \end{bmatrix} u \\ y(t,r) &= \begin{bmatrix} \phi_1(r) & \phi_2(r) & 0 & 0 \end{bmatrix} \begin{bmatrix} x_1 \\ x_3 \\ x_2 \\ x_4 \end{bmatrix} + \left( \sum_{i=3}^{50} k_{ri}^{opt} \phi_i(r) \right) w + \left( \sum_{i=3}^{50} k_{ri}^{opt} \phi_i(r) \right) u \\ y(t,r_L) &= \begin{bmatrix} \phi_1(r_L) & \phi_2(r_L) & 0 & 0 \end{bmatrix} \begin{bmatrix} x_1 \\ x_3 \\ x_2 \\ x_4 \end{bmatrix} + \left( \sum_{i=3}^{50} k_{ri}^{opt} \phi_i(r_L) \right) w + \left( \sum_{i=3}^{50} k_{ri}^{opt} \phi_i(r_L) \right) u \end{aligned} \quad (D.7)$$

Hence, the above matrix formed system can be represented in state space form as:

$$\begin{aligned}
\dot{x}(t) &= Ax(t) + B_1 w(t) + B_2 u(t) \\
y(t, r) &= C_1(r)x(t) + D_1(r)w(t) + D_2(r)u(t) \\
y(t, r_L) &= C_2 x(t) + D_3 w(t) + D_4 u(t)
\end{aligned} \tag{D.8}$$

which is equivalent to equation (4.1), and where the state space variables are:

$$A = \begin{bmatrix} 0 & 0 & 1 & 0 \\ 0 & 0 & 0 & 1 \\ -\omega_1^2 & 0 & -2\xi_1\omega_1 & 0 \\ 0 & -\omega_2^2 & 0 & -2\xi_2\omega_2 \end{bmatrix} \tag{D.9}$$

$$B_1 = B_2 = \begin{bmatrix} 0 \\ 0 \\ \bar{P}_1 \\ \bar{P}_2 \end{bmatrix} \tag{D.10}$$

$$C_1 = [\phi_1(r) \quad \phi_2(r) \quad 0 \quad 0] \tag{D.11}$$

$$C_2 = [\phi_1(r_L) \quad \phi_2(r_L) \quad 0 \quad 0] \tag{D.12}$$

$$D_1 = D_2 = \sum_{i=3}^{50} \phi_i(r) k_i^{opt} \tag{D.13}$$

$$D_3 = D_4 = \sum_{i=3}^{50} \phi_i(r_L) k_i^{opt} \tag{D.14}$$

which are equal to the equations (4.4) to (4.9).

As mentioned in Section 2.5, the spatial  $H_\infty$  control problem can be turned into an equivalent ordinary  $H_\infty$  problem by:

$$\int_R y(t,r)^T Q(r) y(t,r) dr dt = \tilde{y}(t)^T \tilde{y}(t) dt \quad (\text{D.15})$$

Hence, let spatial weighting function  $Q(r) = 1$  so that the region over which the effect of the disturbance is to be reduced will be the entire beam. Hence, equation (D.15) will reduce to:

$$\int_R y(t,r)^T y(t,r) dr = \tilde{y}(t)^T \tilde{y}(t) \quad (\text{D.16})$$

Recalling from state-space:

$$y(t,r) = [C_1 \quad D_1 \quad D_2] \begin{bmatrix} \underline{x} \\ w \\ u \end{bmatrix} \quad (\text{D.17})$$

where  $\underline{x}$  represents the vector of the states as:

$$\underline{x} = \begin{bmatrix} x_1 \\ x_3 \\ x_2 \\ x_4 \end{bmatrix} \quad (\text{D.18})$$

The transpose of equation (D.17) is:

$$y(t,r)^T = \begin{bmatrix} \underline{x}^T & w^T & u^T \end{bmatrix} \begin{bmatrix} C_1^T \\ D_1^T \\ D_2^T \end{bmatrix} \quad (\text{D.19})$$

So, the integral term of equation (D.16) will be:

$$y(t,r)^T y(t,r) = \begin{bmatrix} \underline{x}^T & w^T & u^T \end{bmatrix} \begin{bmatrix} C_1^T \\ D_1^T \\ D_2^T \end{bmatrix} \begin{bmatrix} C_1 & D_1 & D_2 \end{bmatrix} \begin{bmatrix} \underline{x} \\ w \\ u \end{bmatrix} \quad (\text{D.20})$$

that is:

$$y(t,r)^T y(t,r) = \begin{bmatrix} \underline{x}^T & w^T & u^T \end{bmatrix} \begin{bmatrix} C_1^T C_1 & C_1^T D_1 & C_1^T D_2 \\ D_1^T C_1 & D_1^T D_1 & D_1^T D_2 \\ D_2^T C_1 & D_2^T D_1 & D_2^T D_2 \end{bmatrix} \begin{bmatrix} \underline{x} \\ w \\ u \end{bmatrix} \quad (\text{D.21})$$

yielding in:

$$\int_R y(t,r)^T y(t,r) dr = \begin{bmatrix} \underline{x}^T & w^T & u^T \end{bmatrix} \Gamma^T \Gamma \begin{bmatrix} \underline{x} \\ w \\ u \end{bmatrix} = \tilde{y}(t)^T \tilde{y}(t) \quad (\text{D.22})$$

where:

$$\Gamma^T \Gamma = \begin{bmatrix} \int_R C_1^T C_1 dr & \int_R C_1^T D_1 dr & \int_R C_1^T D_2 dr \\ \int_R D_1^T C_1 dr & \int_R D_1^T D_1 dr & \int_R D_1^T D_2 dr \\ \int_R D_2^T C_1 dr & \int_R D_2^T D_1 dr & \int_R D_2^T D_2 dr \end{bmatrix} \quad (\text{D.23})$$

The orthogonality of eigenfunctions given in equation (2.45) can be rearranged as:

$$\int_0^{L_b} \phi_i \phi_j dr = L_b^3 \delta_{ij} \quad (\text{D.24})$$

Consider each element of the matrix given in equation (D.23) separately. So, substitute (D.11) into the below integration and apply the orthogonality given in equation (D.24):

$$\begin{aligned} \int_R C_1^T C_1 dr &= \int_0^{L_b} \begin{bmatrix} \phi_1 \\ \phi_2 \\ 0 \\ 0 \end{bmatrix} [\phi_1 \quad \phi_2 \quad 0 \quad 0] dr \\ &= \begin{bmatrix} \int_0^{L_b} \phi_1 \phi_1 dr & \int_0^{L_b} \phi_1 \phi_2 dr & 0 & 0 \\ \int_0^{L_b} \phi_2 \phi_1 dr & \int_0^{L_b} \phi_2 \phi_2 dr & 0 & 0 \\ 0 & 0 & 0 & 0 \\ 0 & 0 & 0 & 0 \end{bmatrix} \\ &= \begin{bmatrix} L_b^3 & 0 & 0 & 0 \\ 0 & L_b^3 & 0 & 0 \\ 0 & 0 & 0 & 0 \\ 0 & 0 & 0 & 0 \end{bmatrix} \end{aligned} \quad (\text{D.25})$$

Similarly, substitute equations (D.11) and (D.13) into the below integral:

$$\int_R C_1^T D_1 dr = \int_0^{L_b} \begin{bmatrix} \phi_1 \\ \phi_2 \\ 0 \\ 0 \end{bmatrix} \left[ \sum_{i=3}^{50} k_i^{opt} \phi_i(r) \right] dr \quad (D.26)$$

and since  $i=3\dots 50$ , due to the orthogonality:

$$\int_R C_1^T D_1 dr = \begin{bmatrix} 0 \\ 0 \\ 0 \\ 0 \end{bmatrix} \quad (D.27)$$

As the equality mentioned in equation (D.13) is used, the result of equation (D.27) will be equal to the integrals  $\int_0^L C_1^T D_2 dr$ ,  $\int_R D_1^T C_1 dr$  and  $\int_R D_2^T C_1 dr$ .

Similarly:

$$\begin{aligned} \int_R D_1^T D_1 dr &= \int_0^{L_b} \left[ \sum_{i=3}^{50} k_i^{opt} \phi_i(r) \right] \left[ \sum_{j=3}^{50} k_j^{opt} \phi_j(r) \right] dr \\ &= \sum_{i=3}^{50} \sum_{j=3}^{50} \int_0^{L_b} (k_i^{opt})(k_j^{opt}) \phi_i(r) \phi_j(r) dr \\ &= \sum_{i=3}^{50} (k_i^{opt})^2 L_b^3 \end{aligned} \quad (D.28)$$

Equation (D.28) is also equal to  $\int_0^L D_2^T D_1 dr$ ,  $\int_R D_1^T D_2 dr$  and  $\int_R D_2^T D_2 dr$ .

Hence, substituting each matrix element in equation (D.23) yields in:

$$\Gamma^T \Gamma = \begin{bmatrix} L_b^3 & 0 & 0 & 0 & 0 & 0 \\ 0 & L_b^3 & 0 & 0 & 0 & 0 \\ 0 & 0 & 0 & 0 & 0 & 0 \\ 0 & 0 & 0 & 0 & 0 & 0 \\ 0 & 0 & 0 & 0 & \sum_{i=3}^{50} (k_i^{opt})^2 L_b^3 & \sum_{i=3}^{50} (k_i^{opt})^2 L_b^3 \\ 0 & 0 & 0 & 0 & \sum_{i=3}^{50} (k_i^{opt})^2 L_b^3 & \sum_{i=3}^{50} (k_i^{opt})^2 L_b^3 \end{bmatrix}_{6 \times 6} \quad (\text{D.29})$$

which is satisfied by:

$$\Gamma = \begin{bmatrix} L_b^{3/2} & 0 & 0 & 0 & 0 & 0 \\ 0 & L_b^{3/2} & 0 & 0 & 0 & 0 \\ 0 & 0 & 0 & 0 & 0 & 0 \\ 0 & 0 & 0 & 0 & 0 & 0 \\ 0 & 0 & 0 & 0 & \left( \sum_{i=3}^{50} (k_i^{opt})^2 L_b^3 \right)^{1/2} & \left( \sum_{i=3}^{50} (k_i^{opt})^2 L_b^3 \right)^{1/2} \end{bmatrix} \quad (\text{D.30})$$

where  $\Gamma$  is defined as [7]:

$$\Gamma = [\Pi \quad \Theta_1 \quad \Theta_2] \quad (\text{D.31})$$

such that:

$$\Gamma = \begin{bmatrix} L_b^{3/2} & 0 & 0 & 0 \\ 0 & L_b^{3/2} & 0 & 0 \\ 0 & 0 & 0 & 0 \\ 0 & 0 & 0 & 0 \\ 0 & 0 & 0 & 0 \end{bmatrix} \quad (\text{D.32})$$

and,

$$\Theta_1 = \Theta_2 = \begin{bmatrix} 0 \\ 0 \\ 0 \\ 0 \\ \left( \sum_{i=3}^{50} (k_i^{opt})^2 L_b^3 \right)^{1/2} \end{bmatrix} \quad (\text{D.33})$$

where equations (D.32) and (D.33) are equal to the ones given in (4.10) and (4.11).